# SUPERCRITICAL FLUID PROCESSING OF NOVEL TISSUE ENGINEERING SCAFFOLDS CONTAINING SILICA

By

NIKI JANE COLLINS

A thesis submitted to
The University of Birmingham
For the degree of
DOCTOR OF PHILOSOPHY

Department of Chemical Engineering
School of Engineering and Physical Sciences
The University of Birmingham
October 2010
Corrected September 2011

# Abstract

Three dimensional scaffolds were created from a biodegradable polymer (polylactide) and the mineral silica utilising supercritical fluid (SCF) gas foaming. The effect of silica on the scaffold pore architecture was investigated through X-ray computed microtomography (microCT); the scaffolds were shown to be up to 60% porous with pore diameters in the range of 0.088-0.924 mm (0% silica) to 0.044 – 0.342 mm (33.3% silica), demonstrating that silica controlled both pore size and overall scaffold porosity; Silica was found to enhance connectivity of the pores and pore wall thickness and pore connectivity were found have an inverse relationship. Differential scanning calorimetry (DSC) was used to investigate the effect of silica on the $T_m$, $T_g$ and crystallinity of the PLA pre and post SCF processing; increases in $\Delta H_f$ (4J/g) $T_g$ ($1^oC$) and crystallinity (3%) showed that silica had a beneficial effect pre-SCF but post-SCF the PLA reverted to an amorphous state; An isothermal conditioning process was found to restore the previous levels of crystallinity. Mechanical strength testing of the scaffolds showed that silica incorporation increased the load tolerated at yield by up to 60N and the strength by up to 1.5 mPa. The scaffolds were immersed in simulated body fluid (SBF), where the presence of silica was found to enhance mineral deposition by up to 10%; they were also subjected to degradation experiments in physiological saline solution and enzyme buffer solution, where degradation was found to occur most rapidly in the amorphous regions of the polymer (0% and 9.1% silica). The formation of degradation products (lactic acid, isopropanol and lactate) were monitored through HPLC.

In conclusion, addition of silica up to a loading of 9.1-16.7% was found to have many beneficial effects on the PLA scaffolds but no observable benefit was found with additions higher than this.

# Acknowledgements

I would like to thank my supervisors at the University of Birmingham (Dr L M Grover, Dr R H Bridson and Dr G A Leeke) for all of their advice and support over the last 4 years.

For technical help and assistance, I would like to thank Mrs Sue Fisher at Birmingham Dental School; Dr Taghi Miri and Dr James Bowen of the University of Birmingham; and Elaine, Hazel and Christine in the Biocentre at the University of Birmingham.

I would like to acknowledge the BBSRC for their award of a research scholarship, without which this project would never have taken place.

Lastly, I would like to thank my nearest and dearest for tolerating my absence (emotionally, mentally and physically) during the time I have spent on this project, and for offering me unconditional and unlimited moral support and shoulders to cry on.

# Table of Contents

**Chapter 1: Historical over view of the literature** 1
1.1 The need for replacement bone material 1
1.2 Tissue engineering 2
1.3 Physical and structural properties of a tissue engineered scaffold 2
1.4 Materials that can be used to create tissue engineered scaffolds 5
1.1.1 Natural polymers 5
1.1.2 Synthetic polymers 6
1.1.2.1 Polyglycolic acid (Polyglycolide) 7
1.1.2.2 Polycaprolactone 10
1.1.2.3 Polylactic acid (Polylactide) 13
1.1.3 Composites 21
1.1.3.1 Polymer-bioceramic composites 21
1.1.3.2 Polymer-bioglass composites 22
1.2 Scaffold manufacture 22
1.2.1 Solvent casting – particle leaching (SCPL) 23
1.2.2 Emulsion freeze drying 23
1.2.3 Phase separation 24
1.2.4 Computer aided design (CAD) and computer aided manufacture (CAM) 24
1.2.5 Supercritical fluids (SCFs) 25
1.2.6 SCF processing of polymers (gas foaming) 26
1.2.6.1 SCF dissolution 27
1.2.6.2 SCF ‘soak’ time 28
1.2.6.3 Depressurisation and cooling 29
1.2.6.4 Disadvantages of gas foaming 29
1.3 Degradation of PLA 30
1.3.1 Autocatalysis 34
1.3.2 The effect of temperature on degradation 34
1.3.3 Hydrolysis of PLA in neutral media 35
1.3.4 Enzymatic hydrolysis of PLA 37
1.4 Mineral deposition by simulated body fluid (SBF) 38
1.5 Bone 40
1.5.1 The structure and properties of bone 40
1.5.2 Bone formation 41
1.5.3 Bone cells 42
1.5.3.1 Osteoprogenitor cells 42
1.5.3.2 Osteoblasts 42
1.5.3.3 Osteocytes 42
1.5.3.4 Osteoclasts 43
1.5.4 Remodelling (‘coupling’) 43
1.5.4.1 Resorption 44
1.5.4.2 Rebuilding 45
1.5.5 Control of bone formation and resorption 46
1.5.6 Types of bone 47
1.5.6.1 Woven bone 47

1.5.6.2 Cortical (lamellar) bone 47
1.5.6.3 Cancellous bone 48
1.5.7 Distribution and relative proportions of cortical and cancellous bone 49
1.5.8 The clinical need for bone replacement 49
1.5.8.1 Types of bone graft 50
Autograft 50
Xenograft 51
1.6 The scope of this project 51

**Chapter 2: Scaffold manufacture** 53
2.1 Introduction 53
2.2 Materials 54
2.2.1 Polylactide 54
2.2.1.1 Characterisation of PD,LLA 3051D 55
2.2.2 Silica 55
2.2.3 Choice of solvent: Dichloromethane 55
2.3 Supercritical fluid foaming equipment 56
2.4 Methods 59
2.4.1 Establishing optimum experimental conditions 59
2.4.2 Production of PLA-silica films 59
2.4.3 SCF foaming process 61
2.4.4 MicroCT 62
2.4.4.1 Sample preparation and mounting 62
2.4.5 SEM 63
2.4.5.1 Sample preparation and mounting 63
2.5 Results and discussion 64
2.5.1 Development of experimental methodology 65
2.5.2 Calculation of relative porosity 66
2.5.3 Effect of depressurisation rate on the porosity and pore size of the scaffolds 67
2.5.4 Depressurisation rate studies 67
2.5.4.1 Porosity 67
2.5.4.2. Pore size 70
2.5.5 Pore nucleation studies - the effect of silica 73
2.5.5.1 Porosity 73
2.5.5.2. Pore size 73
2.6 Conclusion 79

**Chapter 3 Scaffold microstructure and connectivity** 80
3.1 Section introduction 80
3.1.1 Mercury intrusion porosimetry 83
3.1.1.1 Theory 83
3.1.2 The Archimedes method 86
3.2 Materials 86
3.3 Methods 86
3.3.1 MIP 86
3.3.2 Light microscopy 87

3.3.3 Archimedes method 87
3.3.4 MicroCT 88
3.4 Calculations 89
3.4.1 MIP 89
3.4.2 Archimedes method 90
3.5 Results and discussion 91
3.5.1 Light microscopy 91
3.5.2 MIP 92
3.5.3 Archimedes method 96
3.5.4 MicroCT 99
3.6 Conclusion 104

**Chapter 4 Physical and mechanical properties** 105
4.1 Introduction 105
4.1.1 Physical properties: Tg 105
4.1.2 Physical properties: Tm and Xc 106
4.1.3 DSC 107
4.1.4 Crystallisation 111
4.1.5 Crystal structure and formation 111
4.1.6 Crystallisation kinetics 114
4.1.7 Polarised light microscopy (hot stage microscopy) 114
4.1.8 Mechanical strength testing 115
4.2 Materials and methods 116
4.2.1 DSC 116
4.2.1.1 Sample preparation 116
4.2.1.2 Non-isothermal crystallisation studies (determination of Tg and Tm) 117
4.2.1.3 Isothermal crystallisation studies 117
4.2.2 Hotstage microscopy and polarised light images 117
4.2.2.1 Sample preparation 118
4.2.2.2 Observation of spherulite formation 118
4.2.3 Mechanical strength testing 120
4.3 Results and discussion 121
4.3.1 DSC 121
4.3.1.1 Non-isothermal crystallisation studies 121
4.3.1.2 Isothermal crystallisation studies 129
4.3.2 Hotstage microscopy 133
4.3.3 Mechanical Strength testing 136
4.4 Conclusion 140

**Chapter 5: In-vitro and degradation behaviour of PLA and PLA-silica scaffolds** 142
5.1 Introduction 142
5.2 Materials and methods 143
5.2.3 Development of experimental methodology 143
5.2.4 SBF 144
5.2.4 Mineral deposition study 145
5.2.5 Degradation of PLA and PLA/silica scaffolds by Ringers solution 146

5.2.6 Degradation of PLA and PLA/silica scaffolds by Proteinase k 147
5.2.7 von Kossa staining technique 148
5.2.8 Elemental analysis 149
5.3 Results and discussion 149
5.3.1 Mineral deposition studies 149
5.3.2 Ringers degradation 153
5.3.3 Enzyme degradation 157
5.3.4 DSC analysis of enzyme degraded samples 164
5.3.5 MicroCT 166
5.4 Conclusion 168
**Chapter 6: Summary of Conclusions** 170
**Chapter 7: Further work** 174

References

Appendix I HPLC calibration curve
Appendix II Publications

## List of figures

**Figure 1.1** Polyglycolic acid repeat unit 7
**Figure 1.2**: Polyglycolic acid (polyglycolide) synthesis 8
**Figure 1.3**: Polycaprolactone synthesis 11
**Figure 1.4**: Lactic acid synthesis 16
**Figure 1.5**: Stereoisomers of lactic acid 16
**Figure 1.6**: Production of lactide and polylactic acid 18
**Figure 1.7**: Isomeric forms of lactide 18
**Figure 1.8**: Schematic of co-ordination insertion chain growth mechanism 18
**Figure 1.9**: The Cargill Dow non-solvent process to produce PLA 19
**Figure 1.10**: Pressure-temperature graph for $CO_2$ (McHugh, 1994) 25
**Figure 1.11**: Schematics of ester hydrolysis - nucleophilic substitution reaction (SN2) 33
**Figure 1.12:** Activation of bone resorption. **a**, Activated multinucleated polykaryons adhere to bone and undergo cell differentiation into a mature osteoclasts; **b,** formation of Howships lacunae and digestion of bone by acidophilic enzymes (CATK and TRAP). 44
**Figure 1.13:** Cross-section through lamellar bone showing three complete osteons (Schafer, 1954) 48
**Figure 2.1**: Visual appearance of ‘as received’ PD,LLA 3051D. L: Amorphous, transparent pellets; R: opaque, semi-crystalline pellets. 54
**Figure 2.2**: Schematic diagram showing the rig used to process the scaffold materials 56
**Figure 2.3: A**: Measurement of height of scaffolds (looking down onto the scaffold) **B**: Measurement of diameter of scaffolds (looking at the side of the scaffold) 65
**Figure 2.4**: PLA scaffold, formed through the SCF foaming process 67
**Figure 2.5**: The influence of depressurisation rate on the porosity of PLA scaffolds containing 0% silica obtained through gas foaming at $160^0$C and 160 bar with vent rates as stated (error bars indicate standard deviation from the mean) (n=4) 68
**Figure 2.6**: Pore size distributions of foamed PLA-silica scaffolds from microCT 74
**Figure 2.7: A**) PLA x 12 magnification; **B**) PLA with 33.3% silica x 20 magnification; **C**) PLA x 80 magnification and **D**) PLA with 33.3% silica x 65 magnification. 77
**Figure 2.8:** MicroCT models showing pore architecture of the scaffolds. **A:** 0% silica; **B:** 33.3% silica 78
**Figure 3.1**: Different pore types: a) open; b) closed; c) dead – ended; d) open – ended. 80
**Figure 3.2**: The interfaces present on a drop of liquid resting on a solid surface. 84
**Figure 3.3**: Angles of contact for wetting and non – wetting liquids. 84
**Figure 3.4**: Light micrographs of PLA-silica scaffolds x 400 magnification. 92
**Figure 3.5**: Analysis of pore size distribution by MIP. 93
**Figure 3.6A:** An ideal intrusion – extrusion curve illustrating restitution (Micropore instruction manual) 94
**Figure 3.6 B**: Intrusion-extrusion curves typical of those obtained from the PLA-silica scaffolds, showing that restitution does not occur 95
**Figure 3.7**: Relationship between apparent density, fraction density and fraction porosity with variation in silica content. Error bars for apparent density are standard deviation from the mean (n=3), other error bars are values ± 5%. 97

**Figure 3.8**: Relationship between the fraction interconnected porosity and silica content of PLA scaffolds impregnated with silica (error bars indicate standard deviation from the mean; n=3). 98
**Figure 3.9**: Cross-section and longitudinal section images through PLA-silica scaffolds obtained through microCT X ray attenuation images. 99
**Figure 3.10**: The same cross-section image as in Figure 3.8, thresholded for solid and pores. 100
**Figure 3.11**: Relative volumes within the PLA-silica scaffolds occupied by solid and pores obtained from microCT calculations of percent object volume. 101
**Figure 3.12**: Comparison of pore connectivity in SCF foamed scaffolds. 102
**Figure 3.13**: Relationship between pore wall thickness and fraction interconnected porosity (Error bars indicate standard deviation from the mean, n=4) 103
**Figure 4.1**: Graphical illustration of the relationship between temperature and heat capacity showing the position of the Tg. 106
**Figure 4.2**: Cross sectional diagram through the heating block of power compensated DSC apparatus (replicated from Perkin-Elmer user guide). 108
**Figure 4.3**: Spherulite formation. A: Crystalline regions of the polymer aggregate. B: Repeated branching develops the intermediate ‘wheat sheaf’ structure. C: Further branching makes the crystallite spherical in shape, hence the name spherulite. 112
**Figure 4.4**: Section through a spherulite showing extensive folding and close packing of the crystalline regions of the polymer chain to form sheets called lamella, with amorphous regions of polymer sandwiched between the lamella. R is direction of chain propagation. 113
**Figure 4.5**: Polarised light micrograph of PLLA spherulites showing the ‘Maltese cross’ effect caused by birefringence of polarised light (Permission applied for; Chao et al, 2008). 115
**Figure 4.6**: DSC thermogram of typical non-isothermal crystallisation heating and cooling profile obtained from PLA bead. 121
**Figure 4.7**: DSC thermogram of typical non-isothermal crystallisation heating and cooling profile obtained from solvent cast PLA film. 122
**Figure 4.8**: DSC thermogram of typical non-isothermal crystallisation heating and cooling profile obtained from solvent cast PLA-9.1% showing the effect of thermal decomposition on the melt peak. 123
**Figure 4.9**: ΔHf calculated from the area under curve measurements of DSC thermograms, showing the effect of silica on the energy associated with the melt transition. The effect of silica in samples containing 23.1% silica or higher were significant (Mann-Whitney two tailed U test, P=0.05) 126
**Figure 4.10**: Crystallinity of ‘as received’ PLA beads compared to solvent cast PLA/PLA-silica films. 127
**Figure 4.11**: DSC thermogram of a typical heating and cooling profile obtained from SCF processed foams containing PLA with the addition of 23.1% silica. 128
**Figure 4.12**: The effect of silica on Tm of silica containing PLA films pre and post isothermal crystallisation. Values are presented with the standard deviation from the mean (n=4) 130
**Figure 4.13**: The effect of silica on crystallinity pre and post isothermal crystallisation. Values were calculated from the average of the corresponding ΔHf values (n=4) 131

**Figure 4.14**: Variation in ΔHf with degree of heating/processing. Dark grey = solvent cast films pre isothermal crystallisation; Light grey = solvent cast films post isothermal crystallisation; White = SCF processed foams post isothermal crystallisation. 131
**Figure 4.15**: Images acquired through hotstage microscopy during isothermal crystallisation of PLA film at 110 $^{o}$C.133
**Figure 4.16**: Polarised light image of (C) above, showing birefringence of the PLA spherulites consistent with ‘Maltese cross’ effect. 134
**Figure 4.17**: Stress-strain curve to yield point obtained from compression testing of the SCF processed PLA and PLA/silica scaffolds 137
**Figure 4.18**: Effect of silica content on elastic modulus of PLA scaffolds demonstrating an approximately linear relationship, the error bars indicate standard deviation from the mean (n=5) 137
**Figure 4.19**: Bulk modulus for a material containing silica that obeys the Law of Mixtures, showing the relationship to be linear 138
**Figure 5.1**: Continuous circulation apparatus for mineral deposition study 145
**Figure 5.2**: % mass gains of the PLA and PLA-silica scaffolds during ageing in SBF (± % standard deviation from the mean, n=4). 150
**Figure 5.3**: Foamed PLA scaffolds stained using the von Kossa method to show the presence of mineral deposits. A), B) and C) Pure PLA, PLA containing 16.7wt% and 33.3wt% silica respectively prior to ageing. D), E) and F) Pure PLA, PLA containing 16.7wt% and 33wt% silica respectively following ageing in SBF for 28 days. 151
**Figure 5.4**: **A:** Environmental scanning electron micrograph of the mineral deposit identified on the surface of a polymer scaffold containing 33.3% silica after 28 days immersion in SBF; **B:** EDS spectra showing the deposit to contain calcium and phosphate ions 152
**Figure 5.5**: FTIR of mineral deposits compared with PLA. Phosphate group, 1000 cm-1(mineral deposit); ester (C-O) bond stretch, 1100 cm-1; ketone (C=O) stretch, 1750 cm-1 (both PLA). (Absorbance units are arbitrary) 153
**Figure 5.6**: HPLC trace of scaffolds containing 0% silica after degradation in Ringers buffer showing absence of a lactic acid peak at 16.74 minutes, but the presence of a second peak at a later retention time of around 26 minutes 155
**Figure 5.7**: HPLC elution curves typical of PLA scaffolds containing 9.1% and 33.3% silica after degradation in Ringers buffer. The presence of a lactic acid peak at 16.74 minutes, and also the presence of a second peak at a later retention time of around 26 minutes can clearly be seen 157
**Figure 5.8**: HPLC analysis of the supernatants obtained from the enzyme degradation experiments with PLA scaffolds 158
**Figure 5.9**: HPLC elution curves typically obtained from the supernatants of the enzyme degradation of scaffolds containing 9.1% and 33.3% silica; note the new peak at 15.5 minutes. 160
**Figure 5.10:** Cumulative mass fraction of lactic acid produced during degradation of scaffolds **A:** Ringers buffer; **B:** Tris-proteinase k 162
**Figure 5.11**: DSC thermogram of PLA post enzyme degradation showing almost total loss of Tg 164
**Figure 5.12**: MicroCT images taken throughout the enzyme degradation process. 167

# List of tables

**Table 2.1**: Physical and mechanical properties of PD,LLA 3051D (From Natureworks injection moulding document) 54
**Table 2.2**: Equipment specifications for pressure vessel 57
**Table 2.3**: Equipment specifications for peripheral components of the SCF rig 58
**Table 2.4**: Silica contents of solvent cast PLA films (final concentration of silica, with respect to total scaffold mass). 61
**Table 2.5**: Observations of the scaffold material made whilst optimising the process parameters 64
**Table 2.6:** Representative data relating to pore volume contribution in scaffolds containing 0% silica obtained through gas foaming at $160^0$C and 160 bar with vent rates as stated (n=1) 71
**Table 2.7**: The influence of silica upon the overall porosity of PLA scaffolds produced through SCF foaming in $CO_2$ at $160^oC$ and 160 bar (the error given is the standard deviation from the mean; n=8) 73

**Table 3.1**: Definitions of some common terms used to describe pores and porosity. BSI, British Standards Institute; ASTM, American Society for Testing and Materials 81
**Table 3.2**: Trends in apparent density and theoretical density with silica content (n=3) 96
**Table 3.3**: Fraction interconnected porosity (F.I.P) as a function of the porosity measurements obtained by the Archimedes method and microCT 98

**Table 4.1:** The values of $T_m$ and $T_g$ of an ‘as received’ PLA bead and of solvent cast PLA-silica films obtained through DSC non-isothermal crystallization. Values are presented with the standard deviation from the mean (n=4) 124
**Table 4.2:** The values of $T_g$ of SCF processed ‘as received’ PLA bead and PLA-silica films obtained through DSC non-isothermal crystallisation. Values are presented with the standard deviation from the mean (n=4) 128
**Table 4.3**: Data obtained through DSC for post isothermal crystallisation of films and foams (the error given is the standard deviation from the mean; n=4) 129
**Table 4.4**: Spherulite impingement time and final diameter 136
**Table 4.5**: Dimensions of the scaffolds used in the mechanical strength tests. Errors given are standard deviation from the mean (n=5) 136
**Table 4.6:** Effect of silica content on load and strength at yield point of PLA scaffolds (errors given are standard deviation from the mean, n=5) 139

**Table 5.1**: Reagents and amounts required to make 1 litre of SBF (Kokubo, 2006) 145
**Table 5.2**: Average mass data obtained from Ringers degradation of PLA scaffolds containing 0% silica 154
**Table 5.3**: Average mass data obtained from Ringers degradation of PLA scaffolds containing 9.1% silica (errors given are standard deviation from the mean, n=4) 156
**Table 5.4**: Average mass data obtained from Ringers degradation of PLA scaffolds containing 33.3% silica (errors given are standard deviation from the mean, n=4) 156

**Table 5.5**: Average mass data obtained from proteinase k degradation of PLA scaffolds 158
**Table 5.6**: Average mass data obtained from proteinase k degradation of PLA scaffolds containing 9.1% silica (errors given are standard deviation from the mean, n=4) 159
**Table 5.7**: Average mass data obtained from proteinase k degradation of PLA scaffolds containing 33.3% silica (errors given are standard deviation from the mean, n=4) 159
**Table 5.8:** Peak data obtained from the HPLC analysis of the supernatants of Ringers (R) (wk17/wk/18/wk19/wk20) and Tris-proteinase K (TP) (d3/d6/d9/d13/d16) degradation of PLA and PLA-silica scaffolds (single point run) 161
**Table 5.9:** Change in $T_m$ and ΔH throughout enzyme degradation as evidenced by DSC There was no obvious difference between like samples but there was a significant difference between 0% and 33.3% samples (Mann-Whitney U test two tails, p=0.05). Errors represent standard deviation from the mean (n=4) 165

# Chapter 1: Historical over view of the literature

## 1.1 The need for replacement bone material

The global need for synthetic replacement implants for bone and joints is high and there is an ever-increasing demand due to ageing of the general population, the incidence of osteoporosis among them, and also increasing numbers of sports related injuries in young adults (Rack and Qazi, 2005; Cordonnier *et al*, 2011).

At present, the gold standard in bone replacement is to use autograft tissue (self donation of tissue). Bone autografts contain the patient's own bone growing cells and proteins, which provide a framework for new bone to grow into. Most often, surgeons slice the harvested bone into small chips to fill the defect volume but there are inherent problems associated with this technique such as death of the surrounding tissue at the site of donation, and limitations on how much tissue can be harvested (Freed and Vunjak-Novakovic, 1997). Free vascularised fibular grafting is another standard salvage procedure for reconstructing critical size bone defects after bone tumor resection (Ghert *et al*, 2007; Freidrich *et al*, 2008), or congenital pseudarthrosis (Ohnishi *et al*, 2005; Sakamoto *et al*, 2008).

Titanium metal alloy implants are also widely used although they have a life expectancy of 12-15 years depending upon use before they require replacement. Each subsequent occurrence of surgery creates its own risk of infection and leads to weakening of the tissues surrounding that which is being replaced (Rack and Qazi, 2006; Vadiraj and Kamaraj, 2005).

Current sources donor of tissue include allograft (non-self) or xenograft (non-human) donations (Marler *et al* 1998), both of which are potential sources of disease transmission and which are known to provoke an immune reaction on implantation, resulting in rejection of the implant and the need for long term medication.

The field of tissue engineering (with collaborations in regenerative medicine) is subject to a vast amount of research in an effort to find alternatives that would negate the need for these donated tissues and their inherent problems.

## 1.2 Tissue engineering

The general aim of tissue engineering is to apply the principles of engineering and life sciences towards the development of biological substitutes that restore, maintain, or improve tissue or organ function utilising knowledge about the underlying biological system to make the engineered tissue as functional as possible. (Langer and Vacanti, 1993; MacArthur and Oreffo, 2005; Tai *et al*, 2007).

Engineered implants can be created *ex vivo* (implantation of tissues which have been pre-cultured in vitro) or *in vivo* (direct implantation of isolated / cultured cells or direct *in situ* tissue regeneration) but the basic requirements of the implant are the same in both scenarios (Sachlos and Czernuszka, 2003; Cordonnier *et al*, 2011).

## 1.3 Physical and structural properties of a tissue engineered scaffold

Tissue engineered scaffolds operate in one of three ways:

- To support the polymer/cell/tissue construct up to the point where it is remodelled by the host tissue, in which case it must provide mechanical support (behave as cartilage or bone), degrade/resorb at a rate such that the strength of the scaffold is retained, and be metabolised in the body with no noticeable immune reaction.

- To support cell proliferation and differentiation up to the point at which it can be implanted into the host, whereby it has to maintain its structural integrity until the engineered tissue is able to support itself (Hutmacher, 2000).
- To encapsulate living cells and thus provide a means of implantation whilst also offering protection from the immune system of the host organism.

Some scaffolds (particularly those made from natural polymers) can also be used as to deliver combinations of delicate biological materials such as cell adhesion motifs, growth factors, angiogenic factors, differentiation factors and immunosuppressive or anti-inflammatory agents (Hubbell, 1999). In these circumstances, temporal and spatial control of release is crucial to successful tissue repair and regeneration.

When applied to the field of joint or bone replacement, tissue engineering generally involves the manufacture of a three-dimensional (3D) scaffold or template upon which cells can be seeded which allows them to grow at a rate, density and spatial arrangement similar to that found in a naturally occurring physiological system (Yang and Ng, 2007). In order to fulfil this function the scaffold has to be both porous (to allow exchange of gases and nutrients around the cells) and mechanically strong (Barry *et al*, 2006; Chen *et al*, 2010).

The scaffold material therefore needs to have a high enough elastic modulus to be retained in the space that it was designed for, but it also has to provide the tissue with enough room to grow. It has to be screwed, sutured or pinned to the host tissues so needs a high degree of interatomic or molecular bonding, yet it must also allow for hydrolysis/breakdown once transplanted (Langer and Peppas, 1994; Chen *et al*, 2010).

Pore morphology and porosity are important parameters in tissue engineering and they must be tailored to the type of tissue being regenerated (Coombes *et al*, 2004). It has been found that certain cell lineages have precise requirements and preferences for pore size and architecture: Bony growth predominates in porous structures with pore sizes of approximately 450 µm, although there are conflicting reports in the literature reporting bone growth for pores measuring less than 100 µm and above 500 µm (Mikos *et al*, 1993, Gauthier *et al*, 1998); Connective tissue grows preferentially in pores of 100 µm in size or less (Ikada, 1994); vascular infiltration ideally attaches and grows within pores of approximately 1000 µm, whilst structures containing macropores (150–300 µm in diameter) highly interconnected by micropores (<50 µm in diameter) have been found to be conducive to growth of fibrocartilaginous tissue. Another important factor is that if the dimensions of the window between interconnecting pores is too small it can prevent cellular growth through the scaffold structure.

Therefore the capability to control pore size and architecture is a key factor in the success of any microcellular material to be used in tissue engineering, and an ideal scaffold structure should have:

- A 3D structure with a highly interconnected pore network to allow cell growth and flow of nutrients and waste;
- Controllable degradation to match tissue growth;
- Surface chemistry suitable for cell attachment, proliferation and differentiation;
- Mechanical properties matching the site of implantation.

## *1.4 Materials that can be used to create tissue engineered scaffolds*

Traditionally in replacement bone tissue engineering, implants are made from a metal alloy (commonly containing titanium), but these implants have a finite life span, and the surgical implantation process can be quite traumatic and the recovery time lengthy. New alternatives being extensively explored include natural polymers, synthetic biodegradable polymers, polymer-bioceramic composites or polymer-bioglass composites. Although the implantation process would still require surgery, it is proposed that there would be little adverse reaction, and that the implant would become incorporated into the native tissue at the site of insertion, through a process similar to that of natural fracture healing. The properties of each of these alternative materials will now be explored.

### 1.4.1 Natural polymers

Natural occurring polymers, such as proteins contained within the extracellular matrix (ECM) (Bedossa and Paradis, 2003), fibrin (Sakiyama *et al*, 1999), collagen (Sachlos *et al*, 2003; Chen *et al*, 2006), alginate (Glickis *et al*, 2000), cellulose (Cromme *et al*, 2007) or silk worm thread (Mandal and Kundu, 2010) are easily degraded by cells implanted into the scaffold matrix, but suffer from poor mechanical strength, interbatch variation, and immunogenicity and are a possible source of disease transmission (for example vCJD, HIV). Some effort has been made to improve the mechanical strength through impregnation with biomimetic minerals such as calcium phosphate (Cromme *et al*, 2007), but they are still more widely used in the form of hydrogels to encapsulate cells or bioactive medications, or for skin or soft tissue analogues - such as replacement liver tissue (Griffith, 2000) - than they are for load bearing applications.

### 1.4.2 Synthetic polymers

Conventional synthetic polymers (such as nylon, polyurethane, polymethyl methacrylate, HDPE and LDPE) are manufactured from compounds extracted from fossil fuels which are a declining and non-renewable resource. The extraction process that produces the raw material is not environmentally friendly and the product itself is incredibly stable and is therefore not biodegradable

Biodegradable synthetic polymers (including the poly(α-hydroxy acid)s polyglycolic acid, polycaprolactone and polylactic acid) are currently used in a number of biomedical applications such as sutures, dialysis media and drug delivery devices. They are biodegradable in that they can be broken down by hydrolytic mechanisms (triggered by heat or moisture) into shorter chain oligomers and eventually monomer form by the physical or physiological environment. They have been employed in the preparation of bioplastics (useful for producing ‘green’ loose-fill packaging), compost bags, food packaging and disposable tableware. In the form of fibres and non-woven textiles they have many potential uses as upholstery, disposable garments, awnings, feminine hygiene products and nappies.

#### 1.4.2.1 Polyglycolic acid (Polyglycolide)

Polyglycolic acid or Polyglycolide (PGA) is a biodegradable, thermoplastic polymer and is the simplest linear, aliphatic polyester (figure 1.1).

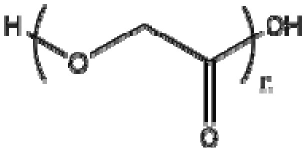

**Figure 1.1 Polyglycolic acid repeat unit**

PGA has been known since 1954 as a tough fibre-forming polymer. However, its hydrolytic instability has until recently limited its range of application (Gilding and Red, 1979).

*Thermal properties*

Polyglycolide has a glass transition temperature between 35-40 °C and its melting point is reported to be in the range of 225-230 °C. PGA also exhibits an elevated degree of crystallinity (45-55%) making it insoluble in water.

*Physical properties*

The solubility of this polyester is somewhat unique, in that its high molecular weight form is insoluble in almost all common organic solvents, whilst lower molecular weight oligomers are more soluble. Fibres of PGA exhibit high strength and modulus (7 GPa) (Middleton and Tipton, 2000).

*Manufacturing process*

Polyglycolide can be obtained through several different processes starting with different materials:

- polycondensation of glycolic acid;
- ring-opening polymerization of glycolide;
- solid-state polycondensation of halogenoacetates;
- acid catalyzed reaction of carbon monoxide and formaldehyde

Polycondensation of glycolic acid is the simplest process available to prepare PGA, but it is not the most efficient because it yields a low molecular weight product.

The most common synthesis used to produce a high molecular weight form of the polymer is ring-opening polymerization of glycolide, the cyclic diester of glycolic acid. Glycolide can be prepared by heating gycolic acid under reduced pressure, then collecting the diester by distillation (Figure 1.2).

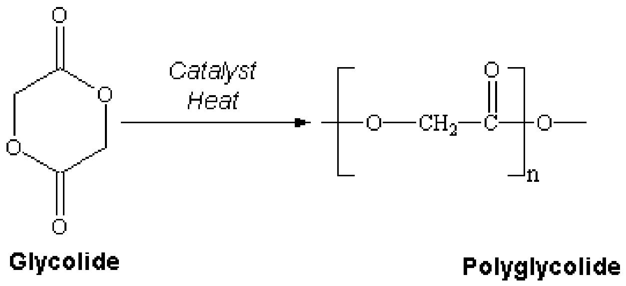

**Figure 1.2: Polyglycolic acid (polyglycolide) synthesis**

Ring-opening polymerization of glycolide can be catalyzed using different catalysts, including antimony compounds, (antimony trioxide or antimony trihalides), zinc compounds (zinc lactate) and tin compounds (tin octoate (tin(II) 2-ethylhexanoate) or tin alkoxides). Tin octoate is the most commonly used initiator, since it is approved by the FDA as a food stabilizer.

PGA can also be obtained by reacting carbon monoxide, formaldehyde or one of its related compounds like paraformaldehyde or trioxane, in presence of an acidic catalyst.

### *Degradation*

Polyglycolide is characterized by hydrolytic instability owing to the presence of the ester linkage in its backbone. The degradation process is erosive and appears to take place in two steps during which the polymer is converted back to its monomer glycolic acid: first water diffuses into the amorphous (non-crystalline) regions of the polymer matrix, cleaving the ester bonds; the second step starts after the amorphous regions have been eroded, leaving the crystalline portion of the polymer susceptible to hydrolytic attack. Upon collapse of the crystalline regions the polymer chain dissolves.

When exposed to physiological conditions, polyglycolide is degraded by random hydrolysis and it can also be broken down by certain enzymes, especially those with esterase activity. The degradation product, glycolic acid, is non toxic and it can enter the tricarboxylic acid cycle after which it is excreted as water and carbon dioxide. A part of the glycolic acid is also excreted by urine (Gunatillake *et al*, 2003).

*Applications*

The traditional role of PGA as a biodegradable suture material (in the form of copolymers (poly(lactic-*co*-glycolic acid), poly(glycolide-*co*-caprolactone) and poly (glycolide-*co*-trimethylene carbonate) has led to its evaluation in other biomedical fields. Implantable medical devices have been produced with PGA, including anastomosis rings, pins, rods, plates and screws. It has also been explored for tissue engineering or controlled drug delivery. Tissue engineering scaffolds made with polyglycolide have been produced following different approaches, but generally most of these are obtained through textile technologies in the form of non-woven meshes. (Kellomaki *et al*, 2000; Wang *et al*, 2000).

### 1.4.2.2 Polycaprolactone

Polycaprolactone (PCL) is a biodegradable thermoplastic, aliphatic and semi-crystalline polyester.

*Thermal properties*

PCL has a glass transition temperature of -65 to -60°C and a melt temperature of 56 to 60°C.

*Physical properties*

PCL is a semicrystalline polymer with a degree of crystallinity up to 69%. At room temperature, PCL is highly soluble in chlorinated hydrocarbons and aromatic hydrocarbons; slightly soluble in acetone or acetonitrile; and insoluble in alcohols, petroleum ether, diethyl ether and water (Sinha *et al*, 2004). PCL displays the rare property of being miscible with many other polymers, polycarbonates, nitrocellulose and cellulose butyrate, and is also mechanically compatible with others (polyethylene, polypropylene, natural rubber).

*Manufacturing process*

PCL is prepared by ring opening polymerization of ε-caprolactone using a catalyst such as stannous (tin) octanoate.

The polymerisation process of PCL is shown in figure 1.3

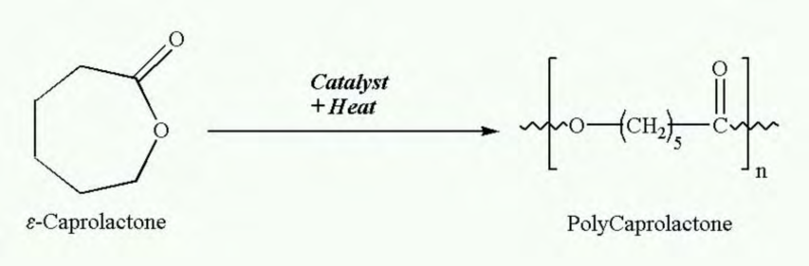

**Figure 1.3: Polycaprolactone synthesis**

PCL can be processed using a wide range of methods, although films produced by blowing are often tacky and as a result, compression moulding and melt extrusion from pellets is usually employed (Hutmacher *et al*, 2001). Solvent casting can also be used, but this method often utilizes high volumes of solvent and results in a material containing organic solvent residues, which may be difficult to remove.

Fibre bonding, particulate leaching, and melt moulding are also employed to produce both microparticles and polymeric scaffolds for biological applications (Hutmacher *et al*, 2000). More recently gas foaming utilising supercritical carbon dioxide has been utilised (Xu *et al*, 2004; Leeke *et al*, 2006).

### *Degradation*

PCL degrades within months to years depending on the molecular weight and degree of crystallinity of the polymer through hydrolysis of its ester linkages in the same manner as PGA. The amorphous phase is degraded first, resulting in an increase in the degree of crystallinity while the molecular weight remains constant (Lam *et al*, 2007). Then, cleavage of ester bonds results in mass loss (Sinha *et al*, 2004). The polymer degrades by end chain scission at higher temperatures, or by random chain scission at lower temperatures (Joshi and Madras, 2008). PCL degradation is autocatalysed by the carboxylic acids liberated during hydrolysis (Sinha *et al*, 2004) but it can also be catalysed by enzymes, resulting in faster decomposition (Chen *et al*, 2000).

### *Applications*

The inclusion of PCL in polyurethane formulations has been found to impart good water, oil, solvent and chlorine resistance to the material produced.

In biomedical applications, its main use is as a matrix for drug delivery systems and a variety of drugs have been encapsulated within PCL beads for controlled release and targeted drug delivery (Sinha *et al*, 2004**).** It is also suited to cell microencapsulation (Matzinos *et al*, 2002), due to its low processing temperature.

### 1.4.2.3 Polylactic acid (Polylactide)

The production of Polylactide (PLA) from the cyclic dimer (lactide) of lactic acid occurred as early as 1932 (Carruthers *et al*). Even before that, low molecular weight dimers and oligomers were detected on removal of water from an aqueous solution of lactic acid (Nef, 1914).

*Thermal properties*

PLA can be either amorphous or semicrystalline, depending on the stereochemistry and thermal history. For amorphous PLAs, the glass transition ($T_g$) determines the upper use temperature for most commercial applications. For semicrystalline PLAs, both the $T_g$ (~58°C) and melt temperature ($T_m$) 130°–230°C are important for determining the use of PLA across various applications.

The ($T_g$) increases with molecular weight ($M_n$) and optical purity (OP). Orientation and physical aging also affect the $T_g$. Physical aging affects the glass transition of PLA and can occur between about -45°C and $T_g$, the rate of aging increasing with increases in temperature (Witzke, 1997). The free volume reduction (a characteristic of physical aging) is observed by DSC as an endothermic volume expansion immediately after $T_g$ and is often referred to as the enthalpy of relaxation. Crystallization and orientation reduce the rate and extent of PLA aging.

The relationship between $T_g$ and the molecular weight of the polymer is described by the Flory -Fox equation:

$$T_g = T_g^{\infty} - K/M_n$$

[Eq.1.1]

Where $T_g^{\infty}$ is the $T_g$ at the infinite molecular weight, K is a constant representing the excess free volume of the end groups for polymer chains, and $M_n$ is the number average molecular weight. Literature values of $T_g^{\infty}$ are usually 57-58 °C and K is (5.5-7.3) x $10^4$ for PLA (Fox and Flory, 1950).

*Physical characteristics*

Having two optical arrangements for lactic acid (L-lactic acid, D-lactic acid), and three optical arrangements for lactide (L-lactide, D-lactide, meso-lactide), the variety of primary structures available for PLA is substantial. The physical characteristics of high molecular weight PLA are to a great extent dependent on its transition temperatures for common qualities such as density, heat capacity, and mechanical and rheological properties. Both $T_g$ and $T_m$ are strongly affected by overall optical composition, primary structure, thermal history, and molecular weight.

Above its $T_g$, an amorphous PLA will transition from glassy to rubbery and behave as a viscous fluid upon further heating. Below its $T_g$, it behaves as a glass with the ability to creep until cooled to its β transition temperature of approximately -45°C; Below this temperature it will only behave as a brittle polymer.

The most common commercial polymers of PLA are optical copolymers of predominantly L-lactide, with small amounts of D- and meso-lactides, made through bulk polymerization with tin octoate catalyst via ring-opening polymerization (ROP). While these copolymers are generally described as random, there is evidence of some degree of stereoselectivity (Thakur *et al*, 1998). Condensation polymerization of L-lactic acid with small amounts of D-lactic acid, polymerized in solution, has also been used. The optical co-monomers introduce kinks in PLAs natural helical conformation and defects in the crystal arrangement, resulting in depression of the melting point, reduction in the level of attainable crystallinity, and reduction in the rate of crystallisation. Optical purity (OP) is a common nomenclature to describe polymers of this variety. As OP decreases < 0.78, crystallization eventually becomes impossible and the polymer is amorphous.

By varying the amount and the sequence of D-lactide units in the polymer backbone the product properties can be changed. Polymers with a high L-lactide content can be used to produce crystalline polymers, whilst higher meso- or D-lactide contents within the polymer (>15%) make it more amorphous. It is also possible to solvent or melt blend the meso- , L- or D- forms of PLA so that they undergo stereocomplexation (racemic) crystallisation (Tsuji *et al*, 2000, 2001, 2004, 2008). These changes impact melt behaviour, thermal properties, barrier properties, and ductility.

### *Manufacturing process*

All plants (including cereal crops) convert the energy of the Sun via the process of photosynthesis into starch. The crop is harvested, and a ‘mash’ of the cereal crop kernels is made in order to separate the starch from the other components. The starch is converted to glucose through enzyme hydrolysis and is then fermented by bacteria to produce lactic acid (figure 1.4). Lactic acid is a chiral molecule and can exist in two different forms (figure 1.5). The lactic acid is fed into a continuous condensation reaction to produce low molecular weight PLA prepolymer, which is then depolymerised into a mixture of lactide stereoisomers using a catalyst to enhance the rate and selectivity of the intramolecular cyclisation reaction. The molten lactide mixture is then purified by vacuum distillation.

Finally, high molecular weight polymer is produced using a tin-catalysed, ring-opening lactide polymerisation in the melt. After the polymerisation is complete, any remaining monomer is removed under vacuum and recycled to the beginning of the process (Green and Kunneman, 2006; Natureworks publication).

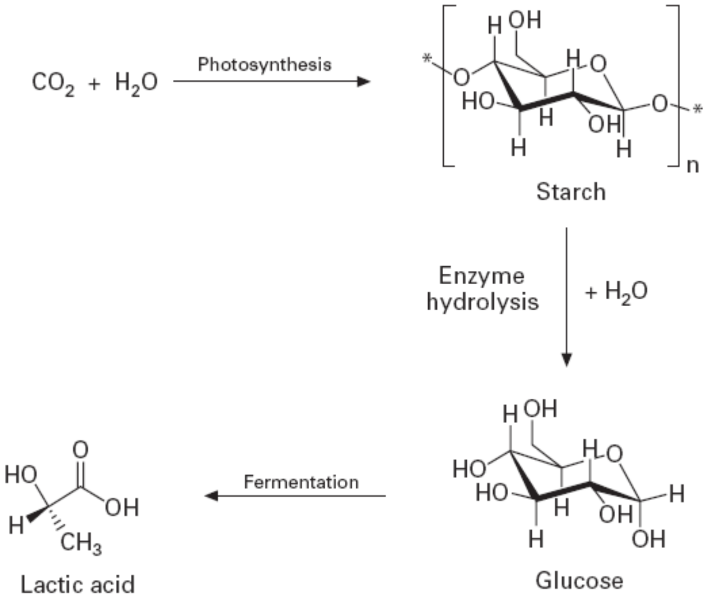

**Figure 1.4: Lactic acid synthesis**

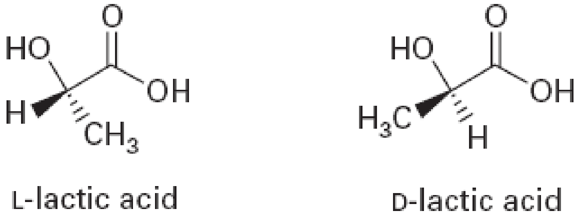

**Figure 1.5: Stereoisomers of lactic acid**

This process relies heavily on bacterial fermentation of glucose in aqueous slurry with a continual addition of a base (such as calcium hydroxide) to maintain a neutral pH and thereby ensure that optimum amounts of lactic acid is ionized (Drumright, 2000).

Isolation of the lactic acid and removal of water requires that a strong mineral acid, such as sulphuric acid, be added to protonate the lactate salt, while at the same time producing a mole of salt for every two moles of acid produced. On a weight basis, about a pound of salt per pound of acid is produced. This significant amount of waste salt contributes to the cost of the lactic acid and is undesirable from a sustainability point of view. The process is being further developed to contain an organism that is tolerant of temperature and acidic conditions and be combined with lactic acid removal technology that does not result in the generation of waste salts. This process will be more cost effective to the company and beneficial to the environment.

Lactic acid can be polymerised to form PLA via two methods (figure 1.6); direct condensation of lactic acid, or via a cyclic intermediate called lactide, through a ring-opening process. Direct condensation of lactic acid involves the removal of water by condensation and the use of a solvent under high vacuum and temperature and there is increased racemisation (production of a mix of the L- and D- form in the polymer chain) with this method, and only low to intermediate molecular weights can be produced which have little commercial viability.

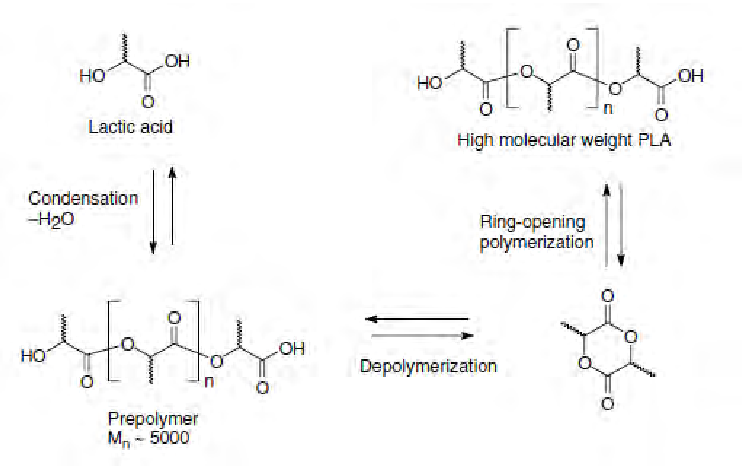

**Figure 1.6: Production of lactide and polylactic acid**

The ring opening process is more widely and successfully used since it allows for the production of high molecular weight PLA. The first step in the process produces the cyclic intermediate lactide (a lactic acid dimer) with three potential forms; L-lactide, D-lactide and L, D- or D, L-lactide, called meso-lactide (figure 1.7).

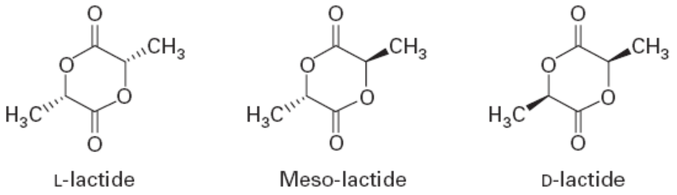
L-lactide
Meso-lactide
D-lactide

**Figure 1.7: Isomeric forms of lactide**

Polymerisation of the lactide is accomplished at 180$^{o}$C-210$^{o}$C, in the presence of a catalyst (usually tin octoate at levels of 100-1000 ppm) for around 2-5 hours (figure 1.8). The purity of the lactide is better controlled (which results in less racemisation) and it is possible to produce a wide range of molecular weights through addition of hydroxyl containing compounds. Conversion rates of ~95% with <1% impurities have been achieved.

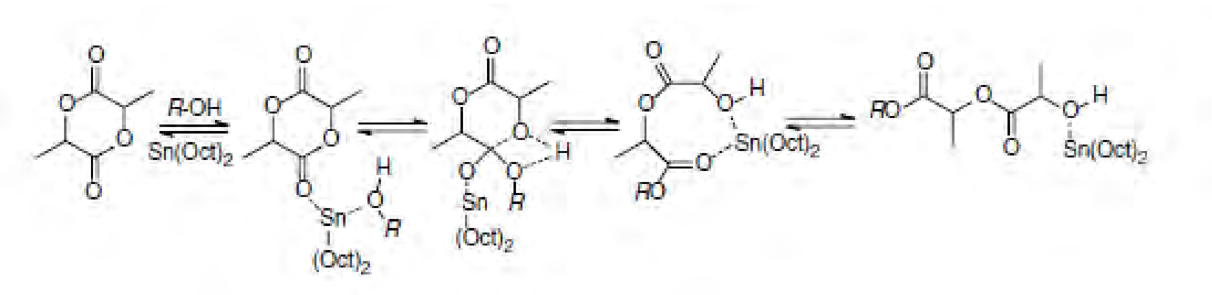

**Figure 1.8: Schematic of co-ordination insertion chain growth mechanism of lactide to PLA**

A patented, low-cost continuous process for the production of lactic acid-based polymers has been developed by Cargill Dow (under the trade name Natureworks) (figure 1.9). The process combines the environmental and economic benefits of synthesising both lactide and PLA in the melt rather than in solution.

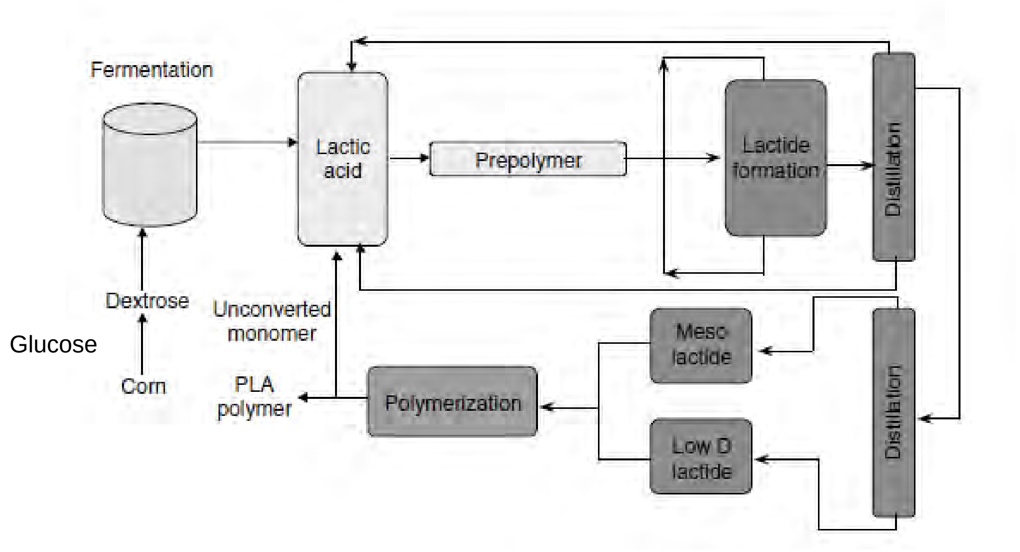

**Figure 1.9: The Cargill Dow non-solvent process to produce PLA**

(Figures 1.1-1.9, adapted from Drumright, 2000).

*Degradation*

PLA is very susceptible to thermal degradation above 180°C and issues with PLA melt stability during processing and rheological testing have been frequently documented (Witzke, 1997; Dorgan *et al*, 2000).

Degradation reactions include: chain scission due to hydrolysis of the ester linkage; random mid-chain scission resulting in lactide formation; depolymerisation; and transesterification to esters or low MW lactide. The kinetics for melt hydrolysis are dependent upon water concentration, acid or base catalysis, and polymerization catalyst concentration. The proton in the CH group of the main chain of PLA is labile and it has been suggested that the proximity of this labile proton to the ester group affects the thermal sensitivity of the polymer (Ramkumar and Bhattacharya, 1998).

Pre-processing, hydrolysis can be reduced or essentially eliminated with conventional drying operations where water is removed prior to melting. However, when PLA is exposed to a humid environment following drying, moisture is quickly reabsorbed into the polymer up to its equilibrium level of swelling.

The rate of the hydrolytic degradation of PLA is determined by the degree of crystallinity; amorphous forms may degrade in weeks, whereas crystalline forms may take months or even years (Garlotta, 2001).

The degradation behaviour of PLA will be discussed further in section 1.3.

### *Applications*

PLA is ideally suited for many applications in the environment where recovery of the product is not practical, such as agricultural mulch films and bags. Composting of postconsumer PLA items is also a viable solution for many PLA products (such as sandwich wrappers).

PLA resins can be tailor-made for different fabrication processes, including injection moulding, sheet extrusion, blow moulding, thermoforming, film forming, or fibre spinning. This is achieved by controlling molecular parameters in the process such as branching, D-isomer content, and molecular weight distribution and selectively incorporating L-, D-, or meso-lactide stereoisomers into the polymer backbone (Drumright, 2000).

PLA is an FDA approved material, and in fibre form has been used as a suturing material, for drug or cell encapsulation (Whang *et al*, 2000; Frank *et al*, 2004; Ginty *et al*, 2005) and more widely in tissue engineering applications as a scaffold material (Kellomaki *et al*, 2000; Lin *et al*, 2003; Duarte *et al*, 2009).

### 1.4.3 Composites

Polymer scaffolds themselves have poor mechanical integrity and tend to collapse when put under load, and while biocompatibility has been demonstrated in animal models they have only really been successful in minimal load bearing situations (Mathieu *et al*, 2006). Composites that include a ceramic (Cyster *et a*l, 2003; dos Santos *et al*, 2005) or bioactive glass (Kellomaki *et al*, 2000) as a filler in the scaffold structure have been made successfully, and improve its mechanical properties even though they are fragile and brittle when used alone (Tancret *et al*, 2006). An overview of the literature surrounding the inclusion of bioceramic material and bioglass into polymer scaffolds follows.

#### 1.4.3.1 Polymer-bioceramic composites

Composite materials (made by the addition of a ceramic to the polymer) have been shown to have enhanced mechanical properties; biocompatibility, calcification and cell proliferation are also improved, since the degradation products of the ceramic are thought to offset any decrease in pH associated with degradation of the polymer material. Ceramic materials are usually calcium phosphate based, and those that are most commonly used are hydroxyapatite, tricalcium phosphate (Kellomaki *et al*, 2000; Mathieu *et al*, 2006) or potassium enhanced calcium phosphate (Gburek *et al*, 2004).

### 1.4.3.2 Polymer-bioglass composites

It has been noted in many laboratory texts (including that of Davis, 2001) that cell adhesion is enhanced on glass surfaces, particularly if the glass has high silica content, or has previously been used. This is due to the cells binding to extracellular matrix components that are adsorbed to the surface of the glass. Commercial available biologically active glass (bioglass) typically has a high silica and/or phosphate content and its incorporation into polymer scaffolds has been shown to enhance cell attachment and growth. Polyactive® (Du *et al*, 2002), bioglass 13-93 (Kellomaki *et al,* 2000), bioglass 45S5 (Chen *et al*, 2007 and 2010; Boccaccini *et al*, 2003) and phosphate glass (Brauer *et al*, 2006), or proprietry made glass (Vallet-Regi, 2000, and *et al*, 2002) have all been used with some degree of success.

## *1.5 Scaffold manufacture*

There are many ways in which polymers can be formed into scaffolds but most involve organic solvents or other chemicals that makes them unsuitable for use within a physiological system due to the toxic effect that residual amounts of these chemicals may have on cells. The techniques themselves are not consistent and can have variable outcomes depending upon the experience of the operator performing them. Methods including (but not restricted to) solvent casting-particle leaching, computer aided design related technologies (such as 3D printing), emulsion freeze drying and liquid-liquid phase separation fall within this category (Quirk *et al*, 2003).

One other method that is already widely used in the paint industry and other non-biological industries is the use of supercritical fluids (Harris and Mooney, 1998). This process uses a gas to create pores within the scaffold (known as ‘gas foaming’ of the polymer), thereby negating the need for use of large volumes of organic solvents. The most commonly used gas is carbon dioxide as it is widely available, carbon neutral and produces no environmentally damaging by-products.

### 1.5.1 Solvent casting – particle leaching (SCPL)

**T**his approach allows the preparation of porous structures with regular porosity, but with a limited thickness. First the polymer is dissolved into a suitable organic solvent (e.g. polylactic acid could be dissolved into dichloromethane), then the solution is cast into a mould filled with porogen particles, such as be an inorganic salt like sodium chloride, crystals of saccharose, gelatin spheres or paraffin spheres. The size of the porogen particles will affect the size of the scaffold pores, while the polymer to porogen ratio is directly correlated to the amount of porosity of the final structure. After the polymer solution has been cast the solvent is allowed to fully evaporate, then the composite structure in the mould is immersed in a bath of a liquid suitable for dissolving the porogen: water in case of sodium chloride, saccharose or gelatin, and an aliphatic solvent like hexane for paraffin. Once the porogen has been fully dissolved a porous structure is obtained. Other than the small thickness range that can be obtained, another drawback of SCPL lies in its use of organic solvents which must be fully removed to avoid any possible damage to the cells seeded on the scaffold.

### 1.5.2 Emulsion freeze drying

This technique does not require the use of a solid porogen like SCPL. First a synthetic polymer is dissolved into a suitable solvent (e.g. polylactic acid in dichloromethane) then water is added to the polymeric solution and the two liquids are mixed in order to obtain an emulsion. Before the two phases can separate, the emulsion is cast into a mould and quickly frozen by means of immersion into liquid nitrogen. The frozen emulsion is subsequently freeze-dried (lyophylised) to remove the dispersed water and the solvent, thus leaving a solidified, porous polymeric structure. Emulsion and freeze-drying allows a faster preparation compared to SCPL since it does not require a time consuming leaching step, but it still requires the use of solvents. Pore size is relatively small and porosity is often irregular. Freeze-drying by itself is also a commonly employed technique for the fabrication of scaffolds. In particular it is used to prepare collagen sponges: collagen is dissolved into acetic acid or hydrochloric acid and then cast into a mould, frozen with liquid nitrogen then lyophylised (Wang *et al,* 2000 and 2005).

### 1.5.3 Phase separation

**S**imilar to emulsion freeze drying, the phase separation procedure requires the use of a solvent with a low melting point that is easy to sublime. For example dioxane could be used to dissolve polylactic acid, then phase separation is induced through the addition of a small quantity of water: a polymer-rich and a polymer-poor phase are formed. Following cooling below the solvent melting point and some days of vacuum-drying to sublime the solvent a porous scaffold is obtained. Liquid-liquid phase separation presents the same drawbacks of emulsification/freeze-drying.

### 1.5.4 Computer aided design (CAD) and computer aided manufacture (CAM)

**S**ince most of the above described approaches are limited when it comes to the control of porosity and pore size, computer assisted design and manufacturing techniques have been introduced to tissue engineering. First a three-dimensional structure is designed using CAD software, then the scaffold is created by using ink-jet printing of polymer powders (Roy *et al*, 2003; Lewis and Gratson, 2004), or through fused deposition modelling of a polymer melt (Reckow and Ricci, 2006).

### 1.5.5 Supercritical fluids (SCFs)

A supercritical fluid is any substance at a temperature and pressure greater than its thermodynamic critical point. All materials in the liquid and gas phase have a temperature above which the densities of the liquid and gas phases become equal, resulting in the formation of a single phase. $CO_2$, a non-toxic gas with a relatively low critical point (Tc = 31°C (304.1 K), Pc = 73.8 bar (7.376 MPa) is most widely used in the supercritical fluid field. Figure 1.9 shows the pressure-temperature graph for $CO_2$ and its critical point.

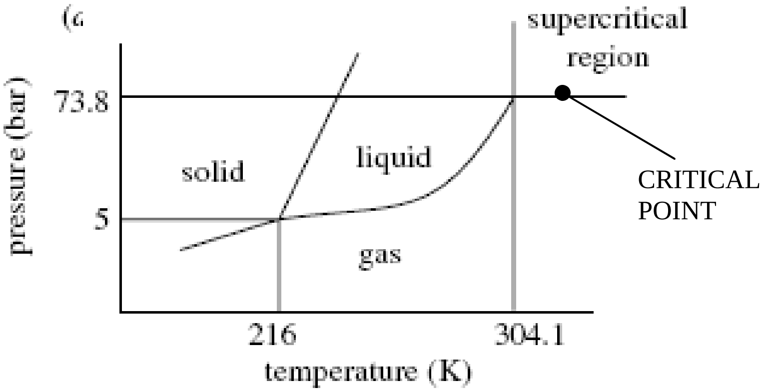

**Figure 1.10: Pressure-temperature graph for $CO_2$ (McHugh, 1994)**

In this form, $CO_2$ can diffuse through solid materials like a gas and dissolve them like a liquid, making it a substitute for many organic solvents.

How dense and viscous the supercritical fluid is, and therefore how well it behaves as a solvent is very much dependent on the temperature and pressure of the system and both of these can and need to be very finely controlled. In the case of supercritical $CO_2$ ($scCO_2$), the viscosity is ten times more than that of a gas but five to ten times less than that of a liquid.

### 1.5.6 SCF processing of polymers (gas foaming)

Polymer foams are formed when a polymer, heated to a temperature above its melt temperature is plasticised by saturation of the supercritical fluid under high pressure and constant temperature. As the pressure is released the SCF reverts to its gaseous form, and pockets of gas nucleate and grow in the polymer. As the supercritical fluid leaves the polymer, the $T_g$ increases. At the point where the $T_g$ for the polymer is higher than the foaming temperature, the porous structure is set. However, scaffolds produced through the gas foaming technique have a tendency to possess an outer ‘skin’ and to have a closed non-connected pore network; the solvent casting-particle leaching approach has been proven to address these issues, but also adds to processing complexity and time.

Gas foaming is a multi-step process: 1) A SCF has to be dissolved in a liquefied polymer under pressure; this creates a thermodynamically stable system; 2) There has to be a period of time to allow homogeneous dispersion of the SCF throughout the molten polymer; 3) The system is then depressurised, creating a thermodynamic instability which results in nucleation of the gas molecules, thereby creating pores as the polymer resolidifies.

The anisotropy of the scaffold structure that has been formed can be altered by controlling the cooling rate of the foamed polymer and hence the density of gas nucleation. Rapid cooling has been found to lock in large numbers of spherical pores, whilst slower cooling enabled pore elongation (providing that no coalescence occurred). Incorporation of ceramic modifiers was also found to influence the process, reducing porosity and surface area due to modification of the polymer viscosity (Mathieu *et al*, 2006).

Each of these stages in the process will be discussed in turn.

### 1.5.6.1 SCF dissolution

The solvent properties of $scCO_2$ (the solubility of polymer in $scCO_2$ and the solubility of $CO_2$ in the polymer) are the key to success in SCF processing, and while many pharmaceutical agents and polymers have demonstrated low solubility in $scCO_2$, it is the high solubility of $scCO_2$ in many polymers that can be particularly advantageous and can lead to dramatic decreases in the glass transition temperature ($T_g$) or melting temperature

($T_m$) thereby reducing polymer melt viscosity (Tomasko *et al*, 2003; Nalawade *et al*, 2006 (a); Lee *et al*, 2006).

Both $CO_2$ solubility and diffusivity in polymers are influenced by the molecular structure (the interaction between $CO_2$ and the molecular chains) and the polymer morphology (crystalline or amorphous regions).

While the polymer chain flexibility can aid dissolution of $CO_2$, carbonyl or ether groups that are accessible in the backbone or on side chains can cause steric hindrance by specifically interacting with the $CO_2$. Polymers with ether groups (like polyethylene glycol) display stronger interactions than polyesters due to weak Lewis acid–base interaction (Nalawade *et al*, 2006 (b)).

Although polylactide (PLA) and polylactide acid-co-glycolide (PLGA) have the same chemical structure in the main chains, the stearic hindrance close to the carbonyl group (in PLGA) and accessible free volume caused by methyl pendant groups (in PLA) can lead to the differences in their solubility. However, the accessible free volume in the polymers (which allows the $CO_2$ to diffuse into them more easily) was found to have a greater effect on solubility than the interaction between $CO_2$ and the polymers (Shah *et al* 1993). Therefore, the solubility of $CO_2$ in PLGA copolymers decreased with increasing glycolide content (Tai *et al*, 2010).

The solubility of $CO_2$ in PLA with two different L:D contents has also been studied, and it was found that $CO_2$ was more soluble in amorphous PLA 80:20 than in PLA 98:2 with 20% crystallinity (Oliveira *et al*, 2006). PGA, PEG and PCL are also highly crystalline polymers and $CO_2$ does not easily diffuse into these at temperatures below their melting points, leading to low solubility. In contrast, $CO_2$ has a high solubility in amorphous poly-$_{D,L}$-lactic acid (PDLLA) because it has larger free volume.

### 1.5.6.2 SCF 'soak' time

During the soak stage the polymer melt absorbs an amount of $CO_2$ that is a function of temperature, pressure and time.

Some reports in the literature suggest that the foaming process of semi-crystalline polymers should be performed by applying a soak temperature higher than the polymer $T_m$, in order to destroy the crystal phase and to guarantee a homogeneous absorption of $scCO_2$ by the melt polymer during the soak stage (Gualandi *et al*, 2009).

Crystallization from the melt can occur during foaming; $CO_2$ acts as a plasticiser (lowering resistance to chain rotation) decreasing both $T_g$ (Fox, 1956) and $T_m$ (Flory, 1953); The polymer crystallization window (the range between $T_g$ and $T_m$), becomes more narrow and shifts towards a lower temperature, with crystallization rate depending on $CO_2$ concentration.

In one study, the foaming of several semi-crystalline polymers with different degrees of crystallinity was investigated. The foaming process was performed at a constant temperature below each polymer melt temperature ($T_m$); the results showed that pores were not homogeneously distributed in the samples, nor was foaming present at $T<T_m$ if the degree of crystallinity was higher than 30-50%. It was therefore hypothesized that pore growth only occurred in the amorphous domains (Doroudiani *et al*, 1996).

### 1.5.6.3 Depressurisation and cooling

During the final stage of the process, nucleation and growth of $CO_2$ bubbles occur;

According to classical nucleation theory, the activation energy that must be overcome in order to create stable nuclei depends on pressure gradient, concentration gradient and temperature. Nucleation density and bubble growth rate depend on the rate of depressurization and on cooling rate (Tomasko *et al*, 2003).

### 1.5.6.4 Disadvantages of gas foaming

A non-porous film (a ‘skin’) is formed on the surface of the scaffolds, making cell penetration difficult, and presenting a barrier for the influx of cell nutrients and the efflux of the waste products of cellular metabolism. This surface skin is thought to be formed by the rapid diffusion of the $CO_2$ from the surface of the scaffold to the uppermost edge of the scaffold as the pressure is released. Subsequent analysis of scaffolds formed during this process showed them to have a relatively closed pore network (Mooney *et al*, 1996).

In the aforementioned study, these issues were overcome by incorporation of a porogen (sodium chloride crystals) into the polymer prior to the gas foaming procedure. Upon production of the polymer foam, the porogen was leached out by soaking in water. The scaffolds created in this manner had an interconnected pore network open to the surface, which was successfully used to culture smooth muscle cells (Harris *et al*, 1998). Interconnectivity of the pores was found to be improved even further by partially fusing the salt porogen by exposing it to 95% humidity (Murphy *et al*, 2002).

The leaching of the porogen is a major disadvantage of the gas foaming/particulate leaching process since it is time consuming and can result in loss of any incorporated pharmaceutical agents.

As the porosity of the scaffold increases so its mechanical strength decreases, an important factor in many biomedical applications and especially in weight bearing tissues such as bone. It appears to be that there is an upper limit to pore size and degree of porosity, above which pore size and low mechanical strength precludes their use in certain applications (Barry *et al*, 2006).

## 1.6 Degradation of PLA

The hydrolytic degradation of polylactide and associated co-polymers (Agrawal *et al*, 1995; Jain, 2000; van Nostrum *et al*, 2004), and the bulk degradation of the polylactide 'end products' (Gopferich, 1997; von Burkersroda *et al*, 2002; Chen *et al*, 2010) have been extensively studied. Two mechanisms of chain degradation have been documented: chain-end scission and random chain scission.

The chain scission of a polymer is called 'random' if the bonds at any position along the polymer chain have the same probability of being cleaved. The hydrolytic degradation of polymers causes the main chain to break down randomly via cascades of irreversible scission steps following simple first-order kinetics, irrespective of the chain length of the polymer molecules involved. The molecular weight distribution shifts towards the lower end of the range as the degradation progresses and a distinguishable peak in the low molecular weight region, then finally in the monomer range is formed.

In the case of chain-end scission, the number of chain ends and the rate constant for the cleavage of the terminal bond are the essential kinetic parameters. Several factors such as the vicinity of a polar group at the chain end can enhance the attraction of water molecules by the chain end and lead to a preferred hydrolysis of the terminal ester bonds. In this case, the molecular weight of a chain linearly decreases over time. A constant initial generation rate of scission products in case of chain-end scission follows from the fact that the number of chains, and thus the number of chain ends, is not changed during this initial period of degradation. In the final stage of degradation this rate decreases gradually, as the shorter chains became completely degraded and cannot contribute to the generation of scission products anymore. The degradation process is completed when the longest chain fraction is completely degraded.

From the point of view of organic chemistry, the hydrolysis of biodegradable polymers is a bimolecular nucleophilic substitution reaction (*SN2*), a second order reaction that can be catalyzed by the presence of either acids or bases (Figure 1.11). The fundamental chemical reaction mechanisms of most hydrolytically biodegradable polymers are thought to be well understood. However, due to the long-chain structures and condensed states of polymers, the detailed hydrolysis of such polymers is much more complicated. For example, polymer bonds in their homopolymers may hydrolyse at different rates compared to that in their copolymers, or the polymer bonds near the chain ends may have a different reactivity from those in more remote sites (van Burkesroda, 2002); likewise, the reactivity in crystalline domains may be different from that in amorphous domains (Tsuji, 2000 & 2001). Also, the diffusion behavior of water, ions, and degradation products (chain segments) are all different and can lead to many transport related phenomena such as autocatalysis (hydrolysis products or chain ends that catalyse the hydrolysis reaction itself) (Li *et al*, 1990 a and b).

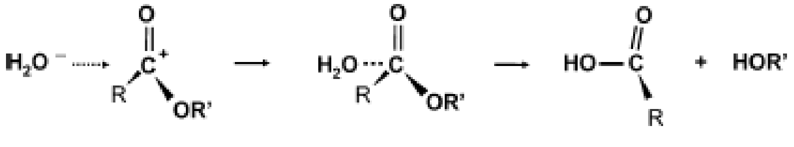

**Figure 1.11: Schematics of ester hydrolysis - nucleophilic substitution reaction (*SN2*)**

A study of the influence of different terminal groups on the hydrolytic degradation of oligolactides revealed that the degradation mechanism and kinetics was strongly dependent on the nature of the chain ends (van Nostrum *et al*, 2004). In neutral and basic media the degradation of acetylated oligomers (those ending in a $COCH_3$ group) occurred more slowly than in hydroxyl-terminated oligomers. The preferred degradation of short hydroxyl-terminated oligomers via chain-end scission based on a backbiting mechanism is considered to account for this observation; Chain-end scission was reported to be more than 100 times faster than random chain scission of hydroxyl-terminated lactic acid oligomers.

With an increasing number of ester bonds in longer oligomer chains and for high molecular weight PLA, the probability of random chain scission was found to be increased because of the small number of chain ends.

The occurrence of bulk degradation or surface erosion in a PLA and PLGA bulk samples has been explained in terms of the diffusivity of water inside the polymer, the hydrolysis rate and a critical dimension of the degrading object (van Burkersroda *et al*, 2002). The variation of the pH of the eroding medium was used to analyse the influence of acid or base catalysis on the erosion kinetics. Autocatalysis due to the accumulation of acidic degradation products was reported to be a determining factor for the erosion of PLA and PLGA, with the variation of the polymer molecular weight influencing both the chain-scission kinetics and the diffusivity of water into the polymer.

Studies on monolayers of polymer films have been carried out in Langmuir troughs, and these contribute to the knowledge of surface erosion degradation kinetics, but the monolayer method has limits when it comes to studying bulk erosion characteristics. In one such experiment (Kulkarni *et al*, 2007) it was concluded that – in addition to the findings of van Nostram *et al* - the terminal end group (hydroxyl or carboxylic acid) the water diffusion constant would be a key factor for the development of improved bulk hydrolytic degradation models. The penetration kinetics of water into the polymer bulk material and the transportation of the eroded material out of the sample would also have to be accounted for in any such model.

Bulk erosion degradation is generally accepted as following third-order kinetics (Pitt *et al*, 1981). The rationale behind this theory is that the hydrolysis rate depends on the concentration of the polymer bonds, water, and the acidic hydrolysis products (but not the $H^+$ itself). This theory predicts a linear relationship between the logarithm of the polymer molecular weight with degradation time. This prediction fits a number of experimental observations, but a few exceptions have been reported (Dunne, 2000; Deng, 2005). The theory does not, however, consider the effects of transport processes of polymers on degradation. Hence, it cannot be used to treat the phenomena related to transport such as surface erosion. A second order mechanism based on combined reaction and transport was then proposed (Lyu *et al*, 2005), which was extended to include surface erosion. The erosion velocity and the size of reaction zone were calculated as functions of the hydrolysis rate and the diffusion coefficient of water.

### 1.6.1 Autocatalysis

The hydrolysis of polyesters can produce acidic products (-COOH) in the chain ends which further catalyse the reaction. Due to the restricted diffusion of the chain ends, the acidic polymer fragments can accumulate inside samples and cause faster degradation in the inner part of the specimens (Li and McCarthy, 1999). Such phenomena were more profound in large-sized specimens and non-buffered testing media.

### 1.6.2 The effect of temperature on degradation

Temperature can also affect the degradation kinetics (Tsuji, 2001; Deng, 2005; Tsuji, 2005) and this is not only important to predict the resorbable behavior of the devices *in vivo* but also extremely useful to develop an accelerated degradation test method, since with some polymers degradation can take more than 3 years (Tsuji, 2000). An *in vitro* degradation study of PLGA fibres, performed over a temperature range of 27.5-47.5 °C (Deng, 2005) documented that changes in the strain at break of the material was found to obey the Arrhenius equation. Another experiment with polycaprolactone (PCL) conducted at very high temperatures (>100 °C) (Tsuji, 2001) observed Arrhenius behavior was as well. However, accelerated degradation behaviour is not necessarily indicative of degradation behaviour in an *in vivo* situation at $37^{o}$C.

The degradation of a polymer may also be dependent on sample size, material processing, composition, and morphology since these are all factors that would affect the development of water diffusion channels at nanoscale, found to be critical to the bulk degradation of certain materials (Sousa, 2006).

### 1.6.3 Hydrolysis of PLA in neutral media

A large number of investigations have been performed on the hydrolytic degradation behavior of PLLA in neutral media such as phosphate-buffered solution (PBS) (Agrawal *et al*, 2000), Ringers solution (Wang *et al*, 2006), and water (Lyu *et al*, 2007). The molecular weight and crystallinity are the crucial factors that determine the hydrolytic degradation of biodegradable polyesters; however, there have been contradictory results obtained. It was observed that PLGA with higher molecular weight degraded faster in PBS than those with lower molecular weight, and that the degradation of PDLLA microspheres had a similar dependence on molecular weight (Wang *et al*, 1998). In contrast, faster degradation of PLLA specimens in PBS with lower crystallinities has also been documented (Li *et al*, 1990; Alexis *et al*, 2004).

The presence of stereoisomers of PLA was also found to have an effect on degradation rate; the hydrolytic degradation rate of an amorphous PDLLA film in PBS was found to be much higher than that of an amorphous PLLA film (Tsuji, 2002). The main conclusions of the same study were that the hydrolytic degradation rate constant of PLLA and PLA/PCL copolymer films increased with the increasing water absorption (hydrophilicity), with decreasing initial glass transition temperature, or with the L-lactide unit sequence length, indicating that the hydrolytic degradation rate of the copolymers is closely related to these three parameters. It was also concluded that rapid crystallisation of L-lactide unit sequences in PLA/PCL film caused an uneven pattern of degradation, probably due to the formation of crystalline residues.

In a long term study involving the amorphous and semi-crystalline (Xc 1.6 %) stereoisomers of PLA, in the time period up to 32 weeks the incorporation of small amounts of D-lactide units (~1%) enhanced the hydrolytic degradation of PLLA in PBS (more so than molecular weight), due to decreased interactions of the PLLA chains with D-lactide units. In the period after this (up to 60 weeks) neither D-lactide content nor molecular weight was a crucial parameter to determine the rate of degradation, due to the onset of autocatalysis. The initially amorphous films remained amorphous even after the hydrolytic degradation for 60 weeks, while the Xc of the semi-crystalline PLLA film increased to 9% during the same time period. The hydrolytic degradation up to 32 weeks decreased their elongation-at-break significantly, but after 60 weeks there were no further significant effects on the tensile strength and Young's modulus of PLLA films. (Saha and Tsuji, 2006).

In buffered pH media, autocatalysis seemed to be suppressed around neutral pH (Li *et al*, 1990) which suggested that it might happen preferentially at low pH. However another study on low pH buffered solutions found that the autocatalysis was not enhanced (Gopferich, 1997), so the effect of the pH of the media on the degradation is still not well understood, and it is not known whether the presence of -COOH or $H^+$ is responsible for it. However, in another study (Tsuji, 2004) the hydrolysis of the crystalline regions was accelerated with the pH deviation from 7, showing that the $H^+$ and OH- ions had a catalytic effects on the hydrolysis of the crystalline residues, and that the catalytic effect of OH- ions on the hydrolysis of the crystalline residues was much higher than that of $H^+$ ions.

Studies involving the spherulite size, crystallinity ($X_c$) and lamella thickness ($L_c$) of PLLA films found that films with higher initial $X_c$ underwent faster hydrolysis due to the fact that a higher $X_c$ film would have a higher $L_c$ and that this would produce more defects in the amorphous region thereby promoting hydrolysis by enhancing water diffusion. The radius of spherulites had an insignificant effect on the hydrolysis of PLLA films in phosphate-buffered solution (Tsuji, 2004).

In related studies, it was found that the hydrolysis of crystallised PLLA at a temperature below its melting temperature ($T_m$) proceeded predominantly in the chains in the amorphous regions, leaving the chains in the crystalline regions untouched or even resulting in the formation of crystalline residues, irrespective of the hydrolysis media.

### 1.6.4 Enzymatic hydrolysis of PLA

Much discussion has been generated regarding the role of enzymes in relation to the breakdown of synthetic polymers. Tissue esterases have been implicated in the breakdown of PGA (Hermann, 1970), as have proteinase K and bromelain (Williams, 1981); Pancreatin has been used to degrade PDLLA (Landry and Bazile, 1996); and lipase has been used to successfully degrade PCL (Gan *et al*, 1999). Of all of the enzymes documented in the literature, proteinase k predominates.

Proteinase K is a fungal protease that can be extracted from the mold *Tritirachium album*. The enzymatic hydrolysis of PLLA is affected by a variety of factors including highly ordered structures, molecular characteristics and polymer blending (Tsuji, 2002). The enzymatic hydrolysis rate is faster in the amorphous region than in the crystalline region (Li, 1999). In addition, the hydrolysis resistance of PLLA chains in the free amorphous region (outside spherulites) has been found to be lower than in the restricted amorphous region (inside spherulites) as evidenced by preferential etching of these regions when viewed by SEM (Tsuji, 2001). Studies of the enzymatic hydrolysis of PLLA single crystals using proteinase K and concluded that their enzymatic hydrolysis proceeds at the disordered chain packing region of the crystal edges rather than at their chain folding surfaces (Iwata and Doi, 1998).

The addition of $CaCO_3$ particles to amorphous PLLA composite films up to 10 wt% enhanced enzyme hydrolysis by proteinase K, and it was concluded that the addition of small amounts of the $CaCO_3$ particles was effective to make the PLLA films susceptible to enzyme hydrolysis at the interface between the PLLA matrix and the $CaCO_3$ particles as well as on the film surfaces when compared to unmodified PLLA film (Fukuda, 2002). Enzymatic hydrolysis rate of the PLLA films was found to decrease monotonously with increasing initial $X_c$ and $L_c$; Proteinase K was also found to have no catalytic effects on the hydrolysis of the crystalline residues (Tsuji, 2004).

## 1.7 Mineral deposition by simulated body fluid (SBF)

The bone-bonding ability of a material is often evaluated by examining the ability of apatite to form on its surface in a simulated body fluid (SBF) with ion concentrations nearly equal to those of human blood plasma (Jayasuriya *et al*, 2006).

Artificial materials implanted into bone defects generally become encapsulated by a fibrous tissue, leading to their isolation from the surrounding bone. However, early studies utilising Bioglass found that it spontaneously bonded to living bone without the formation of surrounding fibrous tissue (Hench *et al*, 1972). Since then, several types of biologically active ceramics and glasses (section 1.2) have also been shown to bond to living bone, and they are used clinically as important bone substitutes. However, these ceramics are not mechanically compatible with the surrounding bone.

It was subsequently shown that a silica rich layer and calcium phosphate film formed on the surface of Bioglass when implanted in the body environment, which allowed it to bond to living bone, and that the *in vivo* formation of the calcium phosphate film could be reproduced in a buffer solution consisting of Tris- hydroxy-methyl-amino-methane and hydrochloric acid (Tris buffer solution) at pH 7.4. (Hench *et al*, 1980). Other studies found that on implantation of a glass-ceramic in a living body, the silica rich layer did not form although the calcium phosphate layer did, still facilitating bonding to living bone (Kitsugi *et al*,1987). This calcium phosphate layer was later identified as a crystalline apatite by micro X-ray diffraction (Kokubo *et al*, 1990 (1)), and that its *in vivo* apatite formation on the surface of the glass-ceramic could be reproduced in an acellular SBF with ion concentrations nearly equal to those of the human blood plasma, but not in a Tris buffer solution. The formation of apatite on the surface of Bioglass in SBF has also been independently confirmed (Kokubo *et al*, 1990 (2); Hench *et a*l, 1993).

Detailed analysis of the surface apatite formed in SBF showed that it was similar to bone mineral in its composition and structure (Kokubo *et al*, 1990 (1 & 2). It was therefore proposed that osteoblasts might preferentially proliferate and differentiate to produce apatite and collagen on its surface, and that apatite formed in this way might bond to the surface apatite as well as to the surrounding bone. In contrast, glass-ceramics that were unable to bond to living bone were found to be lacking this apatite layer on their surface both *in vivo* and in SBF (Kitsugi *et al*, 1989; Kokubo *et al*, 1990 (2)). It was therefore concluded that an essential requirement for an artificial material to bond to living bone was the formation of bonelike apatite on its surface when implanted in the living body, and that this *in vivo* apatite formation could be reproduced in a simulated body fluid (SBF) with ion concentrations nearly equal to those of human blood plasma (Kokubo *et al*, 1991), meaning that the *in vivo* bone bioactivity of a material could be predicted from the apatite formation on its surface in SBF.

## *1.8 Bone*

Bone is a highly complex and multifunctional tissue. In addition to providing support to the body, protection for delicate organs and facilitating movement, it fulfils a number of less obvious roles including mineral storage and blood cell production. In order for a tissue engineered implant to be successful it must be able to mimic, support and promote the processes in the same way as natural bone would.

### 1.8.1 The structure and properties of bone

Bone contains approximately 60-70 % by weight hydroxyapatite crystals (calcium phosphate, $Ca_{10}(PO_4)_6OH_2$) and 30-40 % by weight type I collagen (as the bone matrix) which accounts for 85% - 90% of the total bone protein. Small amounts of cell attachment proteins, proteoglycan, osteocalcin, and growth factors make up the remainder. The mineralisation of the matrix is regulated by associated cells (osteoblasts) that can detect applied load by means of mechanoreceptors and remodel the bone accordingly (Salter *et al*, 1997).

### 1.8.2 Bone formation

In the embryo, bone formation begins when mesenchymal stem cells (MSCs) form condensations (clusters of cells) that adhere through the expression of adhesion molecules. In a few areas of the body the cells of these condensations differentiate directly into bone-forming osteoblasts. These cells lay down a matrix particularly rich in type I collagen through intramembranous bone formation. In all other parts of the body the cells become chondrocytes, the primary cell type of cartilage; cells at the border of condensations form the perichondrium. Chondrocytes have a characteristic shape, secrete a matrix rich in type II collagen and proteoglycans. The cartilage enlarges through chondrocyte proliferation and matrix production. Chondrocytes in the centre of the cartilage mould then stop proliferating, enlarge (hypertrophy), and begin to synthesize type I collagen. The hypertrophic chondrocytes direct bone growth through initiating mineralization of their surrounding matrix, and attract blood vessels through the production of vascular endothelial growth factor (VEGF) and other factors. They also direct adjacent perichondrial cells to become osteoblasts; these secrete a characteristic matrix, forming a bone collar (which in turn forms the periosteum as it grows in size). They then undergo apoptotic cell death, the cartilage matrix left behind providing a scaffold for osteoblasts and blood vessels to lay down a true bone matrix within it forming the primary spongiosa. Continued proliferation of the chondrocytes enlarges the bone establishing secondary ossification centres. In the long bones of the limb, growth chondrocytes continue to proliferate between the primary and secondary ossification centres. This cartilage is then called the growth plate, as it forms a distinct plate of cells between the bone of the secondary ossification centre and the primary spongiosa. At the top of the growth plate, round chondrocytes no longer proliferate rapidly and are called resting or reserve chondrocytes. In humans, growth plates disappear at the time of adolescence after a burst of pubertal activity (Kronenberg, 2003).

## 1.8.3 Bone cells

Four specific cell types are found in bone and they have a particular spatial distribution and specific function.

### 1.8.3.1 Osteoprogenitor cells

These cells are mesenchymal stem cells found on the inner lining of the periosteum and endosteum, which differentiate into osteoblasts when exposed to appropriate growth factors (eg bone morphogenic proteins, BMPs; fibroblast growth factor, FGF; and platelet derived growth factor, PDGF).

### 1.8.3.2 Osteoblasts

These cells secrete the extracellular matrix and alkaline phosphatase, which calcifies the matrix. They lie on the surfaces of the existing bone matrix as a continuous layer - on the periosteum (at the periosteal border) and in the endosteum - and synthesise the organic constituents of the bone (LeBlond and Wright, 1981). They secrete a range of proteins including type 1 collagen, alkaline phosphatase (ALP) and osteocalcin.

### 1.8.3.3 Osteocytes

These are osteoblasts that have become trapped within the newly deposited layer of bone. They are found in lacunae, between the layers of lamellae and in the matrix of cortical bone. The osteocyte is thought to be involved in the homeostasis of minerals and may play a part in the response of bone to applied stresses. Osteocytes gain the nutrition required for survival by diffusion through the network of canaliculi by which they are linked. The death of osteocytes results in the local destruction of bone matrix (Williams *et al*., 1989).

### 1.8.3.4 Osteoclasts

Large and multinucleate, these cells (polykaryons) are derived from monocytes; they contain many lysosomes and mitochondria; they are responsible for the breakdown of bone. They interface with bone via a ruffled border and integrin receptors, which provides a high surface area for the transfer of enzymes to degrade the protein matrix and to allow the absorption of the decomposition products (see ‘bone remodelling’). An increase in the activity of osteoclast cells can be observed in diseases such as osteomyelitis resulting in localised osteoporosis.

### 1.8.4 Remodelling (‘coupling’)

Bone mass in adults is driven by serum levels of calcium, and is maintained locally by the balance of bone resorption by osteoclasts and bone formation by osteoblasts, both of which are subject to control by a host of complex intermediate pathways involving stress receptors, paracrine regulators and hormones. However, resorption occurs much more quickly than rebuilding (2-3 weeks as opposed to 2-3 months respectively, for the same bone mass) so bone loss can result even when increased resorption is accompanied by increased formation.

#### 1.8.4.1 Resorption

When exposed to parathyroid hormone, bone lining cells secrete enzymes that remove the outer cover of the matrix allowing osteoclasts to enter. The osteoclast cell body is polarised and undergoes internal structural changes that prepare it to resorb bone, and a tight junction between the bone surface and basal ‘ruffled’ membrane of the cell body forms a sealed compartment (vacuole). This vacuole is then acidified through the action of endosomes containing protein pumps that move to the ruffled border and insert into the cell membrane. Secretion continues with the export of acidophilic lytic enzymes into the rapidly forming resorption pit (Howship’s lacunae). Degradation products (collagen fragments and soluble calcium and phosphate ions) may be phagocytosed and digested within the osteoclast and released into the circulation (figure 1.11) (Boyle, 2003).

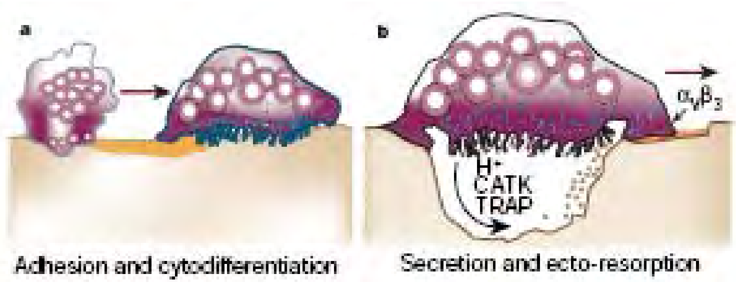

**Figure 1.12: Activation of bone resorption.** a**, Activated multinucleated polykaryons adhere to bone and undergo cell differentiation into a mature osteoclasts;** b, **formation of Howships lacunae and digestion of bone by acidophilic enzymes (CATK and TRAP).**

(Adapted from Boyle, 2003)

### 1.8.4.2 Rebuilding

Osteoblasts in the bone lining cells form new bone in the area that has just undergone resorption. There are two steps to matrix mineralisation: nucleation of calcium phosphate crystals, and then crystal growth.

*Nucleation*

Nucleation can occur either heterogeneously or homogeneously.

Homogeneous nucleation is the formation of crystals due to supersaturation of the local environment with the appropriate ions. It is thought that this could occur in the lumen of matrix vesicles. These are small, membrane-bound vessels of cellular origin. Active transport (ion pumps) may be used to raise the amount of calcium and phosphate in the vesicles to levels above supersaturation. In addition, matrix vesicles protect unstable intermediates, making them ideal locations for nucleation. Crystals are found first on the inner face of the membrane because some of the components of the vesicle membrane are known to have a high affinity for calcium, indicating a combined homogeneous/heterogeneous nucleation mechanism.

Heterogeneous nucleation occurs only at surfaces where the interaction between the surface and the ions lowers the interfacial energy requirement so that nucleation can proceed at concentrations that are less than that of supersaturation. The main example of this in bone calcification is found with collagen-mediated deposition. A heterogeneous nucleator must have both a strong affinity for the ions of the crystal and suitable topography so that a nuclear cluster can be easily formed. Collagen alone meets neither of these requirements, but certain non-collagen proteins (NCPs) such as osteonectin and some phosphoproteins have high affinities for calcium and these, when bound to collagen, form nucleators *in vivo*. It is thought that nucleation may occur because phosphate is adsorbed to the collagen and therefore is in close proximity to the calcium associated with the NCPs.

### *Crystal formation*

After nucleation, amorphous calcium phosphate precipitates and is converted first to octacalcium phosphate and finally to hydroxyapatite. The crystals in the matrix vesicles disrupt the membrane; the newly released crystals fuse and collagen-mediated precipitation predominates. After both types of nucleation, the first small crystals quickly grow from the whole regions in the collagen molecules to the overlap regions, where they are aligned along the fibre axis. The crystal size is determined by inter-fibre space constraints as well as via chemical inhibitors of growth such as pyrophosphates, which bind competitively to the collagen sites that bind NCPs.

### 1.8.5 Control of bone formation and resorption

Certain cytokines and growth factors are required for osteoclast differentiation and activation (Khosla, 2001). Their function is to induce gene expression of other enzymes and receptor cell proteins, and to activate transmembrane signalling receptors found on osteoblasts; these factors and proteins coordinate bone remodelling by stimulating bone resorption by local osteoclasts, which in turn stimulate bone synthesis by closely adjacent osteoblasts by a process called ‘coupling’.

There are several levels of control of the cell signalling pathway that enhance or dampen osteoclast production and activation: negative control of any of the signalling pathways can occur through the secretion of soluble proteins which preferentially bind the transmembrane proteins on osteoblasts, inducing release of interferons which then down-regulate the expression of factors involved in osteoclast development; the binding of calcitonin to its receptor is known to inhibit osteoclast activation and is the basis for its use as a therapeutic agent in the prevention of osteoporosis, although the molecular mechanism of action is unclear; or, calcitropic hormones, pro-resorptive cytokines and parathyroid hormone related peptides have been shown to up-regulate expression of transmembrane receptors in osteoblast cell lines and primary cell cultures.

The T cell is also an important source of cytokines in the bone. Activation of T cells *in vitro* and *in vivo* leads to increased osteoclast production and bone resorption, suggesting that acute and chronic inflammatory states and certain types of leukaemia, contribute to pathologic bone loss.

## 1.8.6 Types of bone

### 1.8.6.1 Woven bone

The bone first produced by proliferating chondrocytes is immature woven bone (Sikavitsas, 1997). It is rich in osteocytes with large spaces around the blood vessels, and has small collagen fibrils which are randomly orientated. This bone will be remodelled to form cortical bone which has a more highly organised structure.

### 1.8.6.2 Cortical (lamellar) bone

Cortical bone (also known as compact or lamellar bone) accounts for ~80% of the adult human skeleton. It is almost solid (around 9.1% porous) with spaces only for osteocytes, canaliculi and blood vessels.

Cortical bone is generated more slowly than woven bone and is less mineralised. The collagen fibres are thicker and are arranged in layers (lamellae), and the fibres extend between the layers increasing their strength. The lamellae in turn can be stacked flat or arranged in concentric circles around blood vessels (forming the Haversian canals). Canaliculi (small collagen fibrils) extend outwards from the centre of the canal to provide blood supply to the osteocytes. The Haversian canal and its associated osteocytes are termed an osteon. The central canals branch and eventually join Volkmann canals which run perpendicular to them and ultimately connect to the periosteal surface (figure 1.12).

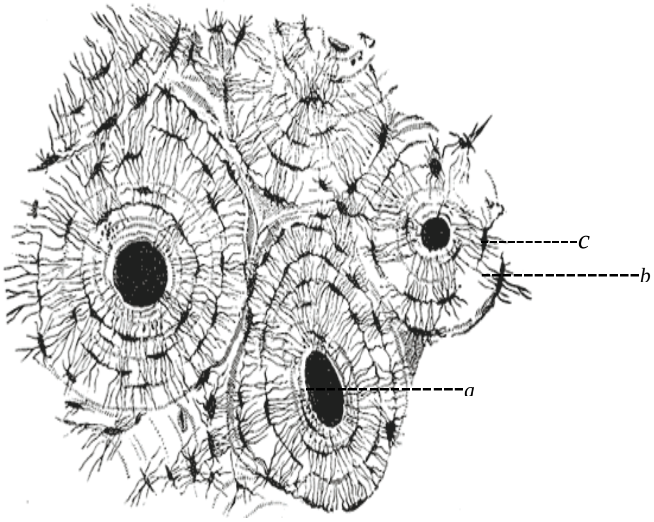

**Figure 1.13: Cross-section through lamellar bone showing three complete osteons (Schafer, 1954).**

a: Haversian canal; b: Lacunae containing osteocytes; c: canaliculi

### 1.8.6.3 Cancellous bone

Cancellous bone (also known as trabecular or spongy bone) accounts for the remaining 20% of the adult human skeleton. It is lighter and less dense than compact bone and also more porous 50-90% porosity). It consists of a network of bars, plates and rods (trabeculae) of bone adjacent to small irregular cavities containing bone marrow and osteocytes. (Buckwater, 1996). There is no Haversian canal; instead canaliculi connect adjacent cavities to receive a supply of blood. Although the structure appears irregular it follows lines of stress and can be rearranged to provide maximum strength. Cancellous bone can be converted to cortical bone by further mineralisation of the trabecular network (Currey, 1984).

## 1.8.7 Distribution and relative proportions of cortical and cancellous bone

Long bones are divided into 3 physiological sections: The epiphysis lies between the physis (growth plate) and the bone and is covered in cartilage; the diaphysis is the long narrow part of the bone; the metaphysis is the transition area between the wide ‘ends’ of the bone and the diaphysis. Cancellous bone is found mainly in the metaphysis, while cortical bone is found in the diaphysis. However, cortical bone is often layered over cancellous bone to improve mechanical properties. (Buckwater, 1996). Generally, cortical bone is distributed with its Haversian canals orientated parallel to the primary axis of loading and cancellous bone is located either in areas subject to high impact forces or where the bone is loaded from a multitude of directions.

### 1.8.8 The clinical need for bone replacement

Osteogenic cells present in bone can repair minor defects caused by trauma or surgery. However, if the defect is too large to allow spontaneous healing, bone graft materials may be used to restore functional integrity and prevent scar tissue formation. Bone grafts may also be used in the augmentation of bony contours to correct skeletal deformities.

Trauma as a result of accident or injury or any one of a number of diseases can require that the affected bone be surgical removed or modified so that a bone graft or repair is necessary. These diseases are: Osteomyelitis (a bacterial infection, caused by *Staphylococcus aureus*); Osteoporosis (a condition whereby the sufferer loses bone mass at a rate higher than the bone loss associated with ageing); Osteosarcoma (removal and treatment of cysts and bone tumours usually involving complete resection of the affected tissue); and congenital disorders (such as cleft palate).

#### 1.8.8.1 Types of bone graft

*Autograft*

An autograft is bone harvested from one site in the patient and placed in another. The autograft remains the most frequently used grafting material since it is recognised by the body as ‘self’ and so does not elicit an adverse immunological reaction. In dental applications the bone is most often harvested from the jaw, whereas in orthopaedic applications where a larger volume of bone is often required the graft is most frequently taken from the iliac crest, tibia or a section of the ribcage.

The use of autograft in bone augmentation is far from ideal. A number of disadvantages associated with its use have stimulated research activity to find a suitable alternative. One of its major disadvantages is the limited quantity of bone suitable for grafting; from the iliac crest of the average adult, there is only 21ml of bone suitable for grafting and in the case of patients suffering from osteoporosis there may be even less (Sandor *et al*, 2003). Autografting procedures also increase the operative time and inevitably result in an increase in blood loss.

*Allograft*

The shortcomings of autograft material have led workers to investigate allograft material for use in bone grafting. Allograft material is harvested from a member of the same species prior to placement. This material is available in plentiful supply, but its use is limited by the risks of disease transmission and immune response.

*Xenograft*

Xenografts are harvested from one species and implanted into another. The use of most xenograft tissues is excluded because of a vigorous immune response on implantation leading to a high failure rate (Urist *et al*, 1994). By removing the protein from the bone, it is possible to reduce the extent of the immune response but this compromises the function of the osteoinductive matrix proteins. However, concerns over the risk of viral transfer from animal to human prompted the banning of xenografting in the UK in 1997 (Patience *et a*l., 1997).

## 1.9 The scope of this project

In this study, it was attempted to control the pore size distribution of a PLA scaffold material produced using a supercritical foaming process by incorporating silica particles into the polymer matrix.

Chapter 2 presents the methodology of scaffold production and preliminary analysis of porosity determined from geometrical measurements and of pore architecture by using scanning electron microscopy (SEM) and X-ray computed micro-tomography (microCT).

In order to assess the interconnectivity of the pores within the scaffold structure in a quantitative, non-invasive and non-destructive manner, visualisation and three dimensional (3D) measurements obtained using microCT were used to develop a greater understanding of the connectivity between and within both the polymer-silica matrix (the solid) and the pores, seeking to establish the true nature of the 3D pore networks within the scaffolds, and these results are presented in chapter 3.

Chapter 4 introduces the mechanical and physical properties of the scaffolds, and discusses the affect that the addition of silica to the polymer matrix has on pre and post SCF processing in terms of thermal behaviour (specifically Tg and Tm), degree of crystallisation and dynamics of crystal formation. These findings are evidenced through differential scanning calorimetry (DSC) and hot-stage microscopy. The affect of silica on the physical properties of the scaffolds is investigated through compression testing and results pertaining to Youngs modulus and ultimate compressive strength are discussed.

Chapter 5 is devoted to the investigation of the degradation behaviour of the scaffolds when exposed to both physiological saline and an enzyme solution in independently run studies, and also to mineral deposition pattern on exposure to simulated body fluids (SBF). The effect that the inclusion of silica has upon rate of degradation and the products produced are evidenced by high performance liquid chromatography (HPLC) and Fourier Transform Infra-red spectroscopy (FTIR); alteration in physical properties is presented in the form of thermal analysis (DSC), and visual assessment of the pattern of degradation on the scaffold architecture is made by microCT.

Chapter 6 presents a final summary of the conclusions from each chapter and chapter 7 presents some ideas for the ways in which this work can be developed further.

# Chapter 2: Scaffold manufacture

## 2.1 Introduction

The scope of the following experimental work was to produce scaffolds suitable for tissue engineering applications through the supercritical fluid gas foaming approach; also to address two of the issues typical of such scaffolds, namely low connectivity between pores, and the presence of an outer ‘skin’ - both artifacts from the production process (Mooney *et al* 1996).

In a novel adaptation of the SCF foaming process, it was proposed to incorporate a porogen (silica) into the polymer thereby making it an integral part of the scaffold material. Other particulate materials (such as sodium chloride) have been used with similar effect in solvent casting / particle leaching experiments but only in relatively thin films (Harris *et al,* 1998). In contrast to other particle leaching methods, in the experiments carried out in the work of this thesis, the silica was not washed away thus resulting in a simplified and shortened production process.

Silica (silicon dioxide, $SiO_2$) is a naturally occurring mineral (most commonly found as sand). It was chosen as the porogen because it is a major component (contributing up to 53% by weight) in many of the biologically active silicate glasses (such as bioglass or Polyactive®, section 1.4.3.2), which are purported to enhance the cell adhesion properties of the materials containing them. In addition, a silicate layer has been found to enhance the formation of carbonated hydroxyapatite on exposure to body fluids (Mathieu *et al*, 2006; Chen *et al*, 2005; Boccaccini *et al*, 2005), which in turn enhances bone cell growth. Inclusion of silicate glasses into a composite has also been shown to improve its mechanical properties (Nazhat *et al* 2001).

## 2.2 Materials

### 2.2.1 Polylactide

The polylactide used in this study was an injection moulding grade ‘meso’ blend of the L- and D-forms of the polymer, designated Poly($_{D,L}$)lactide ($P_{D,L}LA$), catalogue identification number 3051D. It was produced by Natureworks® LLC, Minnetonka, MN, USA and was obtained from RAPRA, UK. Other properties typical of this grade of polymer are given in table 2.1.

**Table 2.1: Physical and mechanical properties of $P_{D,L}LA$ 3051D (From Natureworks injection moulding document)**

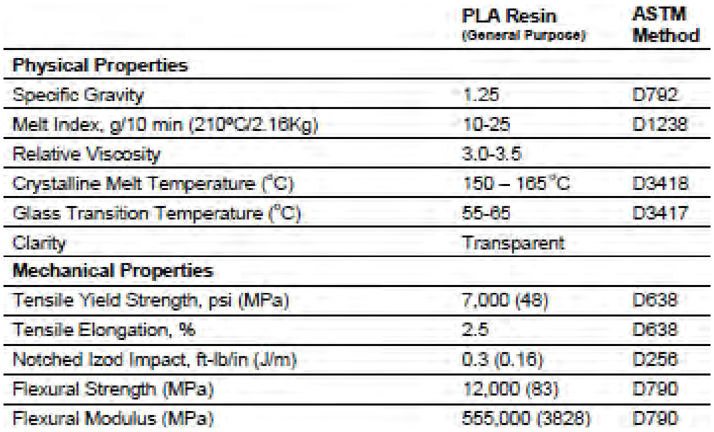

| | PLA Resin (General Purpose) | ASTM Method |
|---|---|---|
| **Physical Properties** | | |
| Specific Gravity | 1.25 | D792 |
| Melt Index, g/10 min (210ºC/2.16Kg) | 10-25 | D1238 |
| Relative Viscosity | 3.0-3.5 | |
| Crystalline Melt Temperature (°C) | 150 – 165 °C | D3418 |
| Glass Transition Temperature (°C) | 55-65 | D3417 |
| Clarity | Transparent | |
| **Mechanical Properties** | | |
| Tensile Yield Strength, psi (MPa) | 7,000 (48) | D638 |
| Tensile Elongation, % | 2.5 | D638 |
| Notched Izod Impact, ft-lb/in (J/m) | 0.3 (0.16) | D256 |
| Flexural Strength (MPa) | 12,000 (83) | D790 |
| Flexural Modulus (MPa) | 555,000 (3828) | D790 |

The $P_{D,L}LA$ in its ‘as received’ state was in the form of semi-crystalline pellets which were opaque in appearance; in its amorphous form the pellets would be transparent (figure 2.1)

**Figure 2.1: Visual appearance of ‘as received’ $P_{D,L}LA$ 3051D Left: Amorphous, transparent pellets; R: opaque, semi-crystalline pellets.**

#### 2.2.1.1 Characterisation of $P_{D,L}$LA 3051D

Experimental analysis of polarimetry and GPC was carried out by Lodz laboratories, Holland, independently of this study. The $P_{D,L}$LA 3051D was assessed by polarimetry to obtain rotatory power and hence optical purity, and by gel permeation chromatography (GPC) to determine molecular weight (Mn).

The results obtained for rotatory power and optical purity of the $P_{D,L}$LA 3051D indicated that the L content was 97.5% and that the D content is 2.5%.

The GPC analysis gave an estimation of number average molecular weight (Mn) of approximately 77,800 Da with a polydispersity index ($M_w/M_n$) of 1.17.

### 2.2.2 Silica

The silica used in this work as a porogenic agent was obtained from BDH chemicals, Poole, UK and the particle diameters were in the range 125 to 250 μm.

### 2.2.3 Choice of solvent: Dichloromethane

Polylactides have limited solubility and are only soluble in dichloromethane (Yureyev *et al*, 2008), dimethyl carbonate (Boccaccini *et al*, 2003) or trichloromethane (chloroform) (Tian and Tagaya, 2007). On the basis of the information contained in MSDS sheets, dichloromethane was deemed to be the least hazardous of these solvents.

HPLC grade dichloromethane (99.8% purity) was obtained from Riedel de Haën, Sigma Aldrich, UK.

## 2.3 Supercritical fluid foaming equipment

A schematic representation of the SCF processing equipment (rig) is provided in figure 2.2. Briefly, the rig consisted of a small capacity pressure vessel (autoclave) with integral pressure and temperature sensors, a gas inlet valve connected to a $CO_2$ source and an outlet valve connected to a flow rate monitor. The pressure vessel itself had a self contained heating jacket which was connected to an external circulator-heater bath. Full specifications of the pressure vessel, $CO_2$ cylinder and circulator-heater are shown in tables 2.2 and 2.3 respectively.

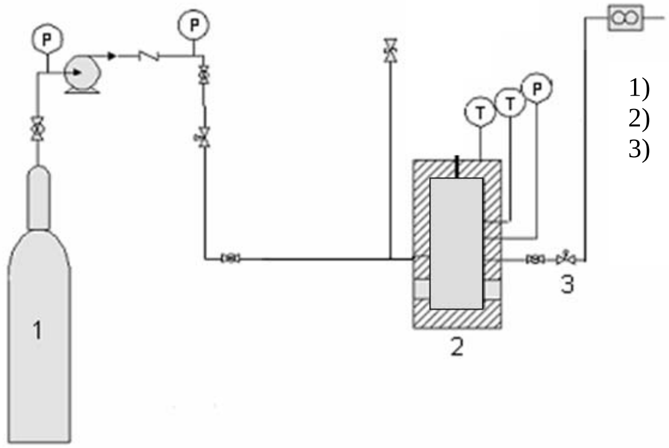

1) $CO_2$ cylinder
2) Pressure vessel
3) Outlet valve
T temperature sensor
P Pressure sensor

**Figure 2.2: A schematic diagram showing the rig used to process the scaffold materials**

**Table 2.2: Equipment specifications for pressure vessel**

| Component | | Manufacturer and Model number | Construction Material | Rated value |
|---|---|---|---|---|
| Pressure vessel | | Parr Instruments USA | Stainless steel T316 | 0-3000 psi (0-207 bar) |
| | Sapphire windows | n/k | Sapphire | 0-5000 psi (0-450 bar) @ 200 $^{o}$C |
| | Graphoil window seal | n/k | Carbon fibre | 0-5000 psi (0-450 bar) @ 200 $^{o}$C |
| Pressure vessel head | | Parr Instruments USA | Stainless steel T316 | |
| | Analogue pressure gauge | Ashcroft, UK (A151 316SS) | Composite plastic/stainless steel | 0-6000 psi (0-515 bar) |
| | Safety rupture disc | Fike Corp, USA (A5179-1-5) | Aluminium | 5000 psi (700 bar) @ 500 $^{o}$C |
| | Digital thermocouple | Digitron 3900 | Composite plastic | 0-999 $^{o}$C |
| | Digital pressure transducer | Druck, UK (PTX 1400 UK) | Composite plastic | 0-9999 bar |
| | Gas inlet ball valve | Swagelok UK (SS-3NRM4) | Stainless steel T316 | 6000 psi (515 bar) @ 38 $^{o}$C |
| | Gas outlet ball valve | Swagelok UK (SS-3NRM4) | Stainless steel T316 | 6000 psi (515 bar) @ 38 $^{o}$C |
| | Gas outlet needle valve | Swagelok UK (131SG2Y) | Stainless steel T316 | 5000 psi (450 bar) @ 38 $^{o}$C |
| Heavy duty stand | | Heidolph Instruments GmbH | Tempered steel | n/a |

**Table 2.3: Equipment specifications for peripheral components of the SCF rig**

| Component | | Manufacturer and Model number | Construction Material | Rated value |
|---|---|---|---|---|
| $CO_2$ cylinder | | BoC UK | Cast iron | 50 psi (1 bar) |
| | Analogue pressure gauge | Swagelok, UK<br>(SS-4354) | Stainless steel T316 | 0-3000 psi (0-207 bar) @ 38 $^{o}$C |
| | Gas flow ball valve | Swagelok UK<br>(SS-3NRM4) | Stainless steel T316 | 6000 psi (515 bar) @ 38 $^{o}$C |
| Manual pressure generator | | High Pressure Equipment Co, USA<br>(62-6-10) | Stainless steel T316 | 10,000 psi @ 30 cc per stroke |
| Heater | | Haake<br>(DC30) | Stainless steel T316 | 200 $^{o}$C |
| Circulator bath | | Haake<br>(B3) | | 250 $^{o}$C |
| | Hoses | Haake<br>(BLB-690-506C) | Stainless steel T316 with rubber insulation jacket | |
| | Synthetic Oil | Thermo Fisher<br>(CLR-500-047W) | | 20-210 $^{o}$C |

## *2.4 Methods*

### 2.4.1 Establishing optimum experimental conditions

Preliminary work had been carried out by another researcher which had set out some basic operating guidelines for the authors work to be based on. Briefly, PLA and PLA-silica composites were made as detailed in section 2.4.2, with silica additions of between 0% and 5% with respect to the mass of the PLA. These films were then subjected to gas foaming (148$^{o}$C, 150 bar, equilibration time of 30 minutes). The author attempted to replicate these experimental conditions without success, therefore the concentrations of silica to be added were reviewed, and the pressure and temperature of pressure vessel operation, and the depressurisation rate of the pressure vessel were adjusted (section 2.4.3). PLA films containing no silica were used initially until the desired scaffold structure was obtained.

### 2.4.2 Production of PLA-silica films

A solvent casting method was used to produce the scaffold material that was used in the supercritical foaming experiments. 1 g of PLA pellets were weighed out into a plastic weighing boat using a clean, dry, stainless steel spatula. The same Sartorius R160P digital balance (accurate to four decimal places) was used in this experiment and throughout all of the experiments that follow. Using a fume hood, 100 ml of dichloromethane (DCM) was measured out using a glass pipette and scrolling pipette filler, the DCM was immediately transferred to a glass 150 ml bottle. The weighed PLA pellets were added to the bottle, the bottle top was screwed on to finger tightness, and the bottle was then manually mixed by swirling for 30 seconds. The final concentration of PLA in DCM was 10% w/v. The complete dissolution of the

PLA took a minimum of 3 hours, so the sealed glass bottle was kept in the fume hood to facilitate removal of any evaporating DCM fumes.

Once the PLA had dissolved, silica was measured out using a clean stainless steel spatula and clean plastic weighing tray to achieve final concentrations of 2, 5, 10, 20, 30, 40, and 50 wt% content with respect to the PLA (see table 2.4 for details). The PLA-DCM-silica solution was manually agitated to obtain an even dispersion of silica throughout the dissolved polymer and was then poured into a shallow glass Petri dish. This in turn was placed onto an orbital shaker (under a fume hood) operating at ~60 rpm to allow sufficient evaporation of the solvent that the PLA-silica solution took on the appearance of very viscous treacle and the particles of silica remained suspended throughout the depth of the film. The shaker was then turned off and the Petri dishes were left under the fume hood overnight to allow the remaining solvent to evaporate.

The resulting film was peeled from the glass and cut into small pieces (2 mm × 4 mm × 1 mm) using a scalpel. These pieces were stored in labelled sealed glass bottles in the dark until required for use (one bottle was used for each silica concentration).

All procedures were carried out at ambient temperature and pressure.

**Table 2.4: Silica contents of solvent cast PLA films (final concentration of silica, with respect to total scaffold mass).**

| Mass of PLA (g) | Mass of silica (g) | Final % content silica |
|---|---|---|
| 1 | 0.00 | 0 |
| 1 | 0.02 | 2.0 |
| 1 | 0.05 | 4.8 |
| 1 | 0.1 | 9.1 |
| 1 | 0.2 | 16.7 |
| 1 | 0.3 | 23.1 |
| 1 | 0.4 | 28.6 |
| 1 | 0.5 | 33.3 |

## 2.4.3 SCF foaming process

In order to fabricate the scaffolds*, between 200 and 250 mg of the PLA-silica film was weighed out into clean plastic weighing trays using the same balance as before. Using forceps, the pieces of film were then placed into one of four stainless steel cylindrical moulds (internal diameter=10mm, height=20mm) lined with PTFE tape, which in turn were placed inside a small capacity pressure vessel of internal volume 25 $cm^3$ (manufactured by Parr Instruments; Illinois, USA). The lid of the pressure vessel was carefully lowered onto the base so as not to disturb the moulds and the retaining bolts were tightened. The inlet valve to the pressure vessel was opened to allow $CO_2$ (99.8% purity; BOC, UK) to fill the vessel to cylinder pressure (~ 50 bar). The circulator-heater bath (programmed to heat from 30 $^oC$ to 160$^oC$ at approximately 1 $^oC$ per minute) and was switched on; once this temperature was attained, the pressure inside the vessel was increased using a manual pressure generator until the pressure reached 160 bar and the $CO_2$ was in a supercritical state. These conditions were maintained for 2 hours to allow complete saturation of the $CO_2$ within the melted polymer (Nalawade *et al*, 2006; Li *et al*, 2006), before the outlet valves were opened and vessel was depressurised bringing it to ambient pressure. The rate of depressurisation was monitored by using a flowmeter. Once the internal vessel temperature had cooled sufficiently for it to be manipulated (~60$^{o}$C) the vessel was opened and the moulds and scaffolds were removed; once they had cooled to room temperature, the scaffolds were then removed from the moulds for further testing.

[*] It should be noted that depressurisation rate studies were carried out on 100 mg of 'as received' PLA beads, and not solvent cast films.

### 2.4.4 MicroCT

MicroCT was used to assess the pore size distribution, porosity, and homogeneity of silica within the scaffold. A bench top microCT scanner (model 1072, Skyscan, Belgium) was used to scan the scaffolds. The X-ray generation voltage was 50 kV and the current was 98 μA. The X-ray absorption distributions were converted to 2D images (a process called reconstruction) using Nrecon software and CTan software was used to assess the internal structure in 2D and 3D. 3D models based upon the CTan calculations were created using ANT software (all software provided by Skyscan, Belgium).

#### 2.4.4.1 Sample preparation and mounting

The scaffolds were scanned whole, with no further modifications. They were mounted on a brass stub and held in place by blu-tack prior to being inserted in the scanning equipment.

### 2.4.5 SEM

The internal scaffold structure was visualised by SEM, and the images obtained were compared to those generated by microCT in order to assess the accuracy of the microCT measurements. The SEM used was a Jeol JSM 840A (Jeol, Tokyo, Japan) set in low vacuum mode with a secondary electron detector operating at an accelerating voltage of 10 kV.

#### 2.4.5.1 Sample preparation and mounting

Using a scalpel, sections through the midpoint of each scaffold (~0.5 mm in thickness) were cut as uniformly as possible across as much of the full width of the scaffold as possible; Scaffolds containing 0% silica, 16.7% silica and 33.3% silica were used, and it was noted that the higher the silica content the more difficult it was to obtain a full width section due to the silica making the structure more likely to crumble. Hence the 0% silica section was a full width, the 16.7% silica section was ~ one third of the width and the 33.3% silica section was ~ one half of the width. The sections were mounted on carbon bases backed with a non-reactive adhesive onto brass stubs.

Non-conductive materials such as PLA have a tendency to accumulate electron charge, therefore a continuous line of silver graphite dag was painted down the side of the scaffold and across the mount, and a thin layer of gold was applied to the scaffold surface by sputter-coating. Both of these procedures served to conduct electrons away from the surface of the scaffold and hence obtain better images.

## *2.5 Results and discussion*

### 2.5.1 Development of experimental methodology

The appearance of the scaffolds after each experimental set-up was recorded and in this way, the optimum parameters for producing the scaffolds were derived. These observations are presented in Table 2.5.

**Table 2.5: Observations of the scaffold material made whilst optimising the process parameters**

| Temperature ($^{o}$C) | Equilibration time (hours) | Comments | **Depressurisation rate (L/min)** | **Comments** |
|---|---|---|---|---|
| 145 | 0.5 | No melt | 0.2 | Massive expansion overfills mould. Huge pores d ~ 1cm |
| | 1.0 | No melt | 0.5 | Moderate expansion, still over fills mould. Pores d ~ 0.5 cm |
| 150 | 0.5 | No melt | 1.0 | Moderate expansion, still over fills mould. Pores d~ 0.1 cm |
| | 1.0 | No melt | 1.5 | Moderate expansion fills mould level. Pores not measurable by eye. |
| 155 | 1.0 | No melt | 2.0 | Moderate expansion fills mould level. Pores not measurable by eye. |
| | 1.5 | No melt | 2.25 | Expansion half fills mould. Pores not measurable by eye. |
| | 2.0 | Partial melt (edges only) | | |
| 160 | 1.5 | Partial melt (edges and base) | | |
| | 2.0 | Full melt | | |

### 2.5.2 Calculation of relative porosity

The mass (m) of each scaffold (in grams) was recorded using the same Sartorius balance that was used to measure out the PLA-silica films prior to scaffold production. Using Vernier calipers, the height (h) and diameter (d) of each scaffold were measured (in cm) in triplicate – height in 3 positions approximately equidistant across the top of the scaffold; diameter in 3 positions approximately equidistant over the length of the scaffold - and the average height and diameter calculated (figure 2.3):

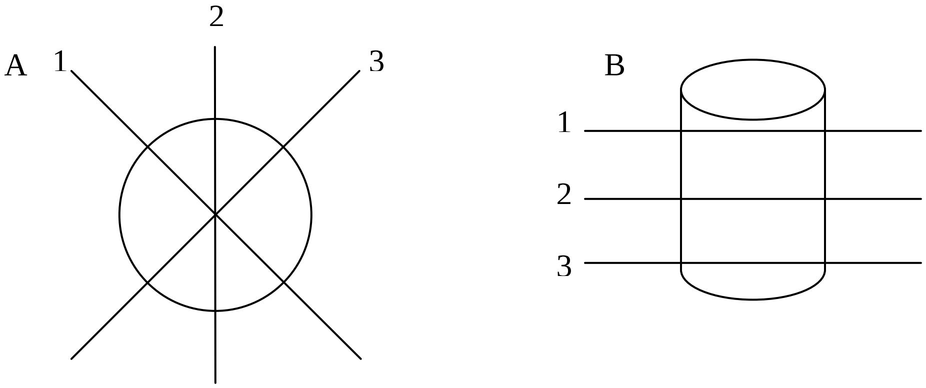

**Figure 2.3: A: Measurement of height of scaffolds (looking down onto the scaffold); B: Measurement of diameter of scaffolds (looking at the side of the scaffold)**

Diameter was converted to radius (r):

$$r = d/2$$

[Eq 2.1]

The volume (V) of each scaffold was then calculated, using the equation for a cylinder:

$$V=\pi r^2 h$$

[Eq 2.2]

The true (geometrical) density ($\rho_g$) was calculated from the scaffold mass and volume:

$$\rho_g = {}^{m}\!/\!_{V}$$

[Eq 2.3]

The theoretical density ($\rho_t$) can be described as the density the scaffold would have if it was a solid structure. It was calculated by taking into account the individual densities of silica ($\rho = 2.6$ g / cm$^3$) and PLA ($\rho = 1.24$ g / cm$^3$) and their relative proportions within each scaffold.

$$1/\rho_t = (m_1/\rho_1) + (m_2/\rho_2)$$

[Eq 2.4]

Where $m_1$ was the mass of PLA, $m_2$ was the mass of silica, $\rho_1$ was the density of the PLA and $\rho_2$ was the density of the silica.

The values obtained for true (geometrical) and theoretical densities were then used to calculate the percent density of each scaffold:

$$\%density = {}^{\rho_g}\!/\!_{\rho_t} \times 100$$

[Eq 2.5]

Percent porosity was directly calculated from percent density:

$$\%\ porosity = 100 - \%\ density$$

[Eq 2.6]

The arithmetic mean ($X$) and standard deviation ($s^2$) from the mean for % porosity was calculated for each of the 4 scaffolds ($x_1$, $x_2$, $x_3$, $x_4$) of each silica concentration (n = 4):

Arithmetic mean:

$$\mathrm{X} = \sum {}^{\chi}\!/\!_{n}$$

[Eq 2.7]

Standard deviation from the mean:

$$s^2 = \sum (x - X)^2 \big/ n - 1$$

[Eq 2.8]

### 2.5.3 Effect of depressurisation rate on the porosity and pore size of the scaffolds

Depressurisation of the pressure vessel containing the melted polymer resulted in the production of a foamed PLA scaffold material (figure 2.4).

**Figure 2.4: PLA scaffold, formed through the SCF foaming process**

### 2.5.4 Depressurisation rate studies

The geometrical measurements recorded and the subsequent calculations carried out were used to determine the porosity of the scaffolds obtained from both the depressurisation rate and pore nucleation experiments.

#### 2.5.4.1 Porosity

It was found that varying the rate at which depressurisation occurred allowed some control over the total porosity of unmodified PLA scaffolds (figure 2.5). Slow depressurisation of the vessel at 0.2 L/min resulted in scaffolds with an average porosity of 83.4 ± 1.2%, whereas a more rapid rate of depressurisation (2.25 L/min) resulted in the formation of PLA scaffolds with an average porosity of 64.6 ± 2.0%.

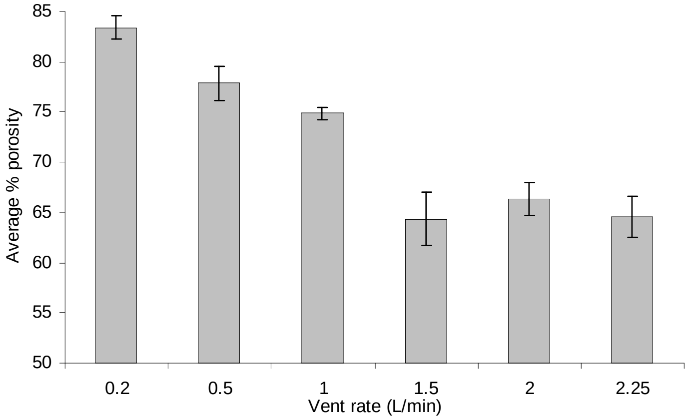

**Figure 2.5: The influence of depressurisation rate on the porosity of PLA scaffolds containing 0% silica obtained through gas foaming at 160$^0$C and 160 bar with vent rates as stated**

**Error bars indicate standard deviation from the mean (n=4)**

This apparent decrease in porosity with the increase in depressurisation rate can be explained by classical nucleation theory. In the case of the PLA scaffolds made from L or D lactide alone, nucleation of gas bubbles (potential pores) would be homogeneous, occuring only at nucleation sites on surfaces in contact with the molten polymer-the sides of the moulds. In classical homogeneous nucleation theory (Colton and Suh, 1987; Han and Han, 1990; and Goel and Beckman, 1994 a), the creation of a nucleus implies the formation of an interface at the boundaries of the new phase. Some energy is expended to form this interface, based on the surface energy of each phase. If the radius of a hypothetical nucleus is too small, the energy that would be released by forming its volume is not enough to create its surface, and nucleation does not proceed; beyond this critical radius size the phase transformation becomes more and more favourable, thereby allowing progressively smaller nuclei to become viable. Eventually, thermal activation will provide enough energy to form stable nuclei which can then grow until thermodynamic equilibrium is restored.

However the polylactide used in these foaming experiments was a L/D blend, and the D component would have provided sufficient structural discontinuity to the structure of the polymer chain to act as additional sites for bubble nucleation, so part of the nucleation process should therefore be considered to be heterogeneous; that is to say that nuclei would form either throughout the continuous (L-L or D-D) portions of polymer phase, or at an interface (L-D portions) within the material in addition to those that form at the interfaces with the mould. Heterogeneous nucleation has been shown to occur more readily than homogeneous nucleation (Mooney, 1996; Baldwin, 1995).

Some of the energy released in heterogeneous nucleation is by the partial destruction of the previous interfaces. For example, if a carbon dioxide bubble was to form between the molten polymer and the inside surface of the mould or the surfaces of adjacent L– and D–lactide portions of the polymer chain, the energy inherent in the polymer-mould or polymer-polymer interface would be released wherever a layer of gas intervened, and this energy would go toward the formation of bubble-polymer and bubble-mould interfaces.

However, there are many shortcomings relating classical nucleation and bubble growth theory to molten polymers as noted in the published literature (Shukla and Koelling, 2009; Kim, Kang and Kwak, 2004), hence no one theory has universal acceptance, and the mathematical discussion as such is outside of the remit of the experiments carried out in this study.

### 2.5.4.2. Pore size

Using the data for ‘structure separation’ from the microCT analysis as an indication of pore size, a pore volume distribution for each scaffold was obtained using the calculations that follow.

The arithmetic mean ($X$) and standard deviation ($s^2$) from the mean for each value of structure separation (interpreted here as pore diameter) was calculated for each of the 4 scaffolds ($x_1$, $x_2$, $x_3$, $x_4$) of each silica content (n = 4), using equations 2.7 and 2.8. This value was then plotted against pore diameter to give an indication of the pore volume distribution within the scaffolds.

Diameter was converted to radius ($r$):

$$r = d / 2$$

[Eq 2.9]

From this value of pore diameter, the volume ($V$) each individual pore was calculated using the equation for a sphere:

$$V = 4/3\ \pi\ r^3$$

[Eq 2.10]

The total volume ($V_T$) occupied by each pore within the scaffold was then calculated:

$$V_T = V \times \mathrm{X}$$

[Eq 2.11]

The pore volumes were added together to give the scaffold pore volume ($\Sigma V_T$), and this value was then used to calculate the % volume contribution of the pores within each scaffold:

$$\%\ \text{volume contribution} = (V_T\ /\ \Sigma V_T) \times 100$$

[Eq 2.12]

The pore volume contribution data for a single representative scaffold containing 0% silica at each depressurisation rate is presented in an abbreviated form in table 2.6.

**Table 2.6: Representative data relating to pore volume contribution in scaffolds containing 0% silica obtained through gas foaming at $160^0$C and 160 bar with vent rates as stated (n=1)**

| | Depressurisation rate (L/min) | Pore diameter range (mm) | Diameter of main contributor to pore volume (mm) | % contribution |
|---|---|---|---|---|
| **‘SLOW’** | **0.2** | **0.09 – 1.5** | **1.4** | **11.4** |
| | **0.5** | **0.07 – 1.3** | **1.3** | **40.9** |
| ↓ | **1.0** | **0.07 – 1.2** | **1.1** | **26.9** |
| | **1.5** | **0.09 – 1.1** | **1.1** | **8.3** |
| **‘FAST’** | **2.25** | **0.04 – 0.9** | **0.9** | **22.8** |

It can be seen from the pore diameter ranges obtained that the pores at the lower end of the diameter range are not overly affected by depressurisation rates of between 0.2 and 1.5 L/min, but decrease dramatically for 2.25 L/min, whereas pore diameters at the higher end of the obtained range decreased steadily with each increase in depressurisation rate, as does the value of the single biggest contributor too total pore volume.

Previous experiments using supercritical fluids (Barry *et al*, 2006) report some control of pore diameter by increasing the depressurisation rate of the vessel. The results that they obtained showed that with a high rate of depressurisation, gas bubble nucleation was rapid and there were a large number of nucleation sites. The rate of pore development was fast, therefore diffusion of gas from the polymer matrix into the bubble would have been negligible and the resulting structure had a uniform pore size distribution. However, with a slow rate of depressurisation (and therefore nucleation), the pores nucleated first would be significantly larger than others nucleated later than them due to greater diffusion of gas from the surrounding matrix into the growing bubble and the resulting structure therefore had a much wider pore size distribution. In other experiments utilising $P_{DL}LA$ foamed in supercritical $CO_2$ at 35$^{o}$C and 240 bar scaffolds with pores 0.05 mm diameter after fast depressurisation (no rate given, but timed over 12 minutes), and scaffolds containing pores of 0.5 mm after slow depressurisation (again, no rate given but timed over 60 minutes) (Quirk *et al*, 2004).

These literature findings are consistent with the results obtained in this depressurisation rate experiment through visual assessment (table 2.5) geometrical measurements (figure 2.5 and table 2.6) and microCT analysis (figures 2.6 and table 2.6); with a slow depressurisation rate (0.2 L/min, over a time period of ~60 minutes) massive expansion occurred that overfilled the moulds by two-fold and much smaller pores could be seen alongside more giant ones. In comparison, a faster depressurisation rate (2.25 L/min, over a time period of ~6 minutes) generated pores that were much more uniform in size. This reduction in porosity could in part be due to the massive expansion and formation of giant pores that took place during the slow depressurisation process which in turn influenced the geometrical measurements used to calculate scaffold porosity, notably height.

By use of microCT at this stage of the experiment it was possible to demonstrate that in addition to the effect seen on the macroporous scale the depressurisation rate also influenced the scaffolds on the microporous scale, affecting the pore size distribution of the material, and this is evidenced through comparison of slow and fast depressurisation rates in table 2.6; This in agreement with the findings of Barry *et al*, 2006 but adds to the data by the addition of 3D measurements.

## 2.5.5 Pore nucleation studies - the effect of silica

### 2.5.5.1 Porosity

For scaffolds made from solvent-cast PLA and PLA-silica films the porosity as calculated from geometrical measurements increased from 48.8% (± 4.2%) in scaffolds containing 0% silica to 96.1% (± 0.2%) in scaffolds containing 33.3% silica and the results are significant for all silica loadings (table 2.7) (one-way ANOVA, n=8, with level of significance $p = 0.05$).

**Table 2.7: The influence of silica upon the overall porosity of PLA scaffolds produced through SCF foaming in $CO_2$ at 160°C and 160 bar (the error given is the standard deviation from the mean; n=8).**

| Silica content (by % weight of PLA) | Silica content (by % of final scaffold mass) | Porosity (%) |
|---|---|---|
| 0 | 0.0 | 48.8 ± 4.2 |
| 2 | 2.0 | 73.9 ± 2.9 |
| 5 | 4.8 | 82.6 ± 1.8 |
| 10 | 9.1 | 89.5 ± 0.8 |
| 20 | 16.7 | 92.9 ± 0.6 |
| 30 | 23.1 | 94.4 ± 0.4 |
| 40 | 28.6 | 95.3 ± 0.2 |
| 50 | 33.3 | 96.1 ± 0.2 |

### 2.5.5.2. Pore size

MicroCT analysis of structure separation measurements and calculations of pore volume contribution (calculated as shown in section 2.4.1.2) are shown in figure 2.6. The structure of the scaffolds containing PLA alone (0% silica) contained pores with a range of diameters (0.088 – 0.924 mm) with no single largest contributor to percentage volume (black diamonds). By adding 2wt% silica to the polymer, the pore size distribution was considerably narrowed and the majority of pore volume was contributed by pores of diameter 0.088 – 0.616 mm (black triangles), with the largest contributor to pore volume being pores of 0.342 mm in diameter (16.5%). Addition of 16.7% silica to the PLA (black squares) narrowed the pore size distribution even further to 0.088 – 0.44 mm with pores of 0.176 mm diameter contributing most to the overall pore volume (31.3%). A silica content of 33.3% resulted in a further narrowing in pore size distribution to between 0.044 – 0.342 mm, with the largest proportion of pore volume contributed by pores of diameter approximately 0.176 mm (black rectangles).

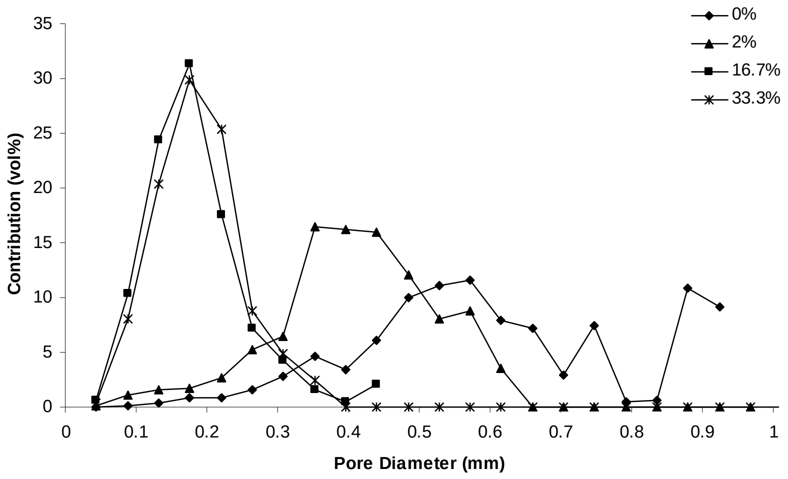

**Figure 2.6: Pore size distributions of foamed PLA-silica scaffolds derived from microCT.**

The author proposes that the inclusion of silica in the PLA films prior to the SCF foaming process provided further surfaces and minute bubbles within the polymer – artifacts from the solvent casting process - upon which nucleation could occur, and that this further accelarated the heterogeneous nucleation of  bubbles when the pressure and temperature became favourable, in accordance with the findings of previous work (Ramesh *et al.* 1994 a and b). Pore size may also have been influenced by the addition of increasing amounts of silica which would have resulted in a proportionate decrease in the viscosity of the polylactide, resulting in less growth (Matthieu, 2006).

As mentioned in section 2.4.1.1, there are many models of nucleation and bubble formation but not all of them can be applied to polymer systems; some models of heterogeneous nucleation represent the effect of solid surfaces by a reduction in the Gibbs free energy (Shafi *et al.* 1997), but factors such as the inherent porosity in the preprocessed material and residual solvents that may plasticise and alter the surface free energy of the polymer can also have an impact upon the extent of each nucleation type, the differing rates of which inversely affect the average pore size formed (Mooney, 1996).

There have been studies on diffusion-driven bubble growth in Newtonian, power-law, and visco-elastic melts (Ramesh *et al.* 1991). Bubbles are assumed to remain spherical during growth, and bubble-bubble interaction is accounted for, to a limited extent, by a cell model where the influence of other bubbles is represented by a finite shell of polymer melt.

Ramesh *et al.* (1994 a and b) also proposed a model based on three key assumptions:

1) Each particle produces one bubble from its largest microvoid. Bubbles created by smaller voids, if any, are absorbed by the largest one during the onset of bubble growth.

2) The size of the nucleated bubbles scales with the size of the particle.

3) There is a minimum size for the bubble to be viable; larger ones grow further while smaller ones disappear.

These assumptions have been adapted to predict bubble growth in polymer melts proposing that instead of the larger bubble growing and absorbing smaller bubbles, under typical processing conditions the viscosity of the melt would contribute much more resistance to bubble growth than the interfacial tension, minimising the dependence of nucleation on the critical nucleus size. The relevance of this to the pore nucleation study is that by increasing the silica content, the viscosity of the polymer was increased, thus contributing to a reduction in achievable pore size.

It has been long established in the boiling literature that crevices and depressions on solid surfaces (microvoids) contain microbubbles that serve as nuclei during boiling. Similarly, in polymer foaming experiments it has been observed that dissolved gas tends to aggregate on the surface of the nucleating agents, and that each aggregation will in turn become a nucleation site during foaming or degassing (Tatibouet *et al*, 2002).

Some researchers have shown that the total number of bubbles to be several times more than that of the solid particles (Kieken, 2001) and proposed that bubbles were continuously produced by a particle, from one or several active cavities; the rate of production depended upon the detachment time of the bubble, which in turn was dependent on the gas diffusivity and cavity geometry; the rate of nucleation was shown to slow down with time as the bubble growth gradually used up the dissolved gas in the melt. A similar idea has been used in other models to account for simultaneous nucleation and growth (Shafi *et al*, 1997).

The relevance of these pieces of work to the pore nucleation study is that by incorporating more particles of silica, the number of nucleation sites was also increased proportionally, however the volume of available gas for bubble growth was constant; hence more pores would be formed but their growth would be limited by the amount of $CO_2$ available.

Examination of scaffold sections using scanning electron microscopy enabled visual assessment of the effect that the addition of silica had on both the diameter of the pores and also the number of pores (porosity) present within the scaffold (figure 2.7 A and B).

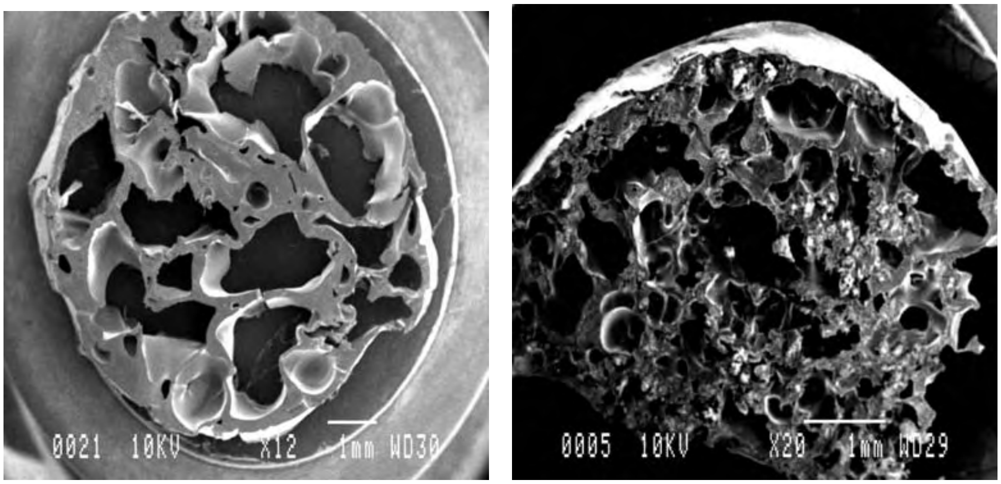

**Figure 2.7: A) PLA x 12 magnification; B) PLA with 33.3% silica x 20 magnification.**

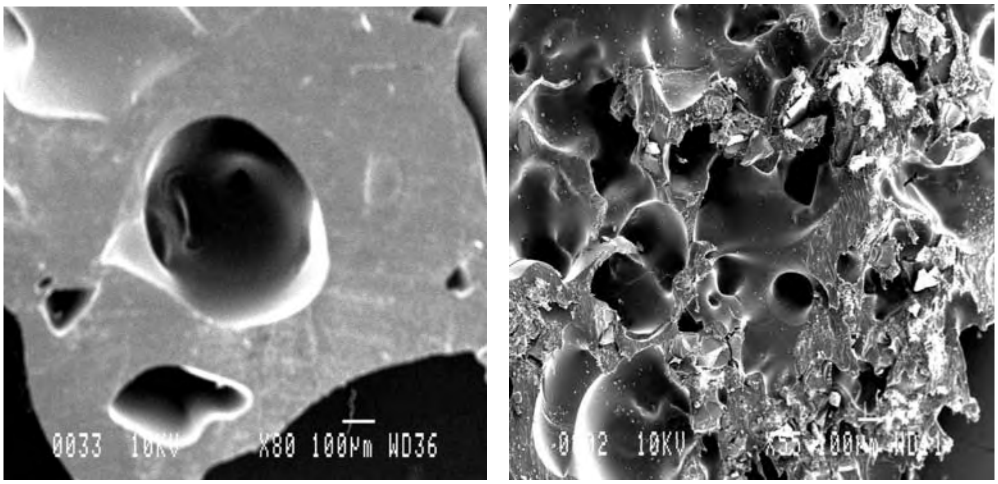

**Figure 2.7: C) PLA x 80 magnification and D) PLA with 33.3% silica x 65 magnification.**

In figure 2.7 A, the largest pore in the field of view measures approximately 0.25 mm in diameter whilst the largest pore in the field of view in figure 2.7 B measures approximately 0.05 mm (by comparison of the scale bars, taking magnification into account); at higher magnifications as can be seen clearly in figure 2.7 C and D, the pores are not only smaller with the addition of silica, the distance between them (effectively the pore wall thickness) is also much smaller – the significance of this will be discussed further in Chapter 3.

In order to visually assess pore size distribution, models of the scaffolds were built using microCT data (figure 2.8); the diameters of the pores present on the reconstructions were consistent with those obtained in the scanning electron micrographs, showing that the data obtained from the microCT scans was as reliable as SEM in assessing pore size and structure.

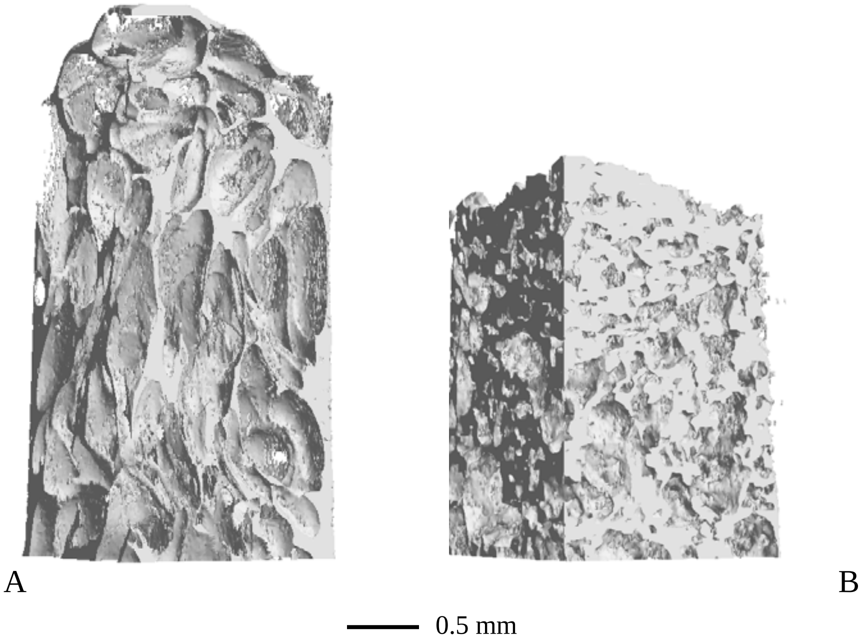

**Figure 2.8: X-ray computed microtomography was used to characterise the pore structure of each scaffold. A PLA; B PLA with 33.3% silica**

## 2.6 Conclusion

The scope of the preceding experimental work was to produce scaffolds suitable for tissue engineering applications through the supercritical fluid gas foaming approach using the polymer Polylactide (PLA) with the inclusion of the mineral silica in order to address two of the issues typical of such scaffolds, namely low connectivity between pores, and the presence of an outer ‘skin’.

It was found that varying the rate at which depressurisation occurred allowed some control over the total porosity of unmodified PLA scaffolds, with slow depressurisation of the vessel at 0.2 L/min resulting in scaffolds with an average porosity of 83.4 ± 1.2%, while a more rapid rate of depressurisation (2.25 L/min) resulted in the formation of PLA scaffolds with an average porosity of 64.6 ± 2.0%, obtained from geometrical measurements.

Inclusion of silica at a rate of depressurisation of 2.25 L/min resulted in scaffolds that were between 48.8% ± 4.2% porous (0% silica) and 96.1% ± 0.2% porous (33.3% silica) obtained from geometrical measurements. Analysis of these scaffolds by microCT showed the pores to be in the diameter range of 0.088-0.924 mm in the absence of silica, and 0.044 – 0.342 mm with the inclusion of 33.3% silica demonstrating that silica was beneficial in control of both pore size and overall scaffold porosity.

Visual assessment of the scaffolds by SEM and microCT modelling confirmed this reduction in pore size and also revealed the absence of the outer skin which is known to often blight gas foamed scaffolds.

# Chapter 3 Scaffold microstructure and connectivity

## 3.1 Section introduction

Foamed polymer scaffolds contain ‘void volumes’ of empty space, distributed within the solid mass. The total sum of these void volumes is the porosity of the scaffold, and it strongly determines important physical properties such as durability, mechanical strength and degradation kinetics. The knowledge of pore structure is therefore an important step in characterising the scaffold and predicting its behaviour under different environmental conditions.

Pores can be either open or closed; an open pore is a cavity or channel that connects with the surface of the scaffold and is therefore accessible to fluids or gases. Open pores can be further divided in dead - end and open end (interconnected) pores.

A closed pore is inside the material and is therefore completely isolated from the external surface, and does not allow the access of external fluids in neither liquid nor gaseous phase. Closed pores influence parameters like density, mechanical and thermal properties (Sing *et al*, 1985).

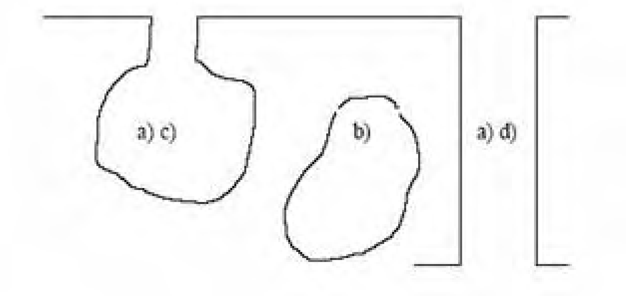

**Figure 3.1: Different pore types: a) open; b) closed; c) dead – ended; d) open – ended.**

Table 3.1 gives definitions of some commonly used definitions associated with pores and porosity.

**Table 3.1: Definitions of some common terms used to describe pores and porosity. BSI, British Standards Institute; ASTM, American Society for Testing and Materials**

| **Term** | **Definition** |
|---|---|
| Macropore | A pore of diameter > 50 nm |
| Mesopore | A pore of diameter from ~ 2 nm to 50 nm |
| Micropore | A pore of diameter < 2 nm |
| Closed Pore | A cavity with no access to an external surface |
| Open Pore | A cavity or channel with access to an external surface |
| Pore volume | The volume of open pores unless otherwise stated |
| Porosity | a) The ratio of open pores and voids to the envelope volume (BSI)<br>b) The ratio, expressed as a percentage, of the total volume of voids of a given porous medium to the total volume of the porous medium (ASTM) |

Pore structures within scaffolds are usually analysed by scanning electron microscopy (SEM) (Jenkins *et al*, 2006; Matthieu *et al*, 2005; Howdle *et al*, 2001; Hile *et al*, 1999) or by mercury intrusion porosimetry (MIP) (Rigby *et a*l, 2002; Lu *et al*, 2000). MIP can provide reliable information about the pore size and pore volume distribution, the bulk density and the specific surface area for porous solids regardless of their nature and shape. Gas sorption porosimetry and gas pyconometry can also be used, but the applicable pore size ranges of each technique are different; gas sorption and pyconometry is useful for pores in the diameter range 0.00035 – 0.5 mm, and mercury intrusion for pores 0.3 - 300 mm. For the range of pore sizes of the scaffolds in this study, mercury intrusion porosimetry was deemed to be the more appropriate method to use.

However, the results obtained by both SEM and MIP can be misleading for several reasons. SEM micrographs are images of a sectioned or freeze fractured (broken) surface, therefore a true representation of the 3D shape and connectivity cannot be made; MIP only gives an indirect indication of the connectivity of the pore network through the degree of narrowing of the pore spaces and requires the use of a mathematical model in order to interpret the experimental data, and there are other problems which are discussed further in section 3.1.1.

The external macrostructure of the scaffold surface can be visualised by use of light microscopy but is of limited use to assess microstructure due to poor light penetration to the interior of the scaffold and therefore poor image quality; like SEM, analysis of sections of the scaffold would represent an image of a fractured or sectioned surface. More recently, X-ray computed microtomography (section 2.3.4) has been used as an alternative to these destructive 2D methods.

Relative density may also be calculated using the Archimedes method, although is limited in accuracy by the presence of closed pores, which water cannot penetrate.

SEM and microCT were introduced in chapter 2, so the technicalities will not be discussed any further here; a brief overview of MIP and the Archimedes method follow.

### 3.1.1 Mercury intrusion porosimetry

Mercury intrusion porosimetry collects information about porosity by applying various levels of pressure to a sample immersed in mercury. The pressure required to intrude the mercury into the samples pores is inversely proportional to their size (explained in section 3.4.1).

However, the level of detail and the accuracy of the characterisation of the sample obtained by this method all depend upon the degree of sophistication of the model used to interpret the data obtained. Larger pores may be concealed (shielded) by surrounding smaller pores, and pores where the opening (neck) of the pore is smaller than the body of the pore (as in figure 3.1 a) may not be detected.

As the result of the percolation process, the shape of a mercury intrusion curve is sensitive to the connectivity and spatial arrangement of the individual pores within the sample space; the invasive percolation process and the pressure to which the samples are exposed may cause very thin pore walls to collapse, causing a spike in mercury intrusion volume to be superimposed on the intrusion curve.

#### 3.1.1.1 Theory

Mercury is a non-wetting liquid, that it is to say it resists contact with any other material or surface that it comes into contact with. Consider a drop of mercury resting on a solid surface as shown in Figure 3.2. The underside of the drop is in contact with the solid surface. The remainder of the surface of the drop is in contact with some other fluid above, typically either its own vapour or air. This creates liquid-solid, liquid-vapour, and solid-vapour interfaces as well as a liquid - solid - vapour boundary. There is tension in each interface; the liquid - vapour and solid - vapour interfacial tensions also are referred to as surface tensions. The angle of contact of the liquid-vapor surface to the solid-vapor surface at a point on the liquid - solid – vapour interface characterises the interfacial tension present between the solid, liquid, and vapour.

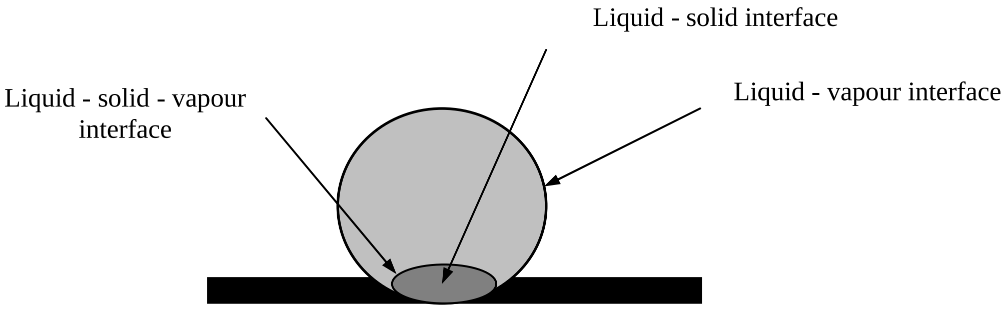

**Figure 3.2: The interfaces present on a drop of liquid resting on a solid surface.**

Figure 3.3 shows five liquids of different surface tensions resting on the same surface material. Different surface energies cause the liquids to assume different contact angles relative to the solid surface. A liquid with lower surface tension (lower surface energy) than the solid surface will spread out on the surface forming a contact angle less than $90^o$; this is referred to as wetting. If the surface energy of the liquid exceeds that of the solid, the liquid will form a bead and the angle of contact will be between $90^o$ and $180^o$; this is a non-wetting liquid relative to the surface.

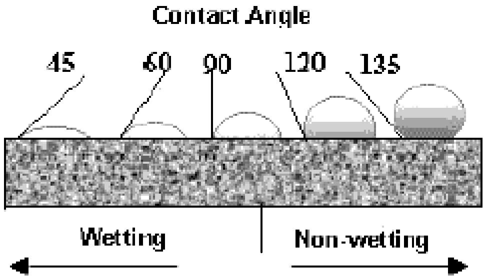

**Figure 3.3: Angles of contact for wetting and non – wetting liquids.**

(adapted from Micromeritics information)

Interfacial tensions also cause liquids to exhibit capillarity. If one end of a capillary tube is forced to penetrate the vapour - liquid surface from the vapor side, a wetting liquid spontaneously enters the capillary and rises to a level above the external liquid - vapour interface. A non-wetting liquid resists entering the capillary and remains at a level below the external liquid - vapour level. In other words, a non-wetting liquid must be forced to enter a capillary. Inside the capillary and along the line describing the vapour - liquid - solid boundary, the liquid - solid interface assumes an angle that results in equilibrium between cohesive and adhesive forces. In summary, there are three physical parameters needed to describe the intrusion of a liquid into a capillary: a) the interfacial tension (surface tension) of the liquid - vapour interface, b) the contact angle of the liquid on the capillary surface, and c) the geometry of the line of contact at the solid - liquid - vapour boundary.

Washburn in 1921 derived an equation describing the equilibrium of the internal and external forces on the liquid - solid - vapour system in terms of these three parameters. It states that the pressure required to force a non-wetting liquid to enter a capillary of circular cross-section is inversely proportional to the diameter of the capillary and directly proportional to the surface tension of the liquid and the angle of contact with the solid surface (see section 3.4.1). This physical principal was incorporated into an intrusion-based, pore-measuring instrument by Ritter & Drake in 1945. Mercury is used almost exclusively as the liquid of choice for intrusion porosimetry because it is non-wetting to most solid materials.

### 3.1.2 The Archimedes method

Archimedes principle states that any floating object displaces its own weight of water; in terms of forces this can be interpreted such that any object whether fully or partially immersed in a fluid, is acted upon by a force equal to the weight of the fluid displaced by the object. For a sunken object, the volume of displaced fluid is the volume of the object, and for an object floating on the liquid surface, the weight of the displaced liquid is the weight of the object. By recording the weight of an object before and during submersion in water its true density can be calculated (section 3.4.2).

## *3.2 Materials*

Scaffolds containing a range of silica contents were manufactured as described in Chapter 2 (section 2.3).

## *3.3 Methods*

### 3.3.1 MIP

The equipment used was a Micromeritics Autopore IV. The sample was loaded into the penetrometer which was then sealed and placed into a low pressure port to evacuate air and moisture and which was then backfilled with mercury. The pressure within the penetrometer was slowly increased from 0 to 15 psia. The penetrometer was then moved to a high pressure port where the pressure was steadily increased to 33,000 psia The results initially collected were the capacitance readings from the interior and exterior surfaces of the penetrometer at each pressure point, the difference in which was indicative of the volume of mercury infiltrated into the sample. This raw data was converted into a pore size distribution by a computer program using the Washburn equation and the parallel pore bundle model (section 3.4.1). The maximum intrusion pressure was 33,000 psia, the contact angle of mercury on the sample was 130$^o$, the equilibration time between pressure increases was 10 seconds

### 3.3.2 Light microscopy

A Leica DM750 light microscope connected to a Canon Ixus digital camera was used to obtain images from the upper and lower surfaces of the scaffolds. Initial assessment of the scaffold surface was made using a 10 x objective lens combined with a 10x eyepiece lens. The maximum obtainable magnification was 40x objective lens. Images were captured using Powershot software.

### 3.3.3 Archimedes method

The dry sample mass was recorded using a 4 d.p. balance (Fisher Scientific, UK). The wet sample mass was then recorded by using a suspended balance with the sample submerged in water. Prior to recording the wet mass of the scaffold, the internal pore structure was completely saturated with water in order to gain a better measurement of the true density of the scaffolds. This was accomplished by inserting the scaffold into a 5 ml disposable syringe barrel (after first removing the syringe plunger), filling the syringe with enough water to cover the scaffold (~2.5 ml) and then sealing the inlet of the syringe with Blu-tack. The syringe contents were compressed to the point at which air bubbles were seen to escape from the scaffold surface. The pressure on the syringe was released and the process repeated until no further air bubbles were seen to escape, at which point the scaffold was taken to be fully saturated with water. The scaffold was removed from the syringe (in the reverse process of insertion) and the wet mass recorded. The true and apparent density for the scaffold was then calculated (section 3.4.2). Three scaffolds were measured for each of 0, 4.8, 9.1, 16.7, 23.1 and 33.3% w/w silica contents.

## 3.3.4 MicroCT

The scaffold scanning and image acquisition data procedure has been described in section 2.4.1. The scaffolds used were the same as previously scanned, but the data obtained relating to scaffold to pore ratio within the scaffold (% object volume), pore diameter (structure separation), pore wall thickness (structure thickness) and pore connectivity (fragmentation index) has been interpreted in more depth.

Fragmentation index is an inverse index of connectivity which was developed and defined by Hahn *et al* in 1992, and it is best considered as a relative index for comparing different scanned objects as its absolute value does not have much meaning. It was calculated by the CTan program using an algorithm relating the surface area and volume of the thresholded object before and after image dilation, which in effect either increases or decreases the boundary of the object of interest by one pixel:

$$FrI = (S_1 - S_2 / V_1 - V_2) \qquad \text{[Eq 3.1]}$$

Where $S_1$ is the object surface area before dilation, $S_2$ is the object surface area after dilation, $V_1$ is the object volume before dilation and $V_2$ is the object volume after dilation.

Where structural connectedness resulted in an enclosed space (pore), image dilation contracted the surface resulting in a lower fragmentation index; a prevalence of enclosed spaces could even result in a negative fragmentation index. By contrast the surface of an open end would have expanded on image dilation resulting in a higher fragmentation index.

## *3.4 Calculations*

### 3.4.1 MIP

Washburn's equation, upon which data reduction is based, assumes that the pore (or capillary) is cylindrical and the opening is circular in cross-section. As has been stated, the net force tends to resist entry of the mercury into the pore and this force is applied along the line of contact of the mercury, solid, and (mercury) vapour. The line of contact has a length of $2\pi r$ and the component of force pushing the mercury out of the pore acts in the direction $\cos\theta$ where $\theta$ is the liquid - solid contact angle.

Therefore, the force needed to expel the mercury from the pore ($F_E$) is:

$$F_E = 2\pi r \, \gamma \cos\theta$$

[Eq 3.2]

Where $\gamma$ is the surface tension.

An external pressure on the mercury is required to force its entry into the pore. The relationship between force (F) and pressure (P) is:

$$P = F/\text{area}$$

[Eq 3.3]

Therefore the force required to intrude mercury into the pore ($F_I$) is:

$$F_I = \pi r^2 P$$

[Eq 3.4]

Where $\pi r^2$ is the cross-sectional area of the pore opening.

Balancing the intrusion and extrusion forces results in the Washburn equation:

$$-2\pi r\,\gamma\cos\theta = \pi r^2 P$$

[Eq 3.5]

Or, in terms of diameter D:

$$-\pi D\gamma\cos\theta = (\pi D^2 P) / 4$$

[Eq 3.6]

The relationship between applied pressure and the minimum size pore into which mercury will be forced to enter is:

$$D = -4\gamma\cos\theta / P$$

[Eq 3.7]

For a given liquid-solid system, the numerator is constant, providing the simple relationship expressing that the size of the pore into which mercury will intrude is inversely proportional to the applied pressure. In other words, mercury under external pressure P can resist entry into pores smaller than D, but cannot resist entry into pores of sizes larger than D. So, for any pressure, it can be determined which pore sizes have been invaded with mercury and which sizes have not.

### 3.4.2 Archimedes method

For each of the scaffolds analysed, the apparent density ($\rho_a$) was calculated as follows:

$$\text{Density of object} / \text{density of fluid} = \text{weight} / (\text{weight- apparent immersed weight})$$

[Eq 3.8]

The theoretical density ($\rho_t$) was calculated in a similar manner as described in section 2.3.3.1 (Eq 2.4), by taking into account the individual densities of silica ($\rho = 2.6$ g / cm$^3$)

and the literature value for the density of PLA ($\rho = 1.24$ g / cm$^3$) within each scaffold formulation.

The fraction density of the scaffold was then calculated using the newly calculated apparent and theoretical densities:

$$\text{Fraction density} = \rho_a / \rho_t$$

[Eq 3.9]

And directly from fraction density, fraction porosity:

$$\text{Fraction porosity} = 1 - \text{Fraction density}$$

[Eq 3.10]

An index of fraction interconnected porosity (F.I.P) was then calculated, taking into account the microCT estimation of scaffold volume porosity (object volume of pores):

$$\text{F.I.P} = \text{fraction porosity} / \text{object volume of pores}$$

[Eq 3.11]

## *3.5 Results and discussion*

### 3.5.1 Light microscopy

Figure 3.4 demonstrates how the size and morphology of the pores present on the surface of the scaffolds was influenced by the presence of silica. The pores of the scaffold containing 0% silica (A and C) can be seen to be much larger (~ 1 mm diameter) and much more widely and randomly spaced. In contrast, the pores of the scaffold containing 33.3% silica (B and D) can be seen to be much smaller (~ 0.3 mm diameter) and had a tendency to be arranged in clusters. Analysis of the images obtained through microCT indicated that some of the clusters of pores coincided with the position of silica particles (figure 3.9).

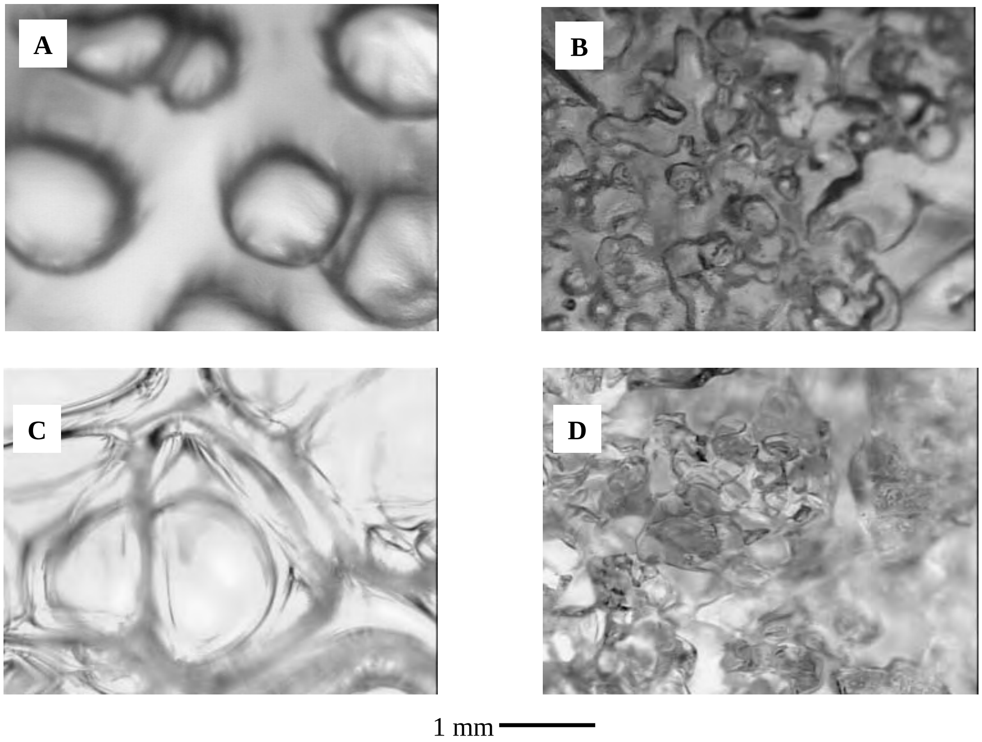

**Figure 3.4: Light micrographs of PLA-silica scaffolds x 400 magnification.**
(A: 0% silica base; B: 33.3% silica base; C: 0% silica top; D: 33.3% silica top)

### 3.5.2 MIP

As the pressure in the port was increased, mercury was forced into the largest pores first followed by those of decreasing diameter. Figure 3.5 shows the pore size distribution obtained from the Washburn equation/parallel pore model for a PLA scaffold containing 0% silica (A) and 33.3% silica (B).

In A it can be seen that the largest volume of mercury is intruded at the points correlating to pore diameters of 0.01 μm and between 1 – 100 μm; In B it can be seen that largest volume of mercury is intruded at the points correlating to pore diameters of 0.01 μm and between 5 – 100 μm. The respective porosities of these scaffolds as indicated by MIP were 36% (0% silica), and 47% (33.3% silica). The pore size that contributed most by volume was 96 μm in the scaffold containing 0% silica and 189 μm in the scaffold containing 33.3% silica.

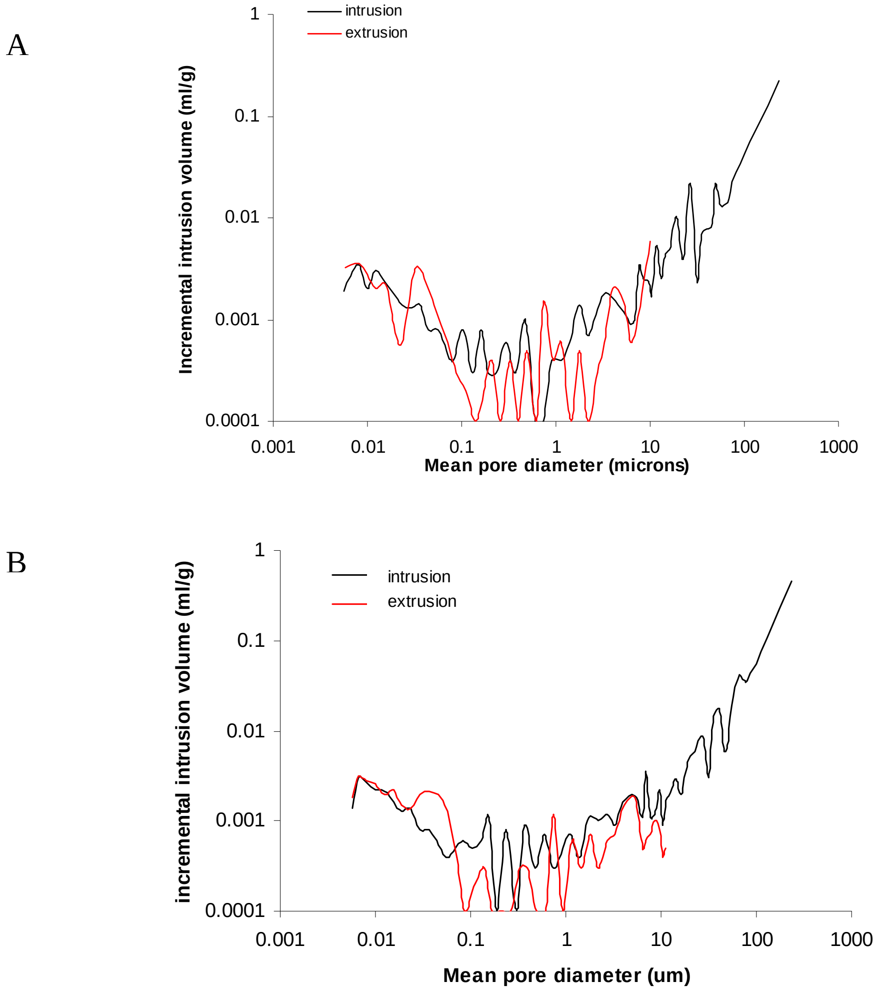

**Figure 3.5: Analysis of pore size distribution by MIP.**

(A: PLA scaffold containing 0% silica; B: PLA scaffold containing 33.3% silica)

MIP is known to overestimate the volume of the smallest pores, due to the presence of closed pores and interconnected pores that shift the pore size volume distribution towards smaller pores (Dees and Polderman 1981). The diameter of the pore opening into the surface of the sample determines when mercury is intruded into the sample. Large pores with a small opening are thus filled at high pressures, and detected as smaller pores than they actually are.

During measurement, high pressures to force mercury into small pores may compress the sample. This effect can be especially marked in samples containing closed pores and is observed as a too large volume of small or medium sized pores (Palmer and Rowe 1974; Dees and Polderman 1981).

It has long been noted that for many materials the intrusion curve at near maximum pressure takes a sudden upward swing. In some cases, this apparent uptake of mercury by the sample is caused by mercury filling the void in the sample cup produced by the collapse or compression of the sample material. If the extrusion curve follows the intrusion curve in this region, the material is demonstrating restitution or elasticity and returning to its original shape or volume, as demonstrated by the graph in figure 3.6A.

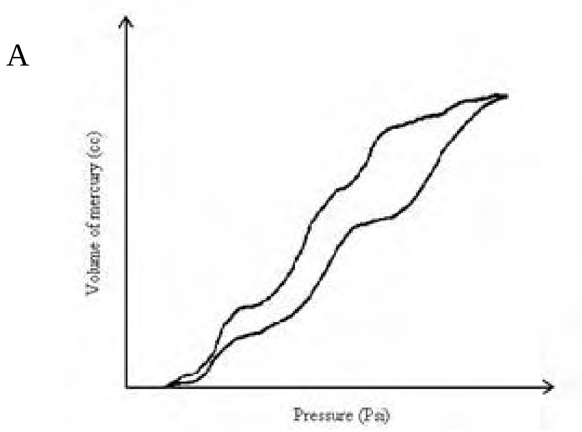

**Figure 3.6A: An ideal intrusion – extrusion curve illustrating restitution (Micropore instruction manual).**

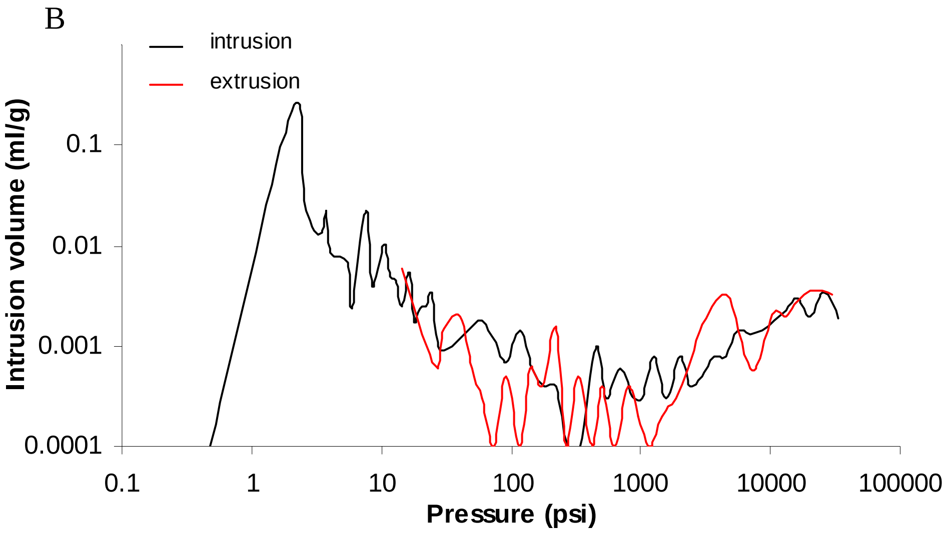

**Figure 3.6B: The intrusion-extrusion curve exhibited by scaffolds containing both 0% and 33.3% silica.**

If the extrusion curve fails to retrace the intrusion curve (as can be seen in figure 3.6 B) the material has been permanently deformed. A pore filled with mercury applies pressure to the pore walls essentially with the same pressure as applied by the bulk mercury surrounding the sample. Therefore, structural collapse is not likely to have been caused by collapse of the open pore structure, but is more likely due to pores that are inaccessible to the mercury. However, there is no way mercury porosimetry can determine whether the upward swing in the intrusion curve was caused by material compression, pore collapse, filling of open pores, or a combination of these occurring at the same time. This will also affect the reported porosity values.

The values obtained for porosity are for open (interconnected) pores and will be compared with the values obtained from microCT (3.5.4).

### 3.5.3 Archimedes method

The theoretical density of the scaffolds is the density they would be if their structure was entirely solid i.e. it contained no pores. The Archimedes method will give an indication of the extent of these pores if they are open to the surface or to each other. Because the scaffolds contain a large number of pores the degree to which these pores connect with each other can be estimated by the apparent density of the scaffolds (table 3.2). This assumption has been made in the knowledge that a fully connected pore network would allow water penetration through the entire scaffold structure and would give an apparent density close to that of the theoretical density. A more disconnected pore network would not allow such extensive water penetration and the apparent density would be considerably less than the theoretical density. It can be seen from table 3.2 that although the values for apparent density increase steadily from 0.61 (0% silica) to 0.76 (33.3% silica) indicating a more connected pore network, for all of the silica contents they do not even closely approach the values for theoretical density and this was thought to be due to the increased proportion of silica content as silica is considerably more dense than PLA (with densities of 2.6 g cm$^{-3}$ and 1.24 g cm$^{-3}$ respectively).

**Table 3.2: Trends in apparent density and theoretical density with silica content (n=3)**

| % silica addition | Apparent density | Theoretical density |
|---|---|---|
| 0 | 0.61 ± 0.09 | 0.81 |
| 9.1 | 0.69 ± 0.03 | 4.17 |
| 16.7 | 0.74 ± 0.04 | 6.98 |
| 23.1 | 0.71 ± 0.04 | 9.36 |

|  |  |  |
|---|---|---|
| 33.3 | 0.76 ± 0.04 | 13.15 |

The fraction of the apparent to theoretical density gave the relative density of the scaffold and since density and porosity are effectively the opposite entities of each other the assumption made was that whatever was not dense (solid) would be pores and so the values for relative porosity were also obtained (figure 3.7).

The value for relative porosity obtained by the Archimedes method was then compared to the value obtained for total porosity - connected and disconnected pores – from microCT measurements. The ratio of the two values was taken to be an indicator of the fraction of connected pore volume throughout the whole scaffold structure, and this was termed the interconnected porosity (table 3.3). Increasing silica loading resulted in a considerable increase in pore structure interconnectivity from a factor of 0.48 with 0% silica increasing up to 1.00 when the scaffold was loaded with 33.3% silica.

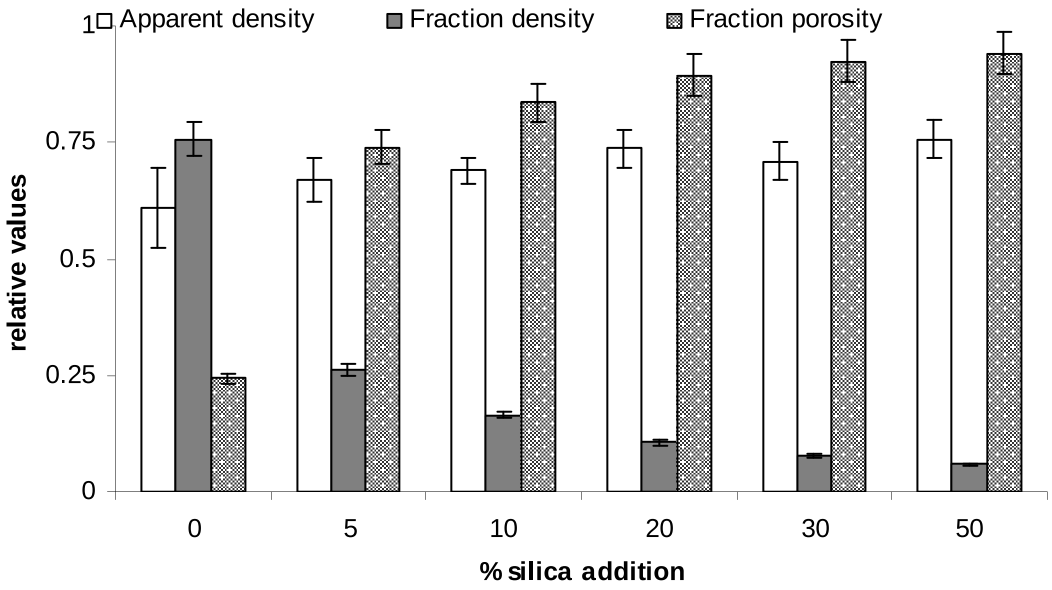

**Figure 3.7: Relationship between apparent density, fraction density and fraction porosity with variation in silica content. Error bars for apparent density are standard deviation from the mean (n=3), other error bars are values ± 5%.**

**Table 3.3: Fraction interconnected porosity (F.I.P) as a function of the porosity measurements obtained by the Archimedes method and microCT**

| % silica addition | Porosity (Archimedes) | Porosity (MicroCT) | F.I.P |
|---|---|---|---|

| | | | |
|---|---|---|---|
| 0 | 0.25 | 0.52 | 0.42 |
| 4.8 | 0.27 | 0.54 | 0.49 |
| 9.1 | 0.33 | 0.55 | 0.55 |
| 16.7 | 0.41 | 0.55 | 0.76 |
| 23.2 | 0.54 | 0.60 | 0.98 |
| 33.3 | 0.60 | 0.60 | 1.11 |

Figure 3.8 demonstrates the approximately linear relationship between the fraction interconnected porosity and silica content.

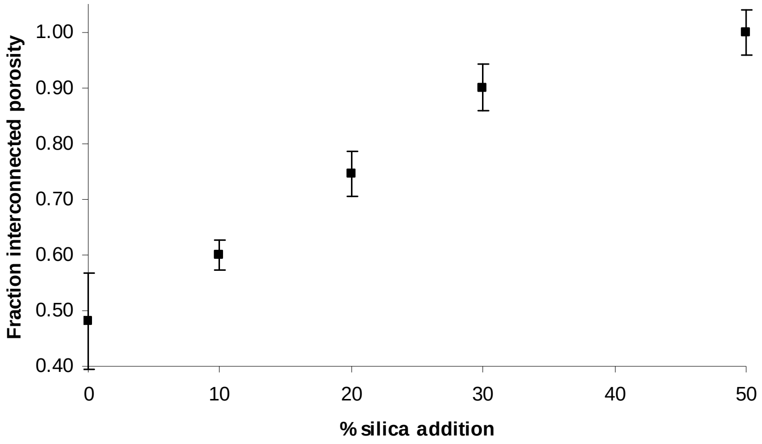

**Figure 3.8: Relationship between the fraction interconnected porosity and silica content of PLA scaffolds impregnated with silica (error bars indicate standard deviation from the mean; n=3).**

### 3.5.4 MicroCT

All of the scaffolds were porous as demonstrated by representative cross sections (mid-height) and longitudinal sections (mid-width) through scaffolds containing 0, 10 and 50

% silica (figure 3.9). The incorporation of silica particles had a significant influence on the morphology of the resulting pores. Silica (dark grey/black spots) was seen to be distributed throughout the polymer (lighter grey background). The influence of silica content on the extent of foaming of the polymer can be best seen in longitudinal section and is evidenced by a reduction in scaffold height. The average height of the scaffolds containing 0 % silica was 9.1 mm ± 0.3 mm, 9.1 % w/w silica was 7.8 mm ± 0.03 mm and for 50 % silica it was 6.7 mm ± 0.2 mm (n=4).

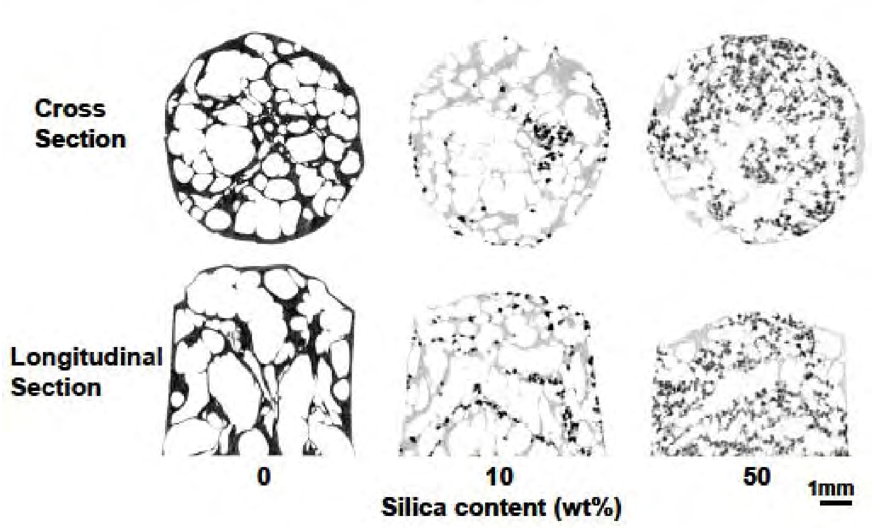

**Figure 3.9: Cross-section and longitudinal section images through PLA-silica scaffolds obtained through microCT X ray attenuation images.**

Figure 3.10 shows the effect of the thresholding process on the appearance of the solid scaffold structure and pores. From these images, it can be seen that the incorporation of silica particles into the polymer had a significant influence on the complexity of the resulting pore network.

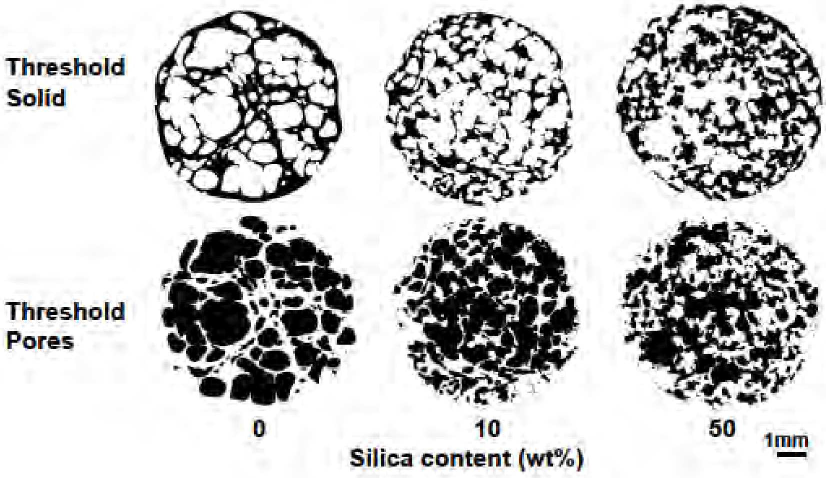

**Figure 3.10: The same cross-section image as in Figure 3.8, thresholded for solid and pores.**

Further analyses were undertaken to quantify the influence of silica addition on the porosity (the relative volume occupied by solid and pores), pore size distribution and the interconnectivity of the pore network. Despite the aforementioned reduction in height with silica loading level, total scaffold porosity was largely independent of silica loading (Figure 3.11). Scaffolds foamed in the absence of silica were 59 ± 1% porous. The porosity of scaffolds formulated with silica was within the range of 49 ± 2% (2% silica) to 54 ± 2% (33.3% silica) with the most porous scaffold being that containing 9.1% silica (60% ± 2%). These results suggest that had the height of the scaffolds remained constant (instead of decreasing) the porosity of the scaffolds would actually have increased in line with the increase in silica loading.

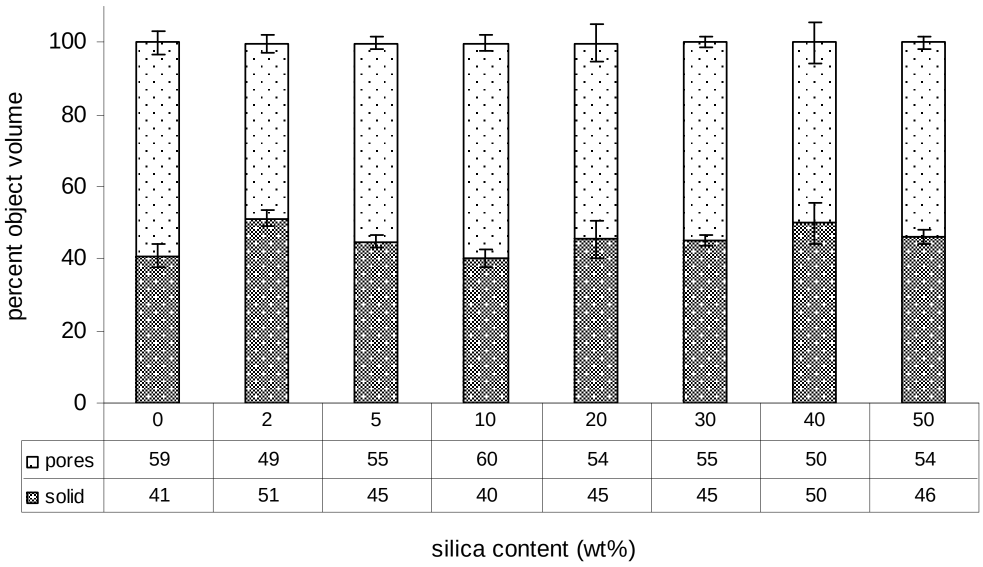

| | 0 | 2 | 5 | 10 | 20 | 30 | 40 | 50 |
|---|---|---|---|---|---|---|---|---|
| □ pores | 59 | 49 | 55 | 60 | 54 | 55 | 50 | 54 |
| ▩ solid | 41 | 51 | 45 | 40 | 45 | 45 | 50 | 46 |

**Figure 3.11: Relative volumes within the PLA-silica scaffolds occupied by solid and pores obtained from microCT calculations of percent object volume.**

These values are dramatically different to the values of porosity obtained by MIP: 36% (0% silica), and 47% (33.3% silica). This could be due to the fact that although the pores in the scaffolds are in the range detectable by MIP (0.3 – 360 mm), the pore volume (on which the calculation of porosity is based) is measured by the volume of mercury that is intruded into each pore. As discussed previously (3.5.2), if the pore neck is narrower than the pore body, it is possible that the pore volume as well as pore diameter would have been underestimated.

Further characterisation of the scaffolds sought to elucidate the nature of the porosity and attempt to quantify interconnectivity of the pore structure using microCT and physical measurements. The microCT derived determination of interconnectivity for the scaffolds was based on assessment of the fragmentation index. For scaffolds containing between 2 and 33.3% silica, the fragmentation index tended to decrease with increasing silica content, indicating an increase in the interconnectivity of the pore structure (Figure 3.12). Interestingly, in the absence of silica, the fragmentation index was 3.8, which suggested that the structure was at least as interconnected as those containing silica. From examination of Figures 3.9, 3.10 and 3.11, this was clearly not the case. Indeed, the nature of the analysis of this parameter is such that it is unable to distinguish between the apparent volume of 'interconnected' space between large, isolated pores, and the real interconnectivity afforded by pathways of smaller ones.

The interconnectivity of a foamed structure is dependent upon the wall thickness of the foamed material. From the microCT data the inter–pore separation (wall thickness) was measured and it was shown to correlate with the interconnectivity of the pore structure through an inverse relationship (Figure 3.13).

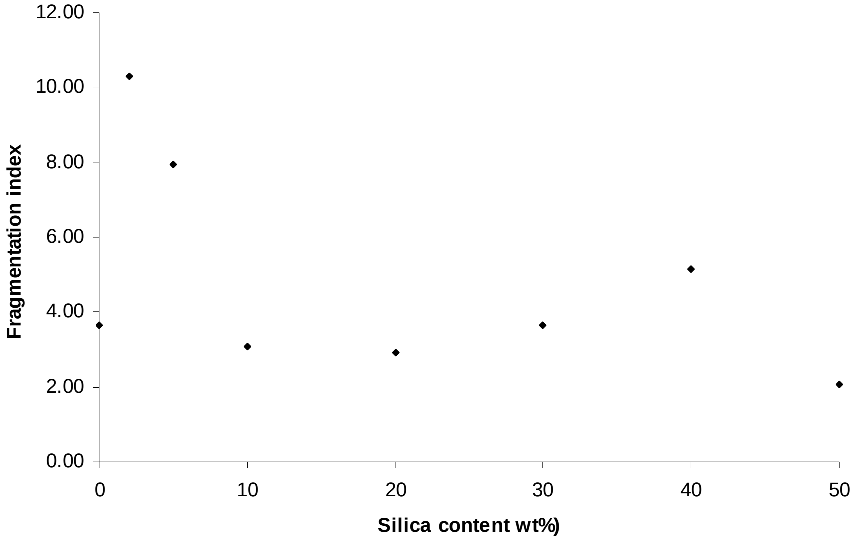

**Figure 3.12: Comparison of pore connectivity in SCF foamed scaffolds.**

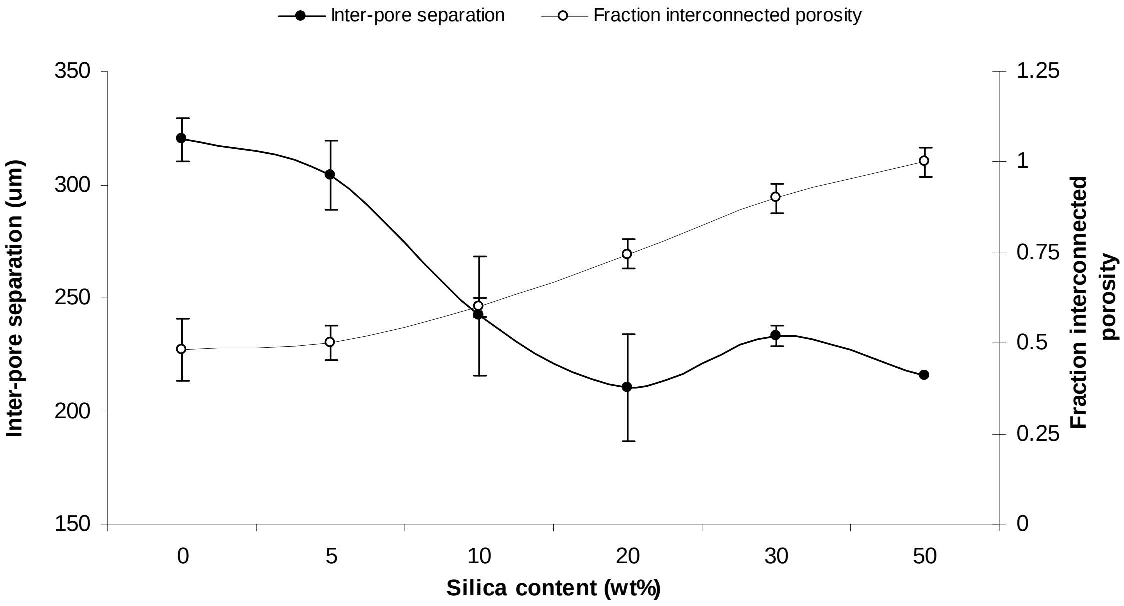

**Figure 3.13: Relationship between pore wall thickness and fraction interconnected porosity (Error bars indicate standard deviation from the mean, n=4)**

## 3.6 Conclusion

The 3D structure of scaffolds is known to play an important role in the success of bone tissue growth, and although advances have been made scaffolds still need to be optimised for better integration with host tissue post operatively and for complete substitution by native tissue in the longer term. The more accurately pore connectivity can be measured the more informative it becomes for the scaffold producers and microCT goes some way to addressing the shortfalls of some conventional methods.

Mercury intrusion porosity is an established method for assessing pore size and porosity but cannot be used on porous structures such as the polymer scaffolds created in the course of this study due to the collapse of delicate pore walls under the pressures needed to intrude mercury into the very smallest pores. These high pressures lead to a perceived porosity of open pores of 35.8% in scaffolds containing 0% silica and 46.8% in scaffolds containing 33.3% silica compared to values of 25% and 60% respectively as obtained by the Archimedes method, (open pores) and 59% and 54% respectively by microCT (open and closed pores). Measurements pertaining to pore wall thickness and connectivity were also obtained from microCT, and the two parameters were found to have an inverse relationship.

MicroCT has already been extensively used to characterise bone micro-architecture at different sites (Hildebrand and Ruegsegger, 1997), in different age groups and with damage caused by osteoporosis (Hildebrand *et al*, 1999), and many of the algorithms can be directly applied to the field of tissue engineering in order to facilitate scaffold design and optimisation. Unlike mercury intrusion porosimetry it is a non-destructive method and in addition it provides quantitative analysis of both closed and open pores. However, more quantitative data needs to be collected to optimise the algorithms that calculate the fragmentation index since the nature of the analysis of this parameter is such that it is unable to distinguish between the apparent volume of ‘interconnected’ space between large, isolated pores, and the real interconnectivity afforded by pathways of smaller ones.

MicroCT has the potential to be used to directly observe the biological system both pre and post implant, giving important information to the surgeon/researcher about its success or failure. It has already been used to assess the integrity of scaffold materials with a high degree of accuracy in a number of non-quantitative studies (Spowage *et al*, 2006; Cancedda *et al*, 2007), and quantified data exists for pore sizes in B-tricalcium phosphate scaffolds (Bashoor-Zadeh *et al*, 2009), for pore size and characterisation in SCF foamed $P_{DL}A$ scaffolds, (Patel *et al*, 2009), for porosity and interconnectivity in SCF foamed polymer scaffolds (Silva *et al*, 2006) and for pore interconnectivity of bioactive glasses (Atwood *et al*, 2004). Quantitative data is highly important as it is a prerequisite for a tissue-engineered scaffold to achieve regulatory approval.

# Chapter 4 Physical and mechanical properties

## 4.1 Introduction

The physical properties of a semi-crystalline polymer are characterised by its glass transition temperature ($T_g$), melt temperature ($T_m$), enthalpy of fusion ($\Delta H_f$) and by how crystalline it is (the degree of crystallinity, $X_c$). All of these values can be ascertained by differential scanning calorimetry (DSC) (Yokohara and Yamaguchi, 2008; Qiu *et al*, 2007; Pyda *et al*, 2004). The degree of crystallinity can also be established by use of polarised light microscopy (Chao *et al*, 2008).

The mechanical properties of a polymer such as its toughness, stiffness, tolerance of stress and strain (from which the Youngs' modulus can be calculated) and its yield point (point of failure or breakage) are important in determining its suitability for a particular application, and are generally measured by use of a universal testing machine.

Each of these properties will now be discussed individually.

### 4.1.1 Physical properties: $T_g$

The $T_g$ of a polymer describes the point at which its appearance alters from being 'glass-like' to being 'rubbery' (figure 4.1), the value of which is determined by the structure of the polymer chain, the available free energy and also the 'free volume of rotation' – the amount of rotation permissible about the backbone of the chain. It is also associated with the amount of disorder in the chemical structure. The $T_g$ is a property specific to the amorphous regions of the polymer chain.

The $T_g$ of a polymer is a function of its relative molecular mass since in short chain molecules, the ends of the chain move at a very different rate to the rest of the backbone which lowers the $T_g$, whilst in longer chain molecules (relative molecular molar mass $>10^5$) $T_g$ becomes almost constant. The $T_g$ is a second order thermodynamic process which is kinetically controlled and therefore its precise value will depend upon the rate or frequency of the applied stimulus (eg, the heating and cooling rates in thermal analysis) (Campbell, 2000; polymer characterisation, 2nd ed, CRC press, FL, USA).

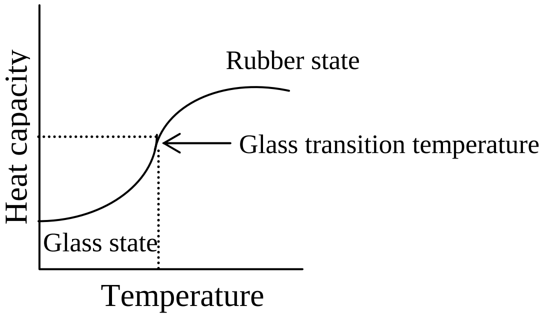

**Figure 4.1: Graphical illustration of the relationship between temperature and heat capacity showing the position of the $T_g$.**

### 4.1.2 Physical properties: $T_m$ and Xc

Melting points are indicative of bond strength. At room temperature, the atoms within a solid are in a state of constant vibration; as the temperature is raised the vibrational energy of the atoms increases to a point at which the bonds are broken and the solid melts. Bond strength, atomic arrangement and crystal structure are of equal importance in determining $T_{m.}$ Regular crystal structures tend to have regular atomic arrangement and are therefore said to be crystalline and ‘ordered’; Irregular crystal structures tend to form amorphous ‘disordered’ solids.

Relative molecular mass and amount of disorder influence the $T_m$ and $X_c$, since an increase in relative molecular mass results in an increase in $T_m$ therefore only polymers with ordered crystalline regions will have an observable $T_m$. The melt transition can occur over a broad range of temperatures reflecting a range of crystal sizes and extents of perfection; it is accompanied by a dramatic change in the mechanical properties of the polymer.

### 4.1.3 DSC

DSC is a thermo-analytical method in which the difference in the amount of heat required to increase the temperature of a sample and reference material are measured as a function of temperature, the objective being to maintain both materials at identical temperatures. The basic principle underlying this technique is that when the sample undergoes a physical transformation such as a phase transition more (or less) heat will need to flow to it than the reference to maintain both at the same temperature. For example, as a solid sample melts to a liquid it will require more heat in order to increase its temperature at the same rate as the reference, due to the absorption of heat by the sample as it undergoes the endothermic phase transition from solid to liquid. Likewise, as the sample undergoes an exothermic process (such as crystallisation) less heat is required to raise the sample temperature. By observing the difference in heat flow between the sample and reference it is possible to measure the amount of energy absorbed or released during such transitions. DSC may also be used to observe more subtle phase changes such as the glass transition.

The DSC apparatus used in the experiments that follow was a power compensated DSC. Typically a DSC experiment consists of identical aluminium sample and reference pans (generally an empty sample pan), covered and sealed by an aluminium lid; aluminium is used as the material of construction as it has a high thermal conductivity. The two pans are situated in a heating block and energy is supplied to (or removed from) each pan by independent heating circuits to maintain the system in a ‘thermal null’ state. The heating or cooling scan rate is uniform so that the heat flow difference between the two can be monitored over a set temperature range (figure 4.2).

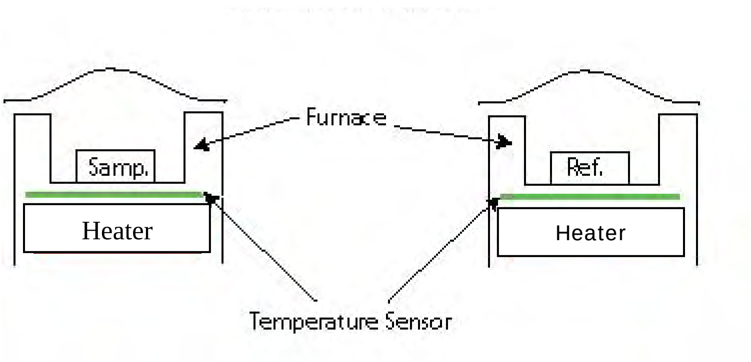

**Figure 4.2: Cross sectional diagram through the heating block of power compensated DSC apparatus (replicated from Perkin-Elmer user guide).**

The difference in the heat flow between the sample and reference pan is then processed resulting in a plot of the differential heat flow between the reference and sample cell as a function of temperature. When there are no thermodynamic physical or chemical processes occurring, the heat flow difference between the sample and reference varies only slightly with temperature, and shows up as a flat or very shallow base line on the plot. However, an exothermic or endothermic process within the sample results in a significant deviation in the difference between the two heat flows. The result is a peak in the DSC curve. Generally, the differential heat flow is calculated by subtracting the sample heat flow from the reference heat flow and therefore exothermic processes will show up as positive peaks (above the baseline) while peaks resulting from endothermic processes are negative (below the baseline).

The result of a DSC experiment is a heating or cooling curve. This curve can be used to calculate enthalpies of transitions, by integrating the peak corresponding to a given transition (glass transition or melt). It can be shown that the enthalpy of transition can be expressed using the following equation:

$$\Delta H = \mathrm{KA}$$

[Eq 4.1]

Where $\Delta H$ is the enthalpy of transition, K is the calorimetric constant, and A is the area under the curve. When applied to a melting peak, the value obtained is the enthalpy of fusion ($\Delta H_\mathrm{f}$), or the enthalpy of the melt ($\Delta H_\mathrm{m}$).

The calorimetric constant will vary instrument to instrument, and can be determined by analysing a well-characterised sample such as tin or zinc with known enthalpies of transition, as a means of calibrating the instrument prior to use.

If there is a clearly defined endotherm peak then the maximum value is used to define the mean melting temperature. However, polymers do not always have discrete melting peaks in the same was as other materials due to the polydisperse nature of their molecular weights, therefore the peak melting temperature can be calculated from the ‘onset’ of melting – the intersection of the baseline before the melt process and the back extrapolation of the melting endotherm to this baseline.

$Xc$ can be calculated from the value of $H_f$ when the value of $\Delta H_f$ for a 100% crystalline sample is known. In practise this value is rarely used as 100% crystalline polymers are difficult to obtain so approximate values are often used (Lu *et al*, 2000).

$$Xc = \frac{Hf}{Hf100}$$

[Eq 4.2]

Or, another way:

$$Xc = \left( \frac{(\Delta Hm - \Delta Hc\ )}{93.1} \right) \times 100$$

[Eq 4.3]

Where $\Delta Hm$ is the enthalpy of melting and $\Delta Hc$ is the enthalpy of crystallisation. In this study $Xc$ was calculated on the average of the $\Delta H_f$ values of each set of four samples of each silica content.

Most commonly, an enthalpy of fusion of 93.1 J/g is used for a 100% crystalline PLLA or PDLA homo-polymer having infinite crystal thickness (Fischer *et al,* 1973). This value of 93.1 J/g is used throughout the literature describing PLLA, but since $T_m$ decreases with decreasing OP, using a constant value for $\Delta Hm$ across all optical compositions may introduce error but there is no systematic way of calculating $\Delta Hm$ for homo-polymers of reduced OP.

It is well known that for PLAs of essentially random optical copolymers of predominantly L-lactide, with small amounts of D- and meso-lactides, the attainable percentage of crystallinity ($Xc$) decreases with decreasing optical purity (OP), and crystallization is essentially nonexistent about when OP < 0.78 (Drumright, 2000).

### 4.1.4 Crystallisation

PLA has been shown to crystallise in one of three forms: α, β, and γ, depending on the composition of the L- and D- forms present. The α form is the most stable, the γ form is the least stable.

It has been observed that a 50:50 mixture of pure PDLA and PLLA will yield an insoluble gel formed by stereocomplexation of the two polymers during crystallisation or polymerisation with a higher crystallinity than PLLA alone. This effect is still observable even at lower levels of 3-9.1% PDLA, and it is thought that the PDLA acts as a nucleating agent increasing the rate of crystallisation (Garlotta, 2001).

In comparison with other crystalline polymers PLA has a low rate of crystallisation and a consequence of this is that mechanical properties such as the Youngs' modulus do not increase in relation to the degree of crystallinity (Drieskens *et al*, 2009).

### 4.1.5 Crystal structure and formation

Historical studies of solution grown crystals analysed by TEM and X-ray diffraction (XRD) concluded that the crystal size was much less than the molecular length, leading to the development of the 'chain folded' crystal theory (Powell and Ingen House, 1991). Subsequent scattering patterns from XRD experiments showed regions of both crystalline and non-crystalline material (ie semi-crystalline), and these results were confirmed by density measurements, leading to the development of the 'fringed micelle' crystal model (Young and Lovell, 1998).

The advent of polarised light microscopy and the study of melt pressed polymer films enabled more of the detail of the crystal structure to be seen (section 4.1.6), and the direction of the birefringence (the rotation of the polarised light) showed that the crystalline regions had radial symmetry with the lamellae arranged tangentially about the molecular axis (figure 4.3 and 4.4). This contradicted the fringed micelle model and hence the spherulite model was developed. Further studies using TEM have shown that under certain crystallisation conditions a bimodal lamellar thickness distribution may be present, the thicker lamellae being formed first interspaced by thinner lamellar which form later; the inter-lamella spaces were found to be filled with amorphous polymer (Bassett, 1981; Principles of polymer morphology, Cambridge University Press, Cambridge).

During isothermal growth, the radii of the spherulites was found to increase linearly with time - the slope of which being the lineal spherulite growth rate - with a smaller number of spherulites being formed at higher temperatures due to a decrease in the nucleation density (ie larger spherulites were formed with increasing crystallization temperature). Spherulites have been shown to contain a stacked lamella morphology, with the long axis of the lamellar crystal running parallel to the spherulite radius.

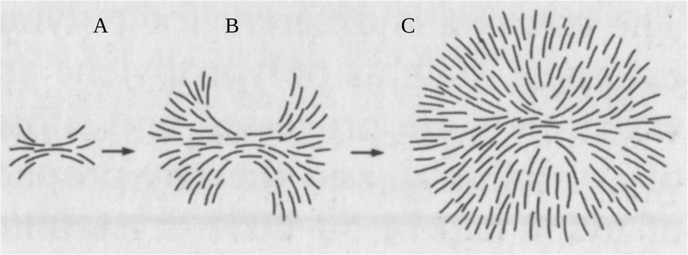

**Figure 4.3: Spherulite formation. A: Crystalline regions of the polymer aggregate. B: Repeated branching develops the intermediate 'wheat sheaf' structure. C: Further branching makes the crystallite spherical in shape, hence the name spherulite.**

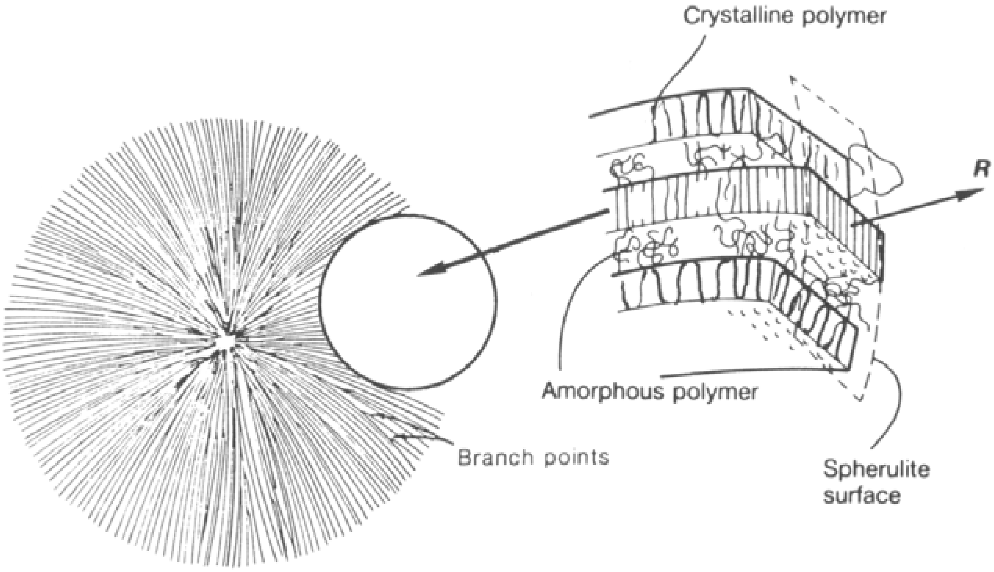

**Figure 4.4: Section through a spherulite showing extensive folding and close packing of the crystalline regions of the polymer chain to form sheets called lamella, with amorphous regions of polymer sandwiched between the lamella. *R* is direction of chain propagation.**

Figures 4.3 and 4.4: Permission applied for; M J Jenkins, UoB web-based learning; Polymers, 1st year, level C PCC

Within the crystal, PLLA has been found to exist as a polymeric helix, with an orthorhombic unit cell of dimensions 1.070 x 0.614 nm and with amorphous polymer residing between the lamellae. The lamellar thickness of PLLA varied with the temperature of crystallization (Tc), crystallization time (tc), optical purity (OP), and molecular weight. PLLA crystals grown at 120, 140, and 160°C had lamellar periodicities (distance from lamella centre to lamella centre) measured at 14–16, 16–18, and 18–22 nm, respectively as determined by AFM (Yuryev *et al*, 2008; Chao *et al*, 2008).

### 4.1.6 Crystallisation kinetics

The crystallisation kinetics of PLA are strongly dependent on the optical copolymer composition and the highest rate of crystallisation can be obtained between 100 and 130°C. The degree of crystallinity, nucleation rate, and spherulite growth rate decrease substantially with decreasing optical purity (OP). The bulk crystallisation half time has been shown to increase by roughly 40% for every 1wt% increase in the meso-lactide (Kolstad, 1996). Two phenomena that contribute independently to the bulk crystallisation rate are nucleation and crystal growth.

Spherulites were shown to be larger in samples crystallised via cooling from the melt than those in samples crystallised via heating from the glassy amorphous state (Pluta and Galeski, 2002). On the lamellar level, the structures were similar for samples prepared by the two methods under similar time and temperature conditions and the thermal properties ($T_m$ and $H_m$) were similar.

### 4.1.7 Polarised light microscopy (hot stage microscopy)

When plane polarised light is transmitted through a thin melt-pressed polymer film the parts of the sample that are birefringent (crystalline areas) will rotate the light differently in comparison to the rest of the sample (amorphous areas). This can also be seen with the difference in orientations of the lamellae as they radiate outwards, resulting in a characteristic ‘Maltese cross’ effect (Figure 4.5).

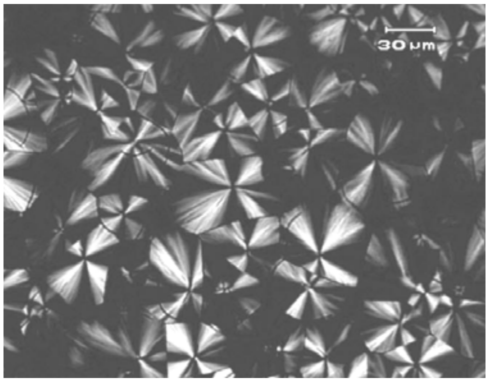

**Figure 4.5: Polarised light micrograph of PLLA spherulites showing the 'Maltese cross' effect caused by birefringence of polarised light (Permission applied for; Chao *et al,* 2008).**

By use of a light dependent resistor (photocell) or digital camera connected to a heating stage and light microscope, images of the passage of polarised light and the depolarisation process can be monitored.

## 4.1.8 Mechanical strength testing

Bond strength, crystal structure and atomic arrangement are equally as important in determining the strength of a material as they are in determining its $T_m$.

A stress-strain curve is the easiest way of visualising the mechanical behaviour of a material because it enables areas of elastic and plastic deformation to be seen. Elastic deformation is reversible, the applied stress is proportional to the strain, and the material is able to return to it original state when the stress is removed. Plastic deformation is irreversible and the stress and strain are not proportional. In crystalline materials, plastic deformation occurs by a number of mechanisms: slip between lamella planes, slip across lamella planes and twisting of the lamella.

Compression testing is used on materials such as composites as this is the type of force the material will be exposed to, and they generate true stress-strain data. The slope of the elastic region of the stress-strain curve gives the value of the Youngs' modulus (also known as the elastic modulus).

## *4.2 Materials and methods*

Prior to all of the following experiments the solvent cast samples were cut as close to size as possible using a scalpel and were heat treated in a hot oven at ~100°C to eliminate the presence of water or residual dichloromethane both of which would have interfered with the obtained results. The 'as received' PLA beads were cut into quarters using very sharp scissors. Foams produced through the SCF process were cut in cross section approximately 1 mm thick at mid-height, and this circular section was then cut into quarters. The masses were recorded using a Sartorius balance accurate to 4 dp with the ideal sample mass for heat transfer in DSC being 4-8 mg (Perkin-Elmer user guidelines).

### 4.2.1 DSC

A Perkin Elmer DSC 1 interfaced to a PC loaded with Pyris series software was used to measure the variation of relative heat flow with temperature. The heating block within the sample chamber was maintained in a constant flow of Argon gas throughout each experiment at a flow rate of 20 ml/minute in order to prevent the formation of water vapour.

#### 4.2.1.1 Sample preparation

Four samples were prepared for each PLA / PLA-silica formulation. The quarter bead was placed in the centre of an aluminium pan using tweezers and the aluminium lid was crimped into place; for the solvent cast PLA and PLA-silica films a small square piece was cut to fit inside the base of the pan without touching the sides. The pan was then placed into the sample cell using hook ended forceps. An empty aluminium pan with crimped lid was placed in the reference cell, the cell covers were gently lowered into place and the heater block cover was locked into place.

#### 4.2.1.2 Non-isothermal crystallisation studies (determination of $T_g$ and $T_m$)

The sample was held at 25 °C to allow the system to equilibrate and was then heated to 180°C at 20°Cmin$^{-1}$ and again held for 1 minute to equilibrate and to remove any thermal history. The sample was then cooled back down to 25 °C at 10°Cmin$^{-1}$. The presence of endotherm peaks corresponding to literature values of $T_g$ and $T_m$ were noted during the heating phase, as was the value of the area under the peak, corresponding to the energy change associated with the transition. In addition, non-isothermal crystallisation would have resulted in an endotherm peak during the cooling phase, so the presence or absence of this was also noted.

#### 4.2.1.3 Isothermal crystallisation studies

During isothermal crystallisation studies, the samples were heated as previously described to 180°C but were then cooled to 110°C ($T_C$) at 80°Cmin$^{-1}$ and held for a given duration ($t_C$) of 60 minutes. The samples were then heated to 180°C at 20°Cmin$^{-1}$, held for 1 minute and then were cooled to 40°C at 20°Cmin$^{-1}$. Peak data was recorded as described previously.

### 4.2.2 Hotstage microscopy and polarised light images

A Linkam THMS 600 hot stage was connected to a PC loaded with LabVIEW 8 Photo Resis and Linksys 32 software, which was also connected to a Linkam TMS 94 temperature controller. Light that passed through the sample was converted to images by a PixeLINK digital camera.

### 4.2.2.1 Sample preparation

A hotplate set to 180°C, a stainless steel cylindrical mould (16 mm diameter and 8 mm in height) and a brass boss slightly under the cylinder diameter were required to melt press the samples. The hotplate was allowed to reach temperature and then the stainless steel mould containing a circular 16mm coverslip was placed onto it using forceps. Very small pieces of as received bead or PLA / PLA-silica film approximating 5mm × 5mm in size were cut from the pieces previously heat treated and was very carefully dropped onto the centre of the coverslip and a second circular 16mm coverslip was placed gently onto the top of the sample. Once the sample was melted, the brass boss was inserted into the mould and was used to apply gentle pressure to the top coverslip, resulting in a sample that was sandwiched between the coverslips and was thin enough for light to pass through. The boss was removed from the mould; the mould was removed from the hotplate using forceps and placed on pieces of tissue to cool enough to be handled. The sample was removed from the mould by inverting and gently tapping the coverslip from the underside of the mould.

### 4.2.2.2 Observation of spherulite formation

Samples were treated in the same manner as in the DSC experiments. Three samples were processed for each film formulation. The PLA film was tested first, as from the literature (discussed in section 4.1.4) it was felt that it would take the longest amount of time to crystallise and could be used as a guideline for the other samples for which the crystallisation time would be considerably less.

The sample was first heated to 180°C and held for 1 minute to remove any thermal history, then cooled to the predetermined crystallisation temperature of 110°C at 50°Cmin$^{-1}$ and held until the sample was completely crystalline – a visual check was carried out every 10 minutes, up to a maximum of 60 minutes. The timing obtained for the first of the three samples was used to inform the interval of image acquisition and duration of crystallisation in the two subsequent samples.

Light intensity was measured both with and without the crossed polarised glass (1л difference) and the digital camera was programmed to record an image every 60 seconds (which was reduced to between 10 and 30 seconds in samples containing silica) as the sample crystallised and the spherulites appeared.

### 4.2.3 Mechanical strength testing

A Zwick-Roell Z030 universal compression testing machine fitted with a 30 kN load cell was used to assess the load applied by the platen versus the distance travelled by the platen up to the point of scaffold failure, and hence to calculate the stress and strain endured by each of the scaffolds and to also determine the Youngs' modulus of each individual scaffold. Five scaffolds of each PLA / PLA-silica formulation were compression tested for each group. The crosshead speed was 0.017 mm $s^{-1}$.

Stress (σ) was calculated from the force applied (F) to the surface area of the sample (A):

$$\sigma = F/A \qquad \text{[Eq 4.4]}$$

Strain (ε) was calculated from the deformation experienced by the sample (*l*) compared to its original height ($l_0$):

$$\varepsilon = l/l_0$$

[Eq 4.5]

The elastic modulus (Youngs' modulus) of the sample (E) was found from the gradient of the slope of the elastic region of the stress-strain curve:

$$\mathrm{E} = \sigma/\varepsilon$$

[Eq 4.6]

## *4.3 Results and discussion*

## 4.3.1 DSC

### 4.3.1.1 Non-isothermal crystallisation studies

**PLA bead**

When heated from 40$^oC$ to 180$^oC$ at 20$^oC$ min $^{-1}$, the PLA beads showed evidence of both a $T_g$ and $T_m$ (figure 4.6). The $T_g$ was recorded as 65.6$^oC$ ± 1.9$^oC$ and the $T_m$ was recorded as 151.7$^oC$ ± 1.4$^oC$ (n=4). There was no evidence of a crystallisation exotherm on cooling.

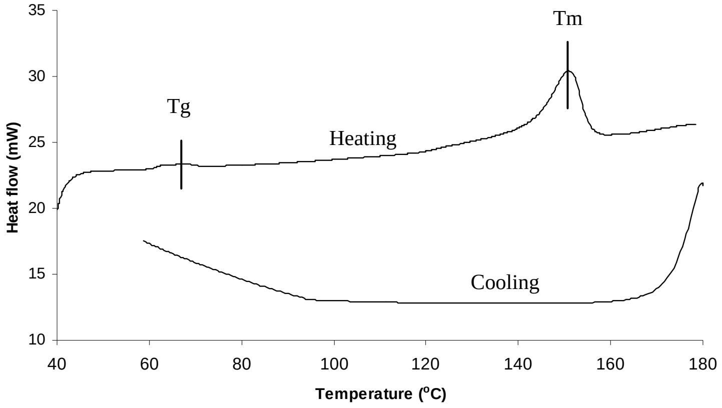

**Figure 4.6: DSC thermogram of typical non-isothermal crystallisation heating and cooling profile obtained from PLA bead.**

### PLA film

When heated from 40$^o$C to 180$^o$C at 20$^o$C min $^{-1}$, the PLA solvent cast films showed evidence of both $T_g$ and $T_m$ (figure 4.7). The $T_g$ was recorded as 63.2$^o$C ± 1.3$^o$C, 2.4 $^o$C lower than the 'as received' PLA bead and the $T_m$ was recorded as 147.8$^o$C ± 1.0$^o$C, 4$^o$C lower than the 'as received' PLA beads. There was no evidence of a crystallisation exotherm on cooling.

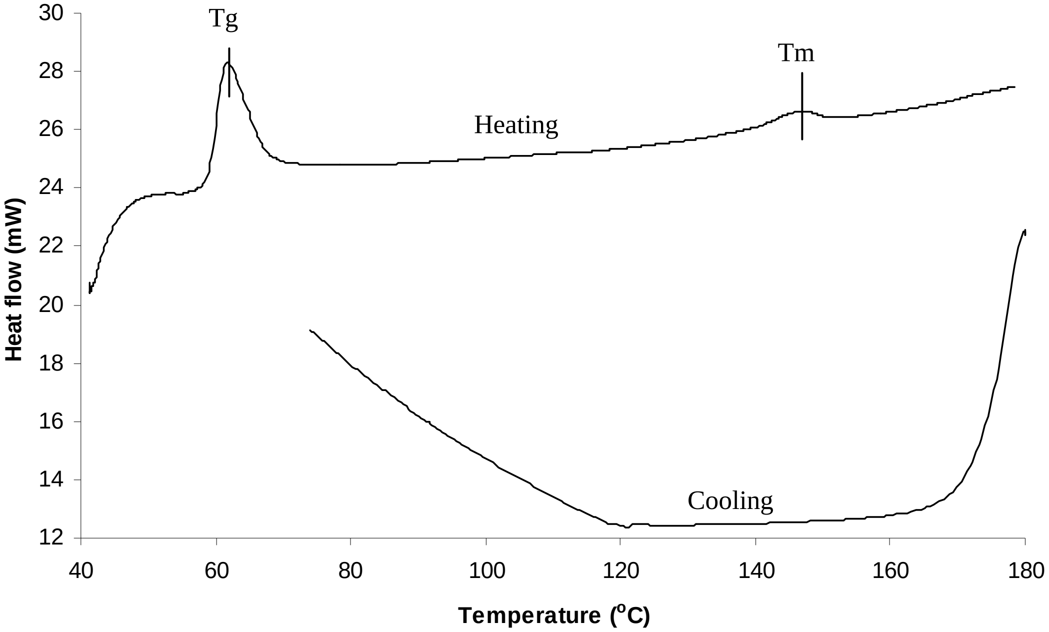

**Figure 4.7: DSC thermogram of typical non-isothermal crystallisation heating and cooling profile obtained from solvent cast PLA film.**

**PLA-silica film**

When heated from 40$^o$C to 180$^o$C at 20$^o$C min $^{-1}$, the PLA-silica solvent cast films also showed evidence of both $T_g$ and $T_m$ (figure 4.8). However, the presence of silica in the samples appeared to contribute to the thermal decomposition of the polymer, making the $T_g$ broader and the slope of the $T_m$ post-endotherm curve uneven with silica concentrations of 9.1% or higher. There was no evidence of a crystallisation exotherm on cooling. Table 4.1 summarises the values of $T_m$ and $T_g$ exhibited by the PLA-silica films and compares them with the values obtained for the 'as received' beads.

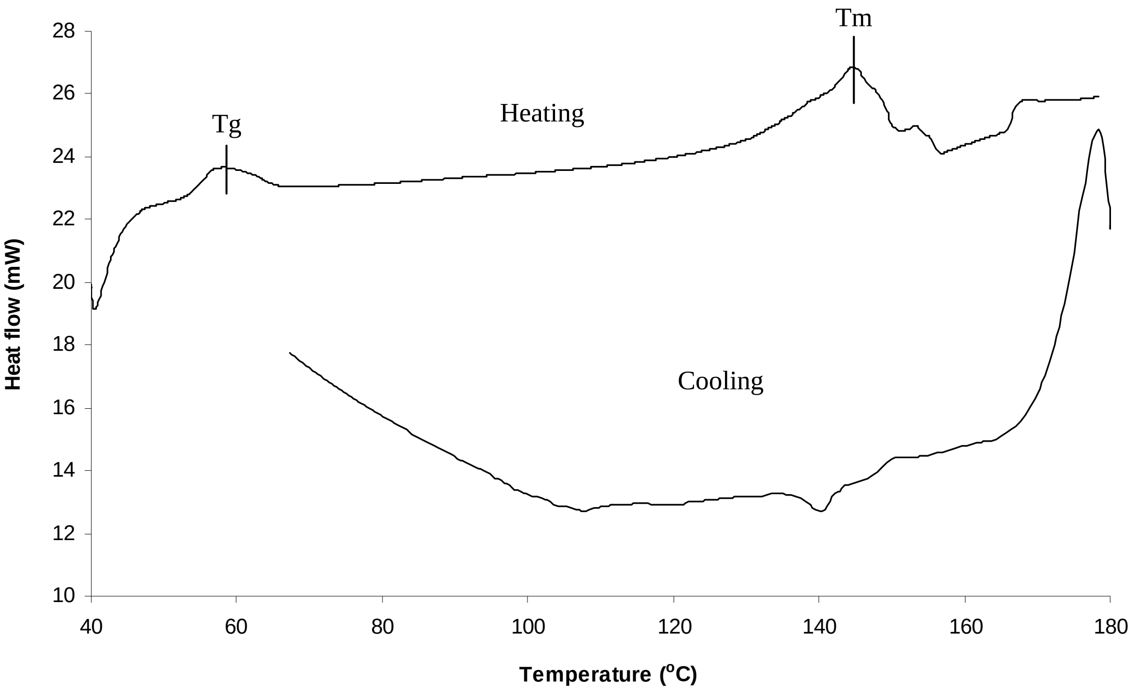

**Figure 4.8: DSC thermogram of typical non-isothermal crystallisation heating and cooling profile obtained from solvent cast PLA-9.1% showing the effect of thermal decomposition on the melt peak.**

**Table 4.1: The values of $T_m$ and $T_g$ of an 'as received' PLA bead and of solvent cast PLA-silica films obtained through DSC non-isothermal crystallisation.**
**Values are presented with the standard deviation from the mean (n=4)**

| Thermal Property (°C) | Sample (wt% silica addition) | | | | |
|---|---|---|---|---|---|
| | PLA Bead | 0 | 9.1 | 23.1 | 33.3 |
| $T_g$ | 65.6 ± 1.9 | 63.3 ± 1.3 | 63.5 ± 2.9 | 66.5 ± 1.3 | 66.6 ± 1.6 |
| $T_m$ | 151.7 ± 1.4 | 147.8 ± 1.1 | 147.5 ± 2.6 | 144.2 ±1.8 | 144.8 ± 2.4 |

From the results presented in table 4.1, it can be seen that the process of solvent casting the PLA beads to make the PLA films reduced the $T_g$ by 2°C, an indication that the crystallinity of the polymer had been reduced. The addition of silica to the solvent cast PLA films resulted in an subsequent increase of the $T_g$ from 63.3°C ± 1.3 °C (0% silica) to 66.6°C ± 1.6 °C (33.3% silica). However, statistical analysis (Mann-Whitney U test, two tails, p=0.05) showed that there was no significant difference between any of the values obtained for the silica containing samples.

With regard to the values of $T_m$ presented in table 4.1, it can be seen that the process of solvent casting the PLA beads to make the PLA films reduced the $T_m$ by 4°C, an indication that the crystallinity of the polymer had been reduced. The addition of silica to the solvent cast PLA films resulted in a decrease of the $T_m$ values throughout, from 147.8 °C ± 1.1 °C (0% silica) to 144.8 °C ± 2.4 °C (33.3% silica).

Statistical analysis showed that there was a significant difference between the value of $T_m$ obtained for the 'as received' bead and the values of $T_m$ obtained for each of the solvent cast silica containing samples. However, among the silica containing samples only the values of $T_m$ for the 23.1% silica sample would appear to be significantly different from the 0% silica sample (Mann-Whitney U test, two tails, p=0.05).

The $T_g$ of a polymer can be affected by the presence of crystalline regions and by the rate of cooling/heating; the rate of heating/cooling was consistent between experiments, therefore the slight increases in $T_g$ with the addition of silica could have been due to the silica nucleating small amounts of crystallisation during the solvent casting process. A similar affect was seen in studies utilising silica nanoparticles (Yan *et al*, 2007), the presence of silica up to 10 wt% was found to increase the crystallinity of PLLA by 8.1% whilst $T_g$ and $T_m$ seemed to be independent of silica loading.

Heating to above the $T_m$ for a sustained period of time has been shown to cause thermal degradation in polymers (Bigg, 1996) which in turn results in shorter chain lengths and lower values of $T_m$. In the experiments carried out in this chapter, an elevated temperature was only used for a short period of time (60 seconds) to erase the thermal history of the polymer, and this may still have caused a small amount of thermal degradation (resulting in the DSC trace seen in figure 4.9), since less energy would have been required to stimulate chain motion and hence melting due to an increased number of chain ends.

One other possible theory is that since the silica had a higher thermal conductivity than the polymer (1.14 $Wm^{-1o}C$ compared to 0.13 $Wm^{-1o}C$ respectively), it was able to conduct heat to the polymer immediately surrounding it, raising the local temperature more quickly than in parts of the sample where silica was absent causing localised melting; these parts of the sample therefore had prolonged exposure to temperatures exceeding the $T_m$ resulting in thermal degradation.

An alternative theory is that the folded chain crystals of the PLA are being reorganised and recrystallised multiple times during the heating process, and that this is the cause of the multiple melt peaks (Bershtein and Egorov, 1994).

The absence of an exotherm in the cooling curves during the non-isothermal crystallisation process (figures 4.7 and 4.8) is not entirely unexpected because literature sources cite PLA as being extremely slow to crystallise from the melt (Drumright, 2000).

Analysis of the $\Delta H_f$ (figure 4.9) showed that the energy associated with the melt transition and hence amount of crystallinity of the sample was significantly higher in the as received PLA bead (28.3 J/g ± 5.3 J/g) than after solvent casting (2.1 J/g ± 0.5 J/g in PLA film). This would suggest that solvent casting removed almost all traces of the crystallinity from the PLA, but the subsequent increase after the addition of silica (from 3 J/g ± 0.6 J/g with 9.1% silica to 6.1 J/g ± 1.4 J/g with 33.3% silica) showed that the crystallinity could be restored. This increase was found to be significantly higher than in the 0% silica sample in samples containing 23.1% and 33.3% silica (Mann-Whitney two tailed U test, P=0.05).

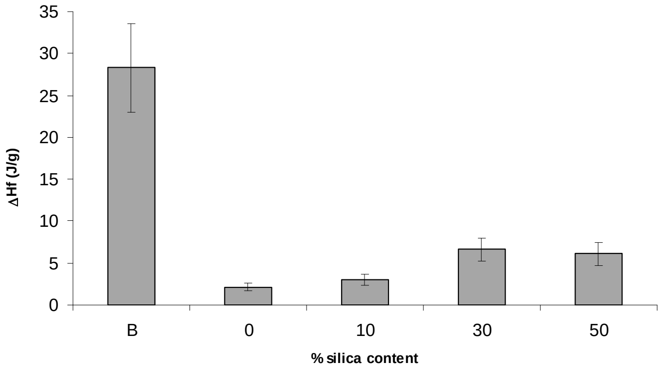

**Figure 4.9: $\Delta H_f$ calculated from the area under curve measurements of DSC thermograms, showing the effect of silica on the energy associated with the melt transition. The effect of silica in samples containing 23.1% silica or higher were significant (Mann-Whitney two tailed U test, P=0.05)**

**(Results are presented showing standard deviation from the mean, n=4)**

The crystallinity of the samples (figure 4.10) exhibited a trend similar to that of the $\Delta H_f$. The crystallinity of the as received PLA bead was found to be 29.1% which was reduced to 2.2% on solvent casting. Addition of 9.1% silica raised the crystallinity to 3.1% which increased to 6.8% with the addition of 23.1% silica and 6.3% with the addition of 33.3% silica; the values for the 23.1 and 33.3%silica samples were significantly higher than for the 0% silica sample (Mann-Whitney two tailed U test, P=0.05).

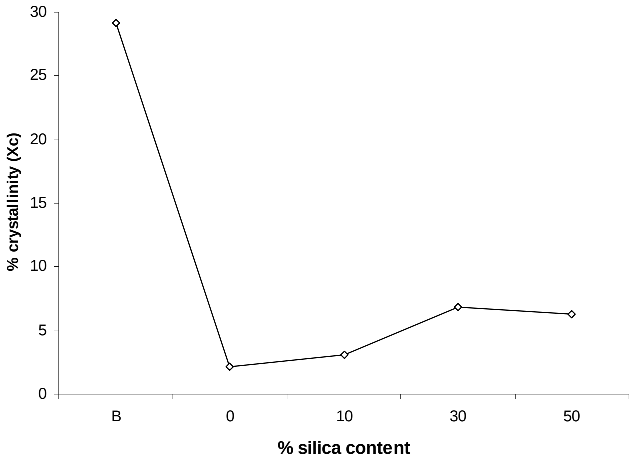

**Figure 4.10: Crystallinity of 'as received' PLA beads compared to solvent cast PLA/PLA-silica films. Values presented are single values obtained from the average of the $\Delta H_f$ of four samples**

## PLA/PLA-silica foam

The data obtained from foamed samples obtained through SCF processing were analysed in the same way as for the films.

It could be seen that there was a notably smaller $T_m$ peak in the PLA foam as compared to the PLA film (figure 4.11), which indicated that that almost all traces of crystallinity had been removed. In fact, the only sample to consistently show a Tm peak with a measurable area under the curve and hence $\Delta H_f$ was the sample containing 23.1% silica; in all other samples, the Tm was transient or absent entirely.

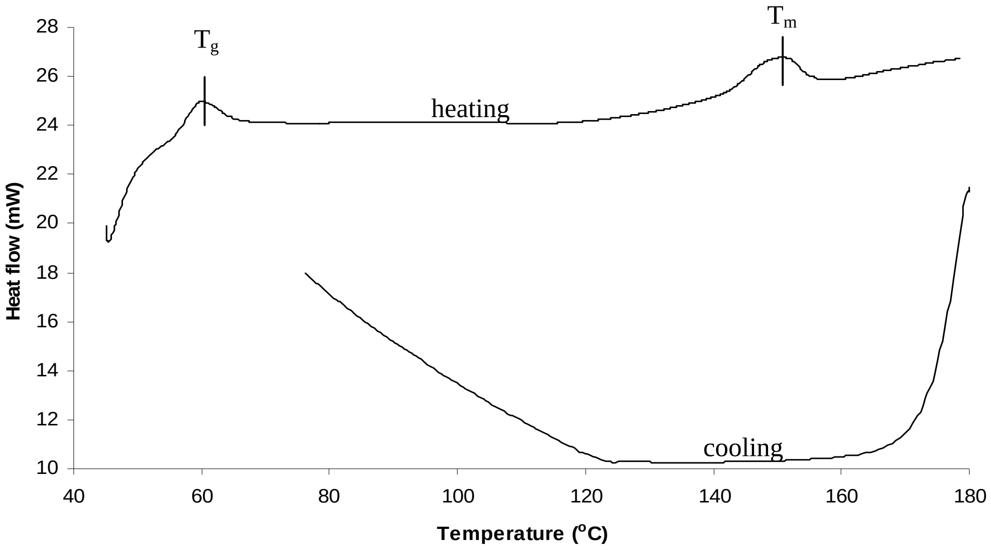

**Figure 4.11: DSC thermogram of a typical heating and cooling profile obtained from SCF processed foams containing PLA with the addition of 23.1% silica.**

The values obtained for the $T_g$ of the SCF foams are given in table 4.2; there was an initial decrease in the PLA bead compared to the PLA film (of 3.1$^o$C) and although the addition of silica produced slight increases in the $T_g$ these were not significant - as was also found with the film data (Mann-Whitney two tailed U test, P=0.05).

**Table 4.2: The values of $T_g$ of SCF processed 'as received' PLA bead and PLA-silica films obtained through DSC non-isothermal crystallisation.**
**Values are presented with the standard deviation from the mean (n=4)**

| Sample (wt% silica addition) | PLA Bead | 0 | 9.1 | 23.1 | 33.3 |
|---|---|---|---|---|---|
| $T_g$ ($^o$C) | 65.9$^o$C ± 2.9 | 62.8 $^o$C ± 1.7 | 64.1 $^o$C ± 0.9 | 63.2 $^o$C ± 2.8 | 63.3 $^o$C ± 2.6 |

Because of the lack of a consistent melt transition, the only data available was obtained from the PLA 23.1% silica sample at 150.5 $^{o}$C producing a $\Delta H_f$ of 6.0 J/g ± 2.8 J/g and % crystallinity of 6.2% ± 0.9%.

### 4.3.1.2 Isothermal crystallisation studies

Data that relates to the melt transition recorded post isothermal crystallisation at 110$^{o}$C for 60 minutes is shown in table 4.3 for both pre- (film) and post- (foam) SCF processed samples.

**Table 4.3: Data obtained through DSC for post isothermal crystallisation of films and foams (the error given is the standard deviation from the mean; n=4)**

| | | **Tm ($^{o}$C)** | **$\Delta$H (J/g)** | **% crystallinity** |
|---|---|---|---|---|
| **film** | **Bead** | 148.9 ± 1.4 | 2.3 ± 0.5 | 2.4 |
| | **0** | 146.3 ± 0.6 | 1.3 ± 0.6 | 1.4 |
| | **9.1** | 147.8 ± 1.8 | 6.4 ± 3.9 | 6.5 |
| | **23.1** | 146.6 ± 1.5 | 8.9 ± 3.5 | 9.2 |
| | **33.3** | 145.6 ± 1.3 | 4.7 ± 2.0 | 4.8 |
| **foam** | **Bead** | 150.1 ± 1.8 | 4.3 ± 0.3 | 4.4 |
| | **0** | 146.7 ± 0.7 | 2.5 ± 0.7 | 2.5 |
| | **9.1** | 147.5 ± 0.5 | 4.8 ± 0.9 | 4.9 |
| | **23.1** | 148.1 ± 0.4 | 9.5 ± 1.0 | 9.7 |
| | **33.3** | 149.9 ± 1.9 | 3.4 ± 1.8 | 3.5 |

Comparing the values obtained for $T_m$, there was found to be no significant difference between the pre- and post-SCF treated samples. The $\Delta H_f$ and % crystallinity were found to be significantly higher in the post-SCF samples than in the pre-SCF samples for the ‘as received’ bead, 0 and 23.1% silica samples (Mann-Whitney two tailed U test, P=0.05).

Figure 4.12 compares the effect of silica on the $T_m$ of the film samples on initial heating (white squares) and on heating after isothermal crystallisation (black squares) and illustrates that although silica appeared to depress $T_m$ on the initial heating, post isothermal crystallisation it had the opposite affect, caused by an increase in degree of crystallinity of the samples. This increase in $T_m$ was significant in the 23.1 and 33.3% silica samples (Mann-Whitney two tailed u test, P=0.05).

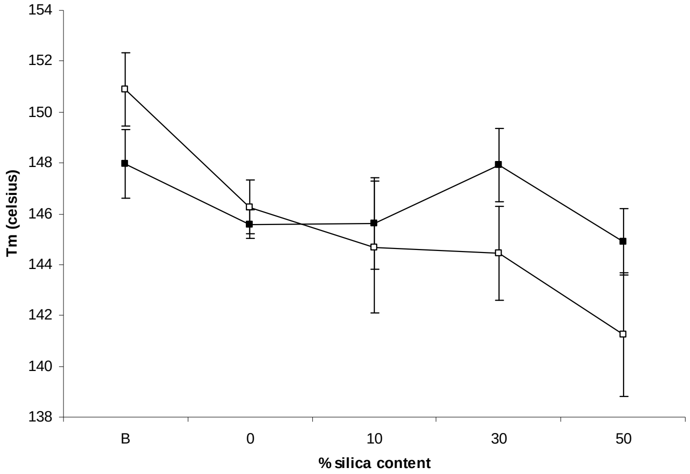

**Figure 4.12: The effect of silica on Tm of silica containing PLA films pre and post isothermal crystallisation. Values are presented with the standard deviation from the mean (n=4 )**

(White squares pre isothermal crystallisation, black squares post isothermal crystallisation)

This observation is borne out by figure 4.13 which shows that there was a decrease in crystallinity on solvent casting, from 29.1% (bead) to 2.2% (0% film), with a subsequent increase following the addition of silica to 6.3% (33.3% silica). Post isothermal crystallisation there was an initial decrease in crystallinity on solvent casting (2.4% to 1.4%) but then increases in the samples containing 9.1% and 23.1% silica (6.5% and 9.2% respectively) and finally decreasing for 33.3% silica (4.8%).

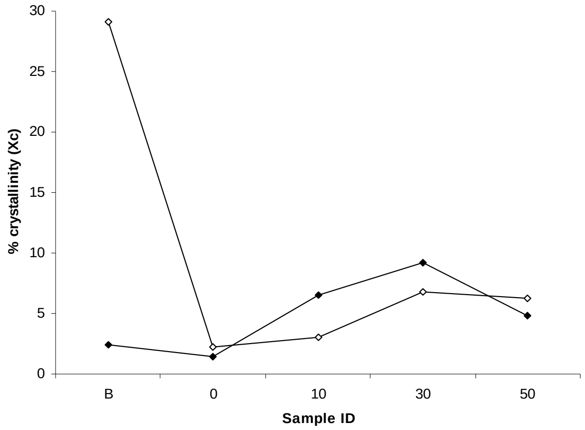

**Figure 4.13: The effect of silica on crystallinity pre and post isothermal crystallisation. Values were calculated from the average of the corresponding ΔH$_f$ values (n=4)**

(White diamonds = pre isothermal crystallisation, black diamonds = post isothermal crystallisation)

Figures 4.14 compares the values of ΔH$_f$ obtained from the area under the melt peak and the crystallinity of the samples after each of the steps of processing – pre and post isothermal crystallisation, and post SCF processing. The trends are similar in crystallinity and ΔH$_f$ since ΔH is used to calculate the value of crystallinity, hence only the one set of data is presented.

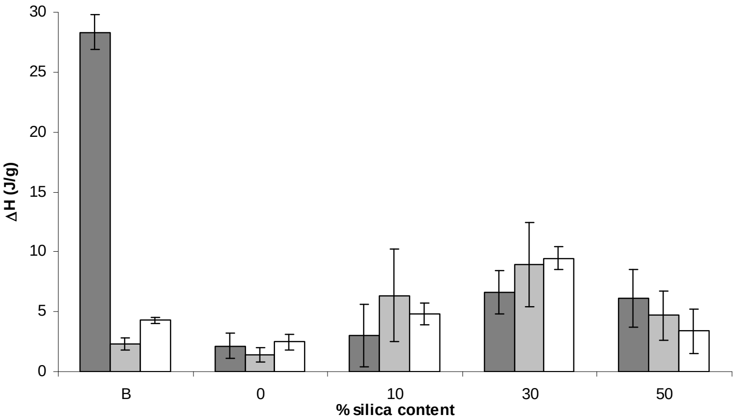

**Figure 4.14: Variation in ΔH$_f$ with degree of heating/processing. Dark grey = solvent cast films pre isothermal crystallisation; Light grey = solvent cast films post isothermal crystallisation; White = SCF processed foams post isothermal crystallisation.**

It can be seen that the $\Delta H_f$ (and therefore crystallinity) is never fully restored, although the addition of silica to the samples up to 23.1% does go someway to addressing this. SCF processing appears to have the greatest effect on samples where silica is absent or in the presence of 23.1% silica and any additional silica content over 23.1% appears to have a detrimental effect on crystallinity and $\Delta H_f$

The fact that the $T_m$ decreases initially would indicate that the films containing silica have less crystal structure or shorter polymer chains (lower $M_w$) as both are known to decrease $T_m$. However, the energy associated with the transition and crystallinity increase, which seems a contradiction; however, as stated earlier the presence of silica had a localised heating effect on the PLA, making the peaks broad and irregular in shape, so the data obtained may not be indicative of the true peak of the melt transition temperature. The results obtained for the foamed samples are more intuitive in that the $T_m$ increases as the energy of the melt and crystallinity increase, which appear to indicate that the presence of silica has a positive effect on the formation of crystalline regions in the foamed structures. There is a decrease in the energy of the melt and crystallinity in the sample containing 33.3% silica for both film and foam, and this would perhaps indicate a counter productive influence of the silica, either in terms of saturation of crystal nucleation (impingement of crystal growth by the other crystals surrounding it) or in terms of nucleation density being too high (not enough room for nuclei to grow to form crystals).

## 4.3.2 Hotstage microscopy

Figure 4.15 documents the growth of spherulites in solvent cast PLA film. The growth of a group of 3 spherulites (black circles), with images acquired at 1 minute (A) and 10 minutes (B); The centre of the same spherulites as their growth impinges on each other (white arrows) after 20 minutes is shown in (C) and 35 minutes in (D). The largest spherulite in D is 134 µm (red line). Image capture was stopped when the spherulite growth impinged on each other and saturated the field of view.

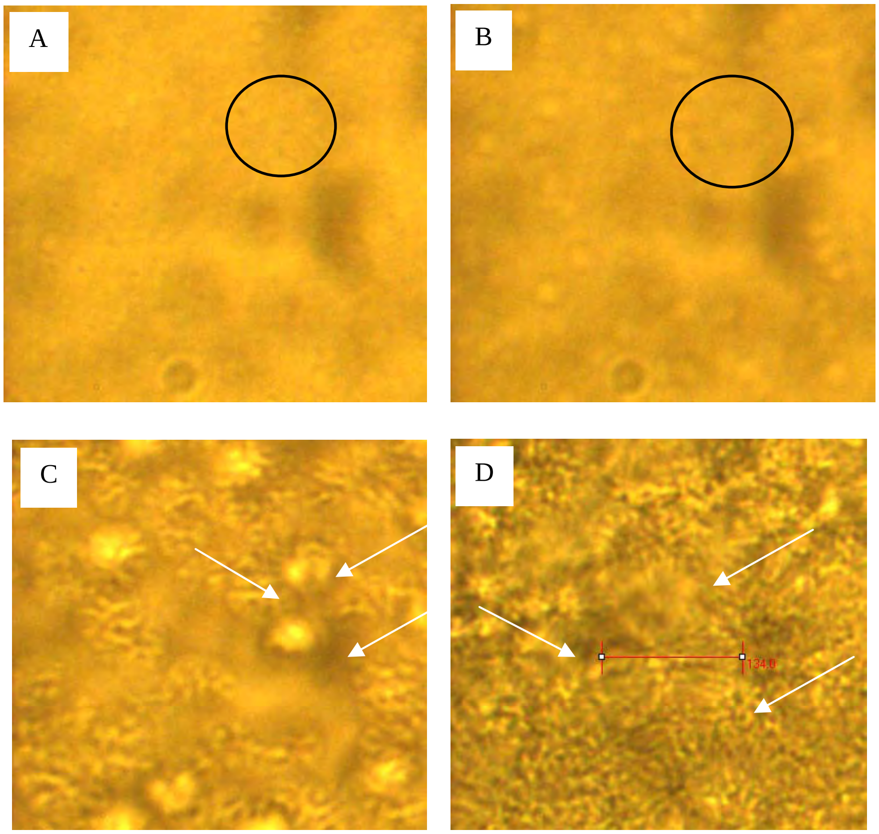

**Figure 4.15: Images acquired through hotstage microscopy during isothermal crystallisation of PLA film at 110 $^{o}$C.**

Figure 4.16 is image C when viewed through cross polar filters, showing the birefringence of the spherulites as areas of orange and blue light.

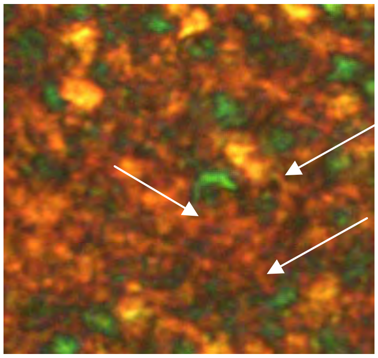

**Figure 4.16: Polarised light image of (C) above, showing birefringence of the PLA spherulites consistent with 'Maltese cross' effect.**

As shown in figures 4.15 A and B, there is a large amount of variation in growth rate between spherulites; there a number of factors that could cause this variation. Crystallisation is an exothermic reaction; it gives out heat. If there are a number of spherulites in a given area, the heat given out by the crystallisation process will raise the local temperature, increasing the crystallisation temperature. In the cluster of 4 spherulites enclosed by the circle in 4.15 B, the local temperature will be raised more than in the polymer surrounding it, thereby decreasing the crystallisation rate. Isolated spherulites will therefore have the fastest growth rate, and will grow larger than spherulites clustered together. Another explanation for the variation in growth rate could be explained by the position of the spherulite with respect to the outside of the sample. The sample is heated from the outside edge; therefore the temperature in the centre of the sample will be coolest. If the local heat is greater at a particular spherulite compared to another it may affect its crystallisation rate and thus growth rate. The heat transfer across the sample is affected by its thickness; less heat will transfer across a thick sample. If the sample is thicker in a particular area the local temperature will be lower, therefore affecting growth rate, it may also cause variability between samples. This is more likely to have happened in the samples containing silica, as the increasing silica content restricted the amount by which the films could be melt-pressed at the preparation stage. The saturation times and final spherulite sizes are presented in table 4.4.

**Table 4.4: Spherulite impingement time and final diameter**

| Sample | 1st sighting (minutes) | Impingement time (minutes) | Final diameter (µm) |
|---|---|---|---|
| PLA | 10-12 | 35 | 135 - 150 |
| PLA + 2.0% silica | 8-10 | 32-35 | 15 - 16 |
| PLA + 9.1% silica | 2 | 10 | 10 - 13 |
| PLA + 16.7% silica | 1.5 | 3 | 4 - 6 |
| PLA + 23.1% silica | 1-1.5 | 2 | 4 - 6 |
| PLA + 28.6% silica | 0.5 | 1 | 4 - 6 |
| PLA + 33.3% silica | 0.5 | 1 | 4 - 6 |

The incorporation of silica within the films affected the thickness of the melt pressed films (silica grains ~ 150µm), this in turn influenced image quality because ideally they should have been 10-20 µm thick so that only one lamella layer could be seen; this may have been true for PLA alone, but as silica content increased it became more difficult to focus on/between the layers. However, from the usable images obtained and the data presented in table 4.4, it was apparent that the inclusion of silica within the solvent cast and melt pressed films nucleated spherulite formation (as indicated by the decreasing time of first sighting), increased the density of nucleation (indicated by decreasing spherulite size at impingement) and also increased the rate of spherulite growth (indicated by the decreasing time to impingement). This observation is supported by the data obtained from the crystallinity of the samples calculated from DSC experiments which show that in both the solvent cast films and the SCF processed foams the presence of silica up to 23.1% increases the crystallinity of the samples, but inhibits any further crystal growth at silica levels greater than 23.1%.

### 4.3.3 Mechanical Strength testing

Table 4.5 presents the physical data of the scaffolds used in the mechanical strength tests and Figure 4.17 presents the stress-strain curve obtained from the compression testing of the SCF processed scaffolds to the point of failure. The increasing slope of the gradient indicates more plastic and less elastic behaviour with the addition of silica. The gradient of this portion of the stress-strain curve (Eq's 4.4 and 4.5) gives the elastic modulus (Youngs' modulus) of the scaffolds (Eq 4.6) and these values are presented in figure 4.18. It can be seen that with the addition of 23.1% silica or higher, the bulk modulus increases above that obtained in the absence of silica, following an approximately linear relationship.

**Table 4.5: Dimensions of the scaffolds used in the mechanical strength tests. Errors given are standard deviation from the mean (n=5)**

| Wt% content silica | Average height of scaffolds (m) | Average surface area of scaffolds ($m^2$) |
|---|---|---|
| 0 | $6.9 \times 10^{-3} \pm 4 \times 10^{-4}$ | $6.7 \times 10^{-5} \pm 5 \times 10^{-6}$ |
| 4.8 | $7.0 \times 10^{-3} \pm 6 \times 10^{-4}$ | $8.3 \times 10^{-5} \pm 2 \times 10^{-6}$ |
| 9.1 | $6.6 \times 10^{-3} \pm 2 \times 10^{-3}$ | $6.2 \times 10^{-5} \pm 1 \times 10^{-5}$ |
| 16.7 | $6.8 \times 10^{-3} \pm 2 \times 10^{-3}$ | $7.5 \times 10^{-5} \pm 9 \times 10^{-6}$ |
| 23.1 | $7.0 \times 10^{-3} \pm 5 \times 10^{-4}$ | $7.7 \times 10^{-5} \pm 3 \times 10^{-6}$ |
| 28.6 | $6.9 \times 10^{-3} \pm 4 \times 10^{-4}$ | $7.1 \times 10^{-5} \pm 4 \times 10^{-6}$ |
| 33.3 | $6.1 \times 10^{-3} \pm 6 \times 10^{-4}$ | $5.8 \times 10^{-5} \pm 3 \times 10^{-6}$ |

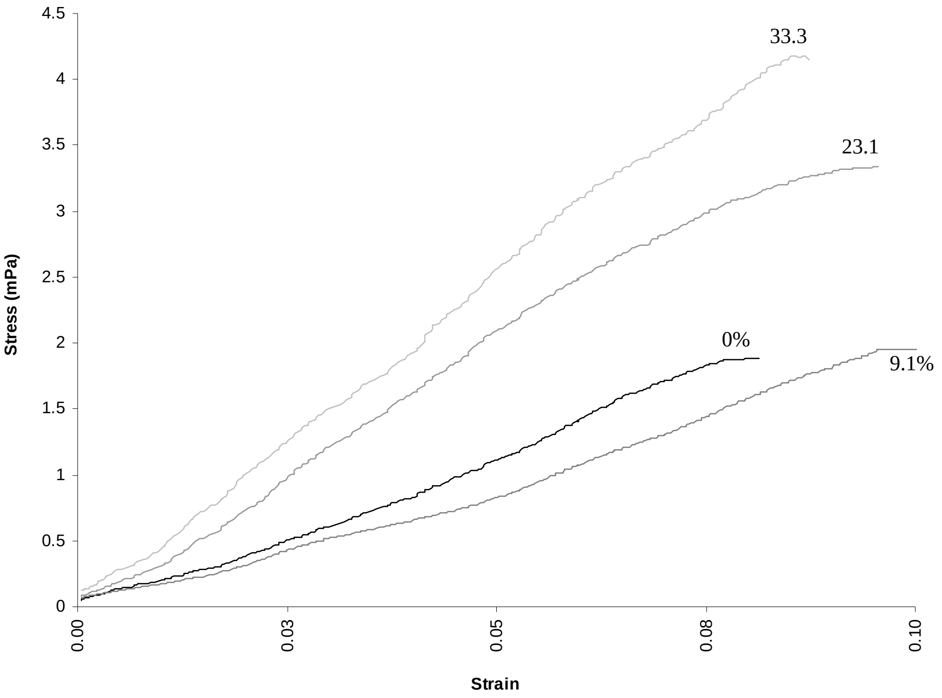

**Figure 4.17: Stress-strain curve to yield point obtained from compression testing of the SCF processed PLA and PLA/silica scaffolds**

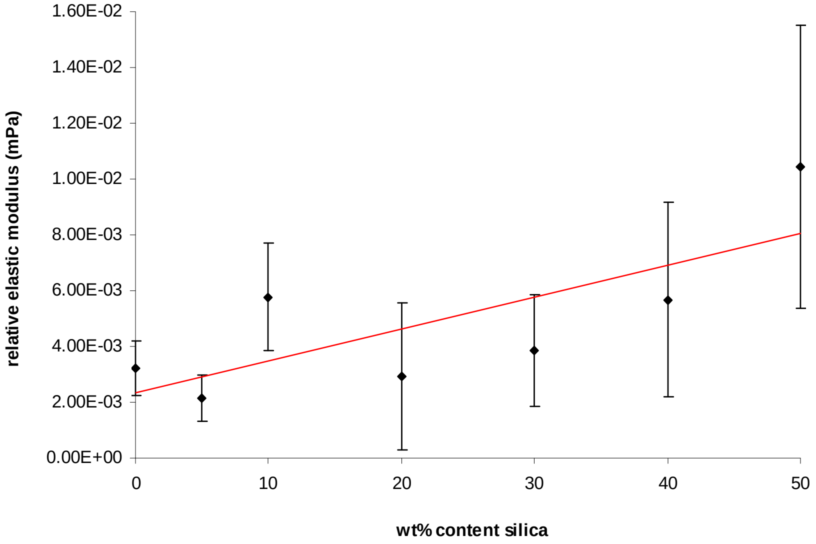

**Figure 4.18: Effect of silica content on elastic modulus of PLA scaffolds demonstrating an approximately linear relationship, the error bars indicate standard deviation from the mean (n=5)**

This is contradictory to that which might be expected from the Law of Mixtures, for which the elastic modulus is illustrated in figure 4.19.

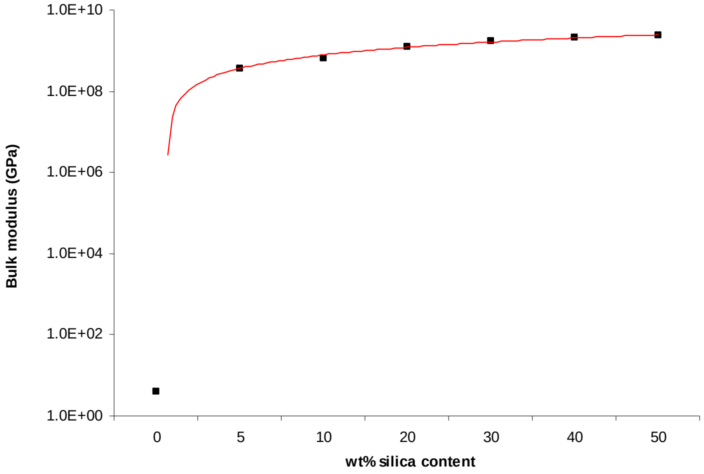

**Figure 4.19: Bulk modulus for a material containing silica that obeys the Law of Mixtures, showing the relationship to be linear**

The elastic modulus for PLA was previously found to be 4 GPa (RAPRA database: www.rapra.co.uk), and for fused silica to be 73.1 GPa (Science and Engineering encyclopedia: www.diracdelta.co.uk). The basic principle of the Law of Mixtures is that every component in the mixture be proportionally represented, hence the linear relationship between silica content and modulus (figure 4.19), which is a factor of $10^5$ different to that seen with the SCF processed foams (figure 4.18).

Table 4.5 shows the effect of silica addition on the load tolerated at the yield point – the point at which elastic behaviour becomes plastic behaviour. It can be seen that this value increased from 143.0 N to 248.8 N with the addition of up to 23.1% silica, but then decreased to 203.4 N with additions up to 33.3% silica. The standard deviation from the mean is high but this is known to be expected in mechanical testing data, with margins of error of up to 30% accepted to be normal (Anderson, Leaver *et al*, 2002). Even so, the loads tolerated at yield for the samples containing 23.1% and 28.6% silica are significantly higher than those obtained in the absence of silica (one way ANOVA, p=0.05).

**Table 4.6: Effect of silica content on load and strength at yield point of PLA scaffolds (errors given are standard deviation from the mean, n=5)**

| Wt % silica content | Load at yield (N) | Strength at yield (mPa) |
|---|---|---|
| 0 | 143.0 ± 27.8 | 2.1 ± 0.4 |
| 9.1 | 171.2 ± 26.7 | 2.5 ± 0.6 |
| 16.7 | 214.2 ± 48.5 | 2.9 ± 0.6 |
| 23.1 | 248.8 ± 54.4 | 3.1 ± 0.7 |
| 28.6 | 240.2 ± 56.8 | 3.2 ± 0.7 |
| 33.3 | 203.4 ± 36.1 | 3.6 ± 0.7 |

In an open or porous structure such as these polymer foams, once the elastic phase is exceeded energy is absorbed as the cell walls bend plastically before they buckle or fracture, which can be seen as a ‘saw-tooth edge’ appearance of the stress-strain curves. The scaffolds exhibited near constant strain through the walls collapsing and this was an observable phenomenon since none of the foams fractured outright, rather they became squashed flat.

The increase in elastic modulus could either be due to increasing silica content alone, or through the presence of the silica increasing the crystallinity of the polymer, thereby affecting its mechanical properties.

The former of these two statements is unlikely to be true, since if the silica alone was the cause of the increase in elastic modulus, the Law of Mixtures would be obeyed, and it can be seen from comparison of figures 4.18 and 4.19 that is clearly not the case.

It was shown in the DSC work of section 4.3.1 that the presence of silica increased the crystallinity of the SCF processed polymer foams. The effect of crystallinity on mechanical properties is complex, but essentially within the crystalline regions the polymer chain is packed more densely and there is a higher degree of inter-atomic bonding than in the amorphous regions, increasing the overall structural integrity and hence the elastic modulus. Amorphous regions that are totally enclosed by crystalline regions can also become reinforced by chain portions that bridge between the adjacent crystallites.

## *4.4 Conclusion*

The inclusion of silica within the polymer films was seen to promote crystal nucleation and growth in solvent cast films and this was evidenced by the data obtained through DSC measurements, namely increases in the values of up to 5J/g and 2°C (for $\Delta H_f$ and $T_g$ respectively) from 0% silica to 33.3% silica addition although $T_m$ appeared to be unaffected; crystallinity of the films increased by up to 6% (33.3% addition of silica); spherulite nucleation and growth was also observed through hotstage microscopy.

However, the SCF process appeared to return all materials to their amorphous form as evidenced by lack of $T_m$ on DSC. This loss of crystallinity was found to be a reversible process that could be restored by an isothermal conditioning process, a phenomenon which has been observed before (Wu *et al*, 2007).

The effect that silica had on the mechanical properties of the foamed samples was that as silica content increased, the foams exhibited more plastic behaviour than elastic behaviour. The load tolerated at yield increased by 60N (0% vs 33.3% silica addition) and the strength of the scaffolds was found to increase by 1.5 mPa (0% vs 33.3% silica content), and it was proposed that this was due to silica promoting crystallinity within the foams, and that crystalline regions have a higher elastic modulus than amorphous regions.

# Chapter 5: *In-vitro* and degradation behaviour of PLA and PLA-silica scaffolds

## *5.1 Introduction*

Degradation research involving polylactic acid appears to have two major focuses: the dependence of hydrolysis on pH, temperature and chemical structure of the polymer chains; and the transport processes of various chemicals such as water, ions ($H^+$, $OH^-$), pharmaceutical agents, and degradation products of polymers (Lyu *et al* 2007). The action of neutral media - buffered salt solutions (such as phosphate buffered saline (PBS) and Ringers solution) - enzymes and simulated body fluids (SBF) has also been considered (section 1.3 and 1.4).

The choice of the buffer (Ringers solution), enzyme (proteinase k) and experimental setup in the following studies was to make the *in vitro* environment as close as possible to the potential *in vivo* environment (for the purposes of the degradation experiments) and in addition, to optimise the experimental environment in the case of mineral deposition studies.

The experimental work described in this section was a preliminary study to investigate the *in-vitro* and degradation behaviour of PLA and PLA-silica scaffolds; the existing literature (section 1.3) has predominantly focused on the behaviour of 2D films with very little known about the behaviour of porous 3D structures, therefore the author regards this current work as unique. However, this also means that the results have had to be interpreted with a degree of caution with conclusions (where appropriate) being drawn from the 2D work.

## *5.2 Materials and methods*

Four scaffolds of each silica formulation (absent – 0% silica; high/middle – 16.7% silica; and high – 33.3% silica) were used for mineralisation studies in SBF; four scaffolds of each silica formulation (absent – 0% silica; middle – 9.1% silica; and high – 33.3% silica) were manufactured for each of the time points in each of the Ringers solution and enzyme degradation experiments (method as previously described in section 2.4.3).

Prior to immersion in the relevant solution the physical dimensions of each of the scaffolds was recorded in order to calculate scaffold density and porosity (as previously described in section 2.5.2). The scaffolds were then immersed in 70% ethanol in a sterile universal bottle for a minimum of 24 hours to sterilise the surface and any pores open to the surface, before being removed aseptically, blotted dry on sterilised filter paper and transferred to a sterile universal bottle containing Ringers or enzyme solution - or in the case of mineral deposition, to the designated flask within the continuous circulation system (figure 5.2). Any associated hydrolysis due to exposure to water or ethanol would have been uniform across all scaffolds as the treatment was the same in all cases.

All of the flasks and tubing that made up the continuous circulation apparatus were autoclaved at 121$^{o}$C for 15 minutes prior to use.

### 5.2.3 Development of experimental methodology

A study carried out found that a media flow rate of 3 ml min$^{-1}$ was best for stimulating mineral matrix deposition on marrow stromal osteoblasts in perfusion culture (Bancroft *et al*, 2002), and no other literature could be found that justified, validated or compared the use of flow rates, so that is why this value was chosen to be used in the mineral deposition method that follows.

Initial studies carried out by the author on degradation of PLA films (0.5 x 0.5 x 0.1 cm) in Ringers solution over a period of 16 weeks showed no mass loss or evidence of surface erosion (data not presented); one literature study of PCL, PEG and PDLA films (0.5 x 0.5 x 0.04 mm) (Wang *et al*, 2006), noticed considerable mass loss of the PDLA at 16 weeks, with the samples being non-viable at 20 weeks. Degradation was monitored by mass loss, SEM, SEC and DSC. The film sizes were dramatically different to those of this author, but these results were used to inform the planning of the following Ringers degradation experiments.

Experiments that have utilised proteinase k at a concentration of 0.2 mg $ml^{-1}$ to degrade PLA or PLA composite films of between 80 μm and 200 μm thickness cite degradation times of 3 hours and 72 hours, respectively (He, 2007; Tsuji *et al* 2007). The general usage range of proteinase k was known to be 0.05 – 0.1 mg $ml^{-1}$ (Sigma aldrich user information for product number P6556), and given the dimensions of the scaffolds (compared to those of the films) it was decided to use 0.1 mg $ml^{-1}$ over a period of around 14 days.

### 5.2.4 SBF

SBF was made according to the method described by Kokubo in 2006. The reagents were added in the order specified in table 5.1 to 700 ml distilled, deionised water. The water was maintained at 37$^{o}$C ± 1$^{o}$C by placing it on a stirrer-hotplate. Reagents were added stepwise only when the preceding reagent had fully dissolved. Before the addition Tris (Tris (hydroxymethyl)aminomethane)), the pH of the solution was recorded with a calibrated pH meter; Tris was added a little at a time, allowing the pH to stabilise between each addition. Finally, reagent 10 (1.0M HCl) was added drop-wise to adjust the pH of the solution to 7.4. Taking the amount of HCl added into consideration, the solution was made up to 1 litre with distilled, deionised water. Once the solution was thoroughly mixed, the bottle was sealed and autoclaved at 121 $^{o}$C for 15 minutes.

**Table 5.1: Reagents and amounts required to make 1 litre of SBF (Kokubo, 2006)**

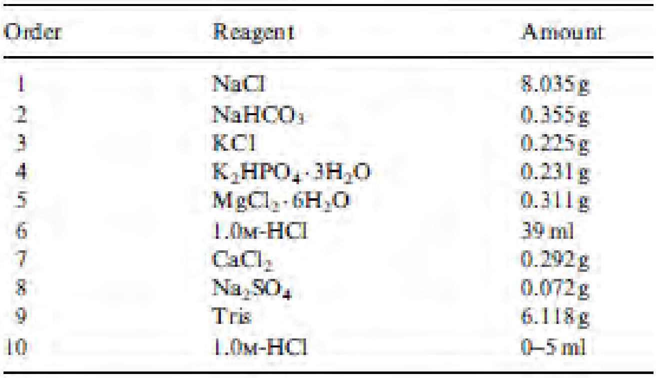

| Order | Reagent | Amount |
|---|---|---|
| 1 | NaCl | 8.035 g |
| 2 | $NaHCO_3$ | 0.355 g |
| 3 | KCl | 0.225 g |
| 4 | $K_2HPO_4 \cdot 3H_2O$ | 0.231 g |
| 5 | $MgCl_2 \cdot 6H_2O$ | 0.311 g |
| 6 | 1.0M-HCl | 39 ml |
| 7 | $CaCl_2$ | 0.292 g |
| 8 | $Na_2SO_4$ | 0.072 g |
| 9 | Tris | 6.118 g |
| 10 | 1.0M-HCl | 0–5 ml |

## 5.2.4 Mineral deposition study

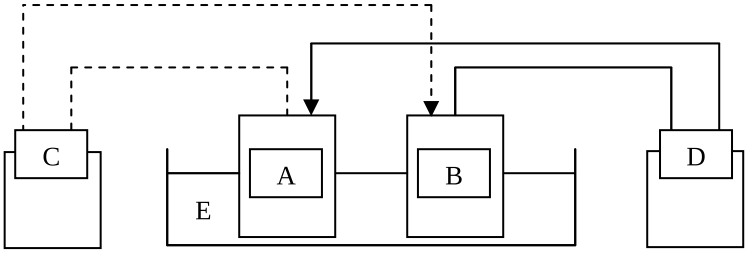

**Figure 5.1: Continuous circulation apparatus for mineral deposition study.**

Key: A = Sample reservoir; B = SBF reservoir;
C = peristaltic pump that circulates from A to B;
D = peristaltic pump that circulates from B to A
E = water bath @ 37 $^{o}$C
Dotted line = flow of SBF A to B;
Solid line = flow of SBF B to A

The four sterilised samples were aseptically placed into the sample reservoir (figure 5.1 A) and the associated cap and tubing attached. The SBF reservoir (figure 5.1 B) was essentially the flask that the SBF was made up in, with a sterile cap and tubing attached. The tubing was fed through the respective pumps, and the flow rate was set at 3 ml min$^{-1}$; initially only pump D was primed in order to transfer SBF into A, but when the levels of SBF were equal in both reservoirs pump C was primed. The level of each of the reservoirs was checked twice daily. The two reservoirs were maintained at 37°C by immersing them to half height in a covered water bath. At 7 day intervals, the pumps were stopped and the samples were removed from A and were blotted dry on sterile filter paper until no further liquid could be removed. The wet mass of each was recorded; the samples were then oven dried overnight. The dry masses were then recorded, and the scaffolds were scanned by microCT, following the same parameters as in section 2.4.4. The samples were then briefly immersed in 70% ethanol, blotted dry on sterile filter paper, and returned to the sample reservoir, where the cap was reattached and the pumps were started again.

On at least two occasions, this transfer process introduced contamination into the SBF; this meant that the entire circulating system (tubing, flasks and caps) had to be decontaminated, washed and re-sterilised, and that the scaffolds were washed briefly in distilled water and were immersed in 70% ethanol for a minimum of 24 hours. The process was then continued from the same time point with fresh SBF.

### 5.2.5 Degradation of PLA and PLA/silica scaffolds by Ringers solution

A decision was made to sacrifice the scaffolds at each time point during the Ringers and proteinase k degradation and to use a shaker incubator system instead, rather than to re-use them due to contamination and sterilisation issues encountered through the use of the continuous circulation system in the mineral deposition study.

Ringers solution was made up following the manufacturers instructions (Fisher scientific, catalogue number BR052G) using deionised water that had been sterilised by autoclaving at 121°C for 15 minutes. 20 ml was aliquoted into sufficient numbers of 30 ml universal bottles for the time points that were needed (16 to 20 weeks). Four scaffolds were aseptically placed into each universal for each time point, the universals were placed into a plastic rack, and the rack was placed into an orbital shaker – incubator set at 37 $^{o}$C and 120 rpm. At each designated time point the universal was removed from the rack in the shaker, the surface was blotted dry on filter paper until no further liquid was removed. The wet mass of each was recorded; the samples were then oven dried overnight. The dry masses were then recorded, and the scaffolds were scanned by microCT, following the same parameters as in chapter 2. The 0% sample was degraded initially to ascertain the correct timescale, and the 9.1% and 33.3% were then degraded in subsequent studies.

### 5.2.6 Degradation of PLA and PLA/silica scaffolds by Proteinase k

Tris buffer solution was made up by dissolving Tris buffer powder (Sigma Aldrich catalogue number 154563) in 100 ml sterile deionised water to achieve a final pH of 8.4. The proteinase k was reconstituted with 1 ml of sterilised deionised water, and was aseptically added to the 100 ml Tris buffer. 5 ml was aliquoted into sufficient numbers of bijoux for the time points that were needed (2 day intervals over 2 weeks). A single scaffold was aseptically placed into each bijou for each time point, the bijoux were then placed into a plastic rack, and the rack was placed into an orbital shaker – incubator set at 37 $^{o}$C and 120 rpm. At each designated time point the universal was removed from the rack in the shaker, the surface was blotted dry on filter paper until no further liquid was removed. The wet mass of each was recorded; the samples were then oven dried overnight. The dry masses were then recorded, and the scaffolds were scanned by microCT, following the same parameters as in section 2.4.4. The 0% sample was degraded initially to ascertain the correct timescale, and the 9.1% and 33.3% were then degraded in subsequent concurrent studies. The enzyme was refreshed every 3-4 days to maintain activity, in accordance with current literature practice (Tsuji, 2001; Wang, 2006) by removing 1 ml of the ‘used’ enzyme solution and replacing with 1 ml fresh solution. The removed aliquot was saved for furhter analyses.

### 5.2.7 von Kossa staining technique

The von Kossa stain was used to determine the presence or absence of phosphate in the samples post mineral deposition study. The nitrate component of silver nitrate was displaced by phosphate in the sample, which then underwent photochemical degradation to form silver on exposure to light. Alizarin red was then used as a counter stain to detect calcium deposits. The scaffolds were cut into 5mm thick sections using a scalpel and were placed into a 6 well microtitre tray. A plastic disposable pipette was then used to cover the samples in equal volumes of silver nitrate solution (~ 5 ml), and the microtitre tray was covered with its clear plastic lid which was secured in place with sticky tape and placed in front of a source of strong natural light. Colour development was allowed to continue for 3 hours, after which each section was thoroughly washed in deionised water (approximately 6 changes of water), blotted dry with filter paper and the placed in a second 6 well microtitre tray. 5 ml of Alizarin red was used to cover the samples, and colour development was monitored over 30 minutes. The samples were then washed and dried as described above. Images were recorded with a Canon Ixus digital camera.

All residues and run off that may have contained silver nitrate were disposed of according to the departments’ hazardous waste guidelines.

### 5.2.8 Elemental analysis

Sections of the scaffolds post mineral deposition study were obtained (as previously described in section 2.4.5.1) and were scanned by environmental SEM (ESEM; (Phillips XL30)), which was also capable of carrying out energy dispersive spectroscopy (EDS) using the INCA EDS system. Spectra were analysed using HKL software and images were acquired by use of a Nordlys S camera.

The supernatants from the samples degraded in Ringers solution and Tris-proteinase k were analysed by high performance liquid chromatography (HPLC) using an Agilent series 1200 pump and refractive index detector, and a Phenomenex Rezex ROA $H^+$ reverse phase column to determine the constituent products of the degradation process. The mobile phase was 0.5% formic acid, the flow rate was 0.5 ml $min^{-1}$; the analysis was carried out at 40 $^{o}$C. The HPLC column was calibrated for lactic acid by running standards of 50, 20, 10, 5 and 1.25 mM lactic acid (diluted in deionised water). The $R^2$ value of the calibration curve was 0.997. It was found that the retention time of lactic acid in the column was 16.74 minutes. The sample volume was ~150µl

## *5.3 Results and discussion*

### 5.3.1 Mineral deposition studies

The scaffolds were immersed in SBF for periods of up to 28 days, in order to monitor the deposition of mineral on the surface of the scaffold. Over the first seven days there was a marked increase in the mass of the 33.3% silica-modified scaffolds of 37% ± 2%, with a further increase in mass to a total 39% ± 2% increase at 14 days, decreasing to 37% ± 3% for the remainder of the study (Figure 5.2).

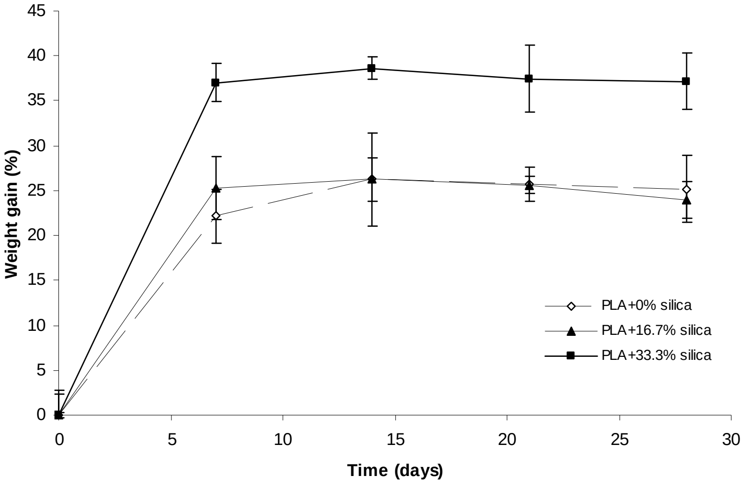

**Figure 5.2: % mass gains of the PLA and PLA-silica scaffolds during ageing in SBF (± % standard deviation from the mean, n=4).**

In comparison, in the 0% silica scaffolds there was only a 22% ± 3% mass increase during the first 7 days, 26% ± 5% after 14 days, decreasing to 25% ± 4% after 28 days. The mass increases in the sample containing 16.7% silica were 25% ± 6% to 7 days, 26% ± 5% to day 14, decreasing to 24% ± 4% at the end of the incubation period.

The deposition of a mineral phase on the surface of the scaffold materials was confirmed using von Kossa and Alizarin red staining. At time zero (Figures 5.3 A, B and C), little or no staining was apparent on the surface of the scaffolds. Following 28 days of ageing in SBF all scaffolds were heavily stained indicating the presence of calcium and phosphate salts (Figures 5.3 D, E and F). The intensity of the staining on the surface of the scaffolds modified with silica was considerably higher than on the surface of the non-modified material, indicating more extensive mineral deposition. Alizarin red (orange colour) was indicative of the presence of calcium, von Kossa (black colour) was indicative of the presence of phosphate.

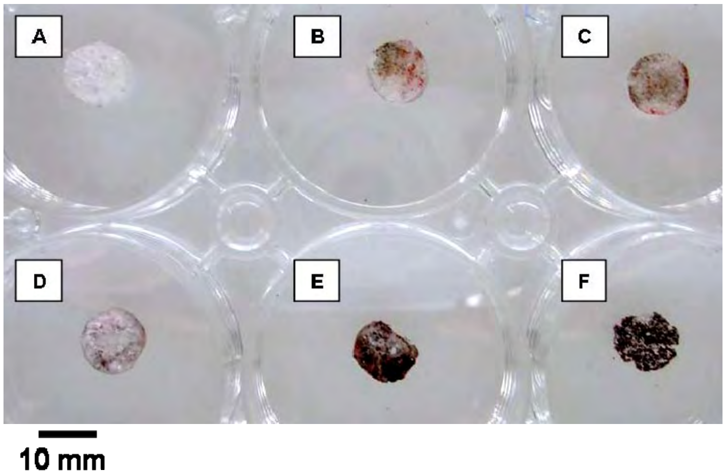

**Figure 5.3: Foamed PLA scaffolds stained using the von Kossa method to show the presence of mineral deposits.** A), B) and C) **Pure PLA, PLA containing 16.7wt% and 33.3wt% silica respectively prior to ageing.** D), E) and F) **Pure PLA, PLA containing 16.7wt% and 33wt% silica respectively following ageing in SBF for 28 days.**

The bioactivity of bone tissue engineering scaffold materials has frequently been assessed by monitoring the deposition of calcium salts on the surface of the scaffold in simulated body fluid. In this study, a difference of up to 12% mass increase was noted for the scaffolds modified with silica compared to the non silica-modified material during the first seven days of immersion.

It is thought that a reduction in the pore size distribution of the scaffold increased the surface area available for the formation of the calcium salt. Furthermore, it is possible that the silica particles provided nucleation sites for the formation of the calcium salt on the surface of the material, as is the case when Bioglass is incorporated into a scaffold (1.1.3.2). It is also possible that the presence of silica in combination with the reduced pore size distribution fascilitated hydrolysis of the PLA, as evidenced by mass loss (subsequent to the initial mass gain to day 14) of up to 2% in silica containing scaffolds as compared to only 1% in PLA alone at day 28.

Sections of the scaffolds were examined by environmental SEM which enabled the mineral deposits on the surface of the scaffolds to be visualised; elemental analysis of the deposits by

Energy Dispersive Spectroscopy confirmed that they were calcium phosphate based (figure 5.4), as did FTIR spectroscopy comparing PLA scaffold surfaces exposed and unexposed to SBF (figure 5.5). The presence of sodium, potassium and chloride ions are due to the other components of the SBF.

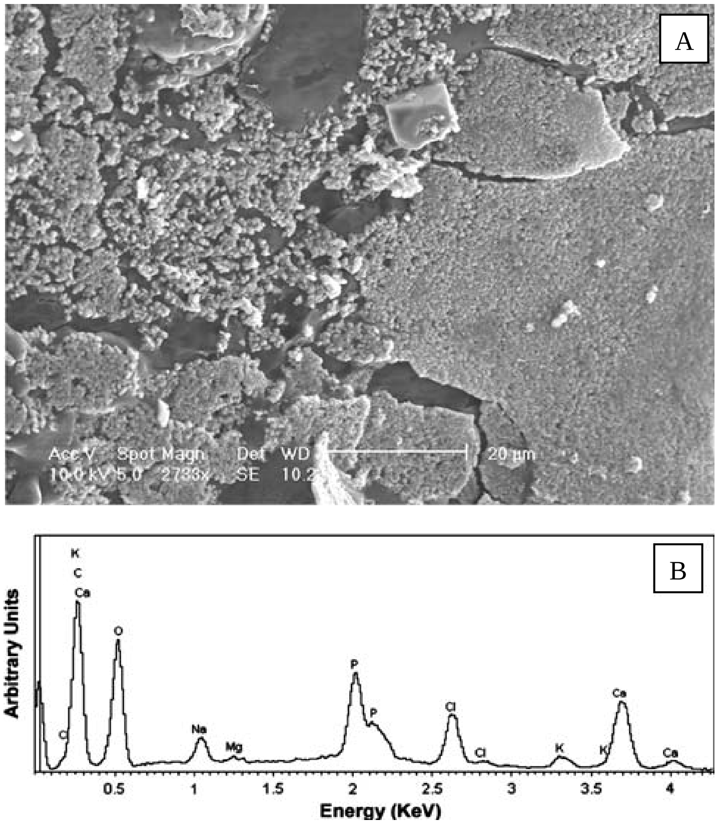

**Figure 5.4: A: Environmental scanning electron micrograph of the mineral deposit identified on the surface of a polymer scaffold containing 33.3% silica after 28 days immersion in SBF;**

**B: EDS demonstrated that the deposit was predominantly calcium phosphate based.**

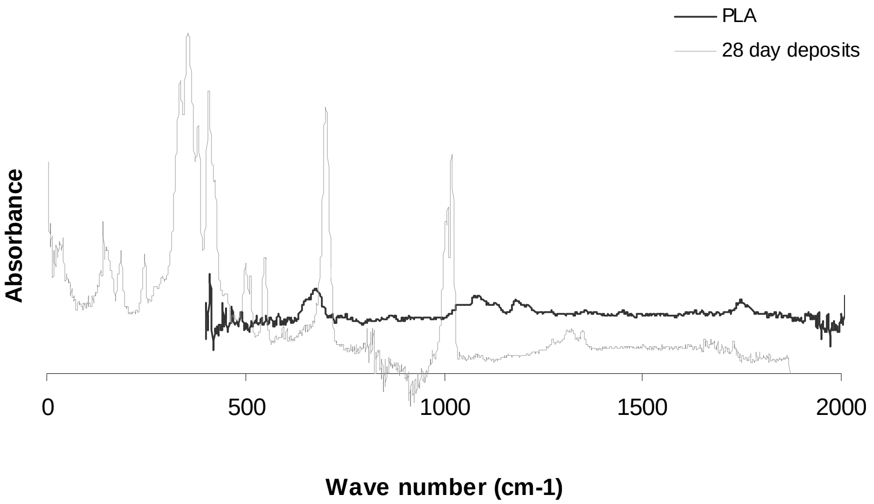

**Figure 5.5: FTIR of mineral deposits compared with PLA. Phosphate group, 1000 cm$^{-1}$(mineral deposit); ester (C-O) bond stretch, 1100 cm$^{-1}$; ketone (C=O) stretch, 1750 cm$^{-1}$ (both PLA). (Absorbance units are arbitrary).**

## 5.3.2 Ringers degradation

The average mass of the four scaffolds at each time point (initial, wet and dry) was calculated by:

$$\text{Average mass} = (\text{mass}_1 + \text{mass}_2 + \text{mass}_3 + \text{mass}_4) / 4$$

[Eq 5.1]

The % mass loss of the scaffolds was calculated from the average initial and final (dry) masses of the scaffolds according to the following formula:

$$\%\ \text{mass loss} = ((\text{initial mass} - \text{final mass}) / \text{final mass}) \times 100$$

[Eq 5.2]

The % water (from the Ringers buffer) absorbed by the scaffolds was calculated from the following equation:

$$\%\ \text{water absorbed} = ((\text{wet mass} - \text{final mass} / \text{final mass}) \times 100$$

[Eq 5.3]

Data relating to the physical changes exhibited by the scaffolds will be presented initially, followed by data relating to the HPLC analysis and assignation of peaks.

*Ringers buffer degradation of PLA and PLA-silica scaffolds*

Through visual inspection of the scaffold surfaces it was determined (unilaterally) that the surfaces which were initially white and smooth became duller and developed a ‘rough’ texture. By week 19, pores in the underlying scaffold structure could be seen through the outer surface and by week 20 some of these pores were open to the surface. In addition, visible fragments (~0.5 to 1mm long) could be seen in the buffer solution from the outset, and by week 20 some of the fragments were quite large (>1mm). It was also noted during transfer of the scaffolds out of universals for weighing that the surface of the scaffolds had softened, as evidenced by them sticking temporarily to the forceps as they were lifted, therefore care was taken to ensure the surface of the scaffolds was not damaged.

The mass loss data obtained from the degradation of scaffolds containing PLA alone are shown in table 5.2. It can be seen that the % water absorbed increased by 40.7% from week 17 to week 20. Over the same period of time, the mass loss (compared to the mass at week 0) increased from 2.4 % (week 17) to 21.3% (week 20); the pH of the buffer solution decreased from 7.2 (0 weeks) to 6.3 (20 weeks).

**Table 5.2: Average mass data obtained from Ringers degradation of PLA scaffolds containing 0% silica**

| Time point (weeks) | initial mass (mg) | wet mass (mg) | %$H_2O$ absorbed | Dry (final) mass (mg) | % mass loss |
|---|---|---|---|---|---|
| 17 | 102.5 ± 8.8 | 131.0 ± 8.6 | 30.9 | 100.0 ± 8.3 | 2.4 |
| 18 | 102.9 ± 8.6 | 131.3 ± 16.4 | 36.6 | 96.0 ± 11.3 | 6.6 |
| 19 | 96.9 ± 11.1 | 118.9 ± 12.3 | 47.3 | 80.7 ± 6.4 | 16.8 |
| 20 | 102.9 ± 5.4 | 176.5 ± 22.9 | 71.6 | 80.9 ± 6.7 | 21.3 |

HPLC analysis of the scaffolds (figure 5.6) did not show an elution peak at 16.7 minutes therefore the degradation of the PLA within the scaffolds did not lead to the production of lactic acid, and this observation was supported by the minimal drop in pH throughout the incubation period. There was however an elution peak at ~26.2 minutes which could possibly be due to larger chain fragments. The trough at ~ 18 minutes was the mobile phase eluting from the column and was present in all samples regardless of silica content.

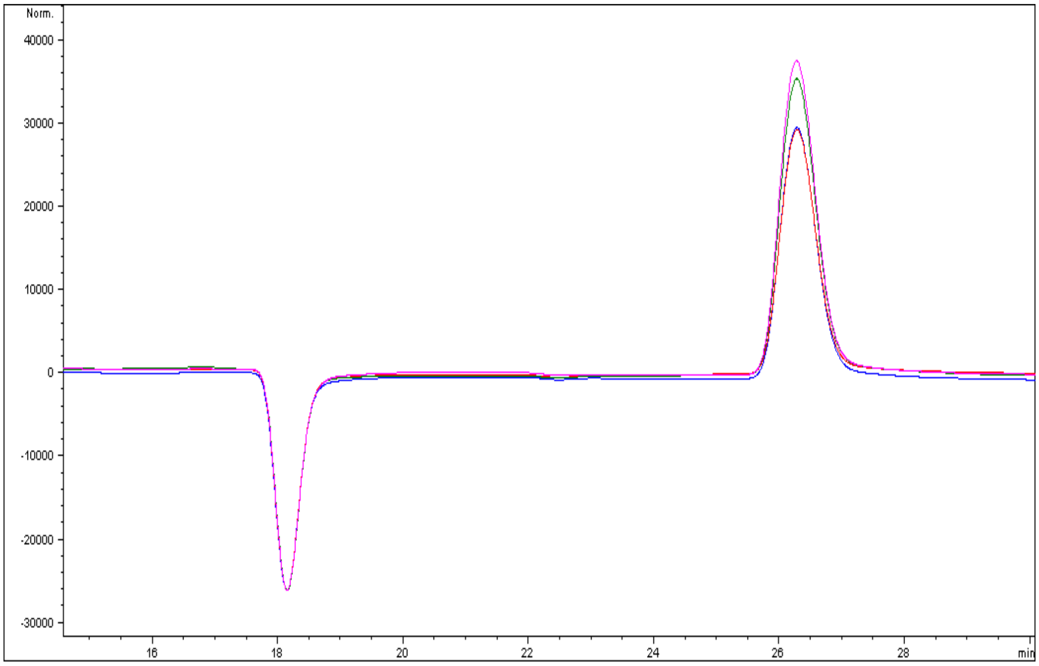

**Figure 5.6: HPLC trace of scaffolds containing 0% silica after degradation in Ringers buffer showing absence of a lactic acid peak at 16.74 minutes, but the presence of a second peak at a later retention time of around 26 minutes.** (Colour code: blue wk 17; red wk 18; green wk 19; pink wk 20)

*Ringers buffer degradation of PLA scaffolds containing silica.*

Table 5.3 presents the data obtained from the degradation in Ringers buffer of PLA scaffolds containing 9.1% silica and table 5.4 presents the data of the scaffolds containing 33.3% silica.

**Table 5.3: Average mass data obtained from Ringers degradation of PLA scaffolds containing 9.1% silica (errors given are standard deviation from the mean, n=4)**

| Time point (weeks) | initial mass (mg) | wet mass (mg) | % $H_2O$ absorbed | dry (final) Mass (mg) | % mass loss |
|---|---|---|---|---|---|
| 17 | 99.9 ± 4.7 | 153.2 ± 10.8 | 53.9 | 99.5 ± 4.8 | 0.4 |
| 18 | 126.5 ± 18.8 | 229.3 ± 43.2 | 81.2 | 126.2 ± 18.9 | 0.3 |
| 19 | 137.7 ± 6.1 | 237.7 ± 7.2 | 72.9 | 137.5 ± 6.5 | 0.1 |
| 20 | 127.0 ± 17.5 | 218.9 ± 36.6 | 72.7 | 126.8 ± 17.3 | 0.2 |

**Table 5.4: Average mass data obtained from Ringers degradation of PLA scaffolds containing 33.3% silica (errors given are standard deviation from the mean, n=4)**

| Time point (weeks) | initial mass (mg) | wet mass (mg) | % $H_2O$ absorbed | Dry (final) Mass (mg) | % mass loss |
|---|---|---|---|---|---|
| 17 | 107.8 ± 8.5 | 174.7 ± 29.4 | 62.1 | 106.6 ± 8.9 | 1.1 |
| 18 | 127.0 ± 24.5 | 225.9 ± 39.7 | 77.8 | 125.9 ± 23.9 | 0.8 |
| 19 | 145.0 ± 3.6 | 233.5 ± 7.6 | 61.0 | 144.5 ± 4.8 | 0.5 |
| 20 | 115.1 ± 11.2 | 181.7 ± 19.2 | 58.7 | 114.5 ± 11.0 | 0.6 |

In both sets of scaffolds it can be seen that the % water absorbed initially increased from week 17 to week 18 but then subsequently decreased to week 20. The 9.1% silica scaffolds appeared to have a higher capacity for the absorption of water than the 33.3% silica scaffolds. At week 17 the mass loss for the 9.1% silica scaffolds was 0.4% but this was had slowed to 0.2% at week 20; similarly the 33.3% silica scaffolds lost mass of 1.1% in week 17 but this had slowed to 0.6% in week 20. This mass loss was accompanied by a dramatic decrease in the pH from 7.2 to 3.3 (9.1% silica) and 3.0 (33.3% silica) over the 20 week period.

HPLC analysis of the scaffolds containing 9.1% and 33.3% silica (figure 5.7) gave elution peaks at 16.7 minutes indicating degradation of the PLA to lactic acid (an observation that was supported by the massive decrease in pH throughout the duration of the experiment) and a peak corresponding to the unknown compound at 26.2 minutes.

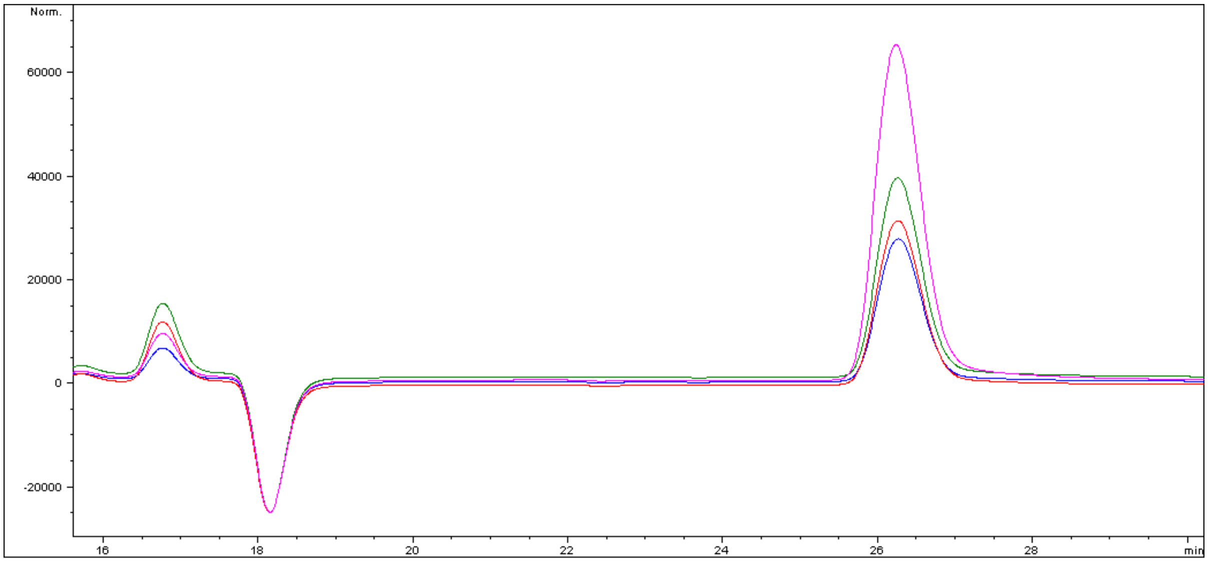

**Figure 5.7: HPLC elution curves typical of PLA scaffolds containing 9.1% and 33.3% silica after degradation in Ringers buffer. The presence of a lactic acid peak at 16.74 minutes, and also the presence of a second peak at a later retention time of around 26 minutes can clearly be seen.** (Colour code: blue wk 17; red wk 18; green wk 19; pink wk 20)

### 5.3.3 Enzyme degradation

*Tris-proteinase k degradation of PLA scaffolds containing 0% silica*

The data obtained from the degradation of scaffolds containing PLA by proteinase k is shown in table 5.5. It can be seen that the % water absorbed increased initially by 56.9% from day 3 to day 6, but then decreased dramatically. At day 3, the mass loss was 15.4% but this mass loss slowed in the subsequent days to 6.3% (day 16). Observations of the scaffold surface determined that the degradation appeared to happen steadily. Pores in the underlying scaffold structure could be seen through the outer surface at day 3 and by day

9 some were open to the surface; by day 13 all of these pores were open to the surface. Large fragments (~1 mm in size) could be seen in the buffer solution from the outset.

**Table 5.5: Average mass data obtained from proteinase k degradation of PLA scaffolds**

| Time point (days) | initial mass (mg) | Wet mass (mg) | %$H_2O$ absorbed | dry (final) mass (mg) | % mass loss |
|---|---|---|---|---|---|
| 3 | 141.4 ± 8.9 | 160.1 ± 29.4 | 33.8 | 119.7 ± 9.0 | 15.4 |
| 6 | 95.6 ± 10.5 | 162.6 ± 26.4 | 90.7 | 85.3 ± 7.6 | 10.8 |
| 9 | 108.3 ± 13.3 | 123.4 ± 19.2 | 24.3 | 99.2 ± 15.0 | 8.4 |
| 13 | 106.5 ± 15.6 | 124.2 ± 19.4 | 6.5 | 116.6 ± 16.9 | 6.1 |
| 16 | 126.3 ± 9.2 | 159.7 ± 15.5 | 34.9 | 118.3 ± 11.2 | 6.3 |

Figure 5.8 shows the results of the HPLC analysis of the supernatants obtained from each time point of the enzyme degradation experiments with PLA scaffolds. There are peaks at 16.74 minutes corresponding to lactic acid as well as the unknown compound at 26 minutes; there is also the hint of a peak at around 15.5 minutes.

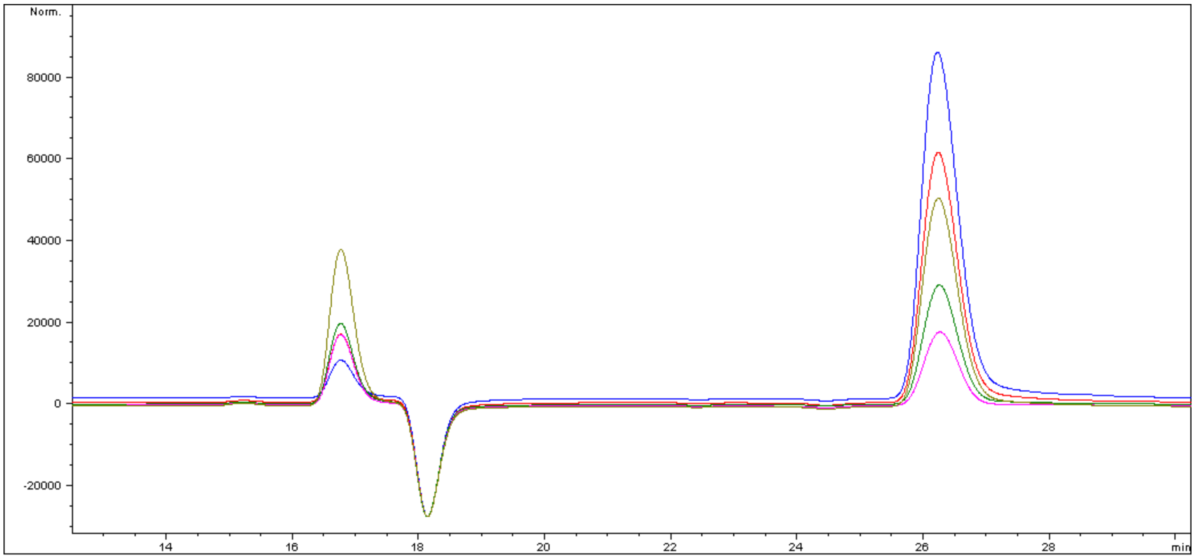

**Figure 5.8: HPLC analysis of the supernatants obtained from the enzyme degradation experiments with PLA scaffolds.** (Colour code: Blue Day3; red Day6; green Day9; pink Day13; brown Day16)

*Tris-proteinase k degradation of PLA scaffolds containing 9.1% silica and 33.3% silica*

The data obtained from the degradation of PLA scaffolds containing 9.1% silica by proteinase k is shown in table 5.6 and from 33.3% silica in table 5.7. For the 9.1% silica it can be seen that the % water absorbed decreased initially by 16.1% from day 3 to day 6 but then increased to 65.0% on day 16, whereas for 33.3% silica it increased throughout with the exception of the final day. There was a general increase in mass loss from 8.2% on day 3 to 14.1% on day 16 (9.1% silica) and from 8.1% to 16.8% (33.3% silica). Observations of the scaffold surface determined that the degradation happened almost immediately; pores became visible on the scaffold surface at day 3 and by day 9 most of these pores were open to the surface. Visible fragments could be seen in the buffer solution and some were quite large at the final time point (~2 mm in size).

**Table 5.6: Average mass data obtained from proteinase k degradation of PLA scaffolds containing 9.1% silica (errors given are standard deviation from the mean, n=4)**

| Time point (days) | Initial mass (mg) | Wet mass (mg) | %$H_2O$ absorbed | Dry (final) mass (mg) | % mass loss |
|---|---|---|---|---|---|
| 3 | 140.8 ± 6.5 | 203.3 ± 19.9 | 57.2 | 129.3 ± 7.3 | 8.2 |
| 6 | 120.4 ± 12.3 | 167.7 ± 20.9 | 41.1 | 118.8 ± 13.6 | 1.3 |
| 9 | 133.4 ± 7.0 | 154.2 ± 14.0 | 43.0 | 107.8 ± 12.8 | 19.2 |
| 13 | 129.1 ± 10.8 | 178.9 ± 31.4 | 55.8 | 114.8 ± 9.7 | 11.0 |
| 16 | 126.2 ± 5.6 | 178.7 ± 23.0 | 65.0 | 108.3 ± 4.4 | 14.1 |

**Table 5.7: Average mass data obtained from proteinase k degradation of PLA scaffolds containing 33.3% silica (errors given are standard deviation from the mean, n=4)**

| Time point (days) | Initial mass (mg) | wet mass (mg) | %$H_2O$ absorbed | Dry (final) mass (mg) | % mass loss |
|---|---|---|---|---|---|
| 3 | 158.8 ± 26.7 | 201.7 ± 38.7 | 38.2 | 145.9 ± 26.1 | 8.1 |
| 6 | 124.9 ± 23.2 | 155.8 ± 40.5 | 40.1 | 111.2 ± 23.1 | 11.0 |
| 9 | 116.5 ± 9.8 | 155.6 ± 18.1 | 47.8 | 105.3 ± 11.8 | 9.6 |
| 13 | 156.3 ± 28.6 | 207.5 ± 42.8 | 59.6 | 130.0 ± 23.7 | 16.8 |
| 16 | 131.6 ± 4.7 | 163.2 ± 5.7 | 46.7 | 111.3 ± 4.3 | 15.4 |

Figure 5.9 shows a representative HPLC analysis of the supernatants obtained from the enzyme degradation experiments with PLA scaffolds containing 9.1% and 33.3% silica. There are peaks at 16.7 minutes corresponding to lactic acid as well as at 26 minutes as noted previously; in addition there is a new peak at 15.5 minutes.

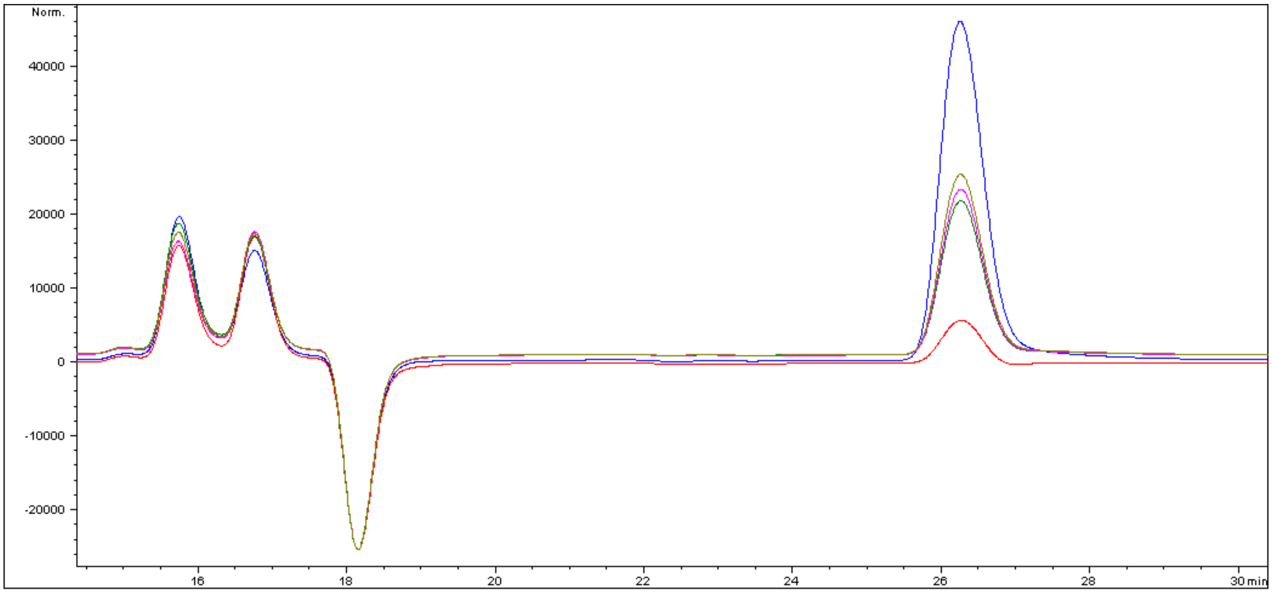

**Figure 5.9: HPLC elution curves typically obtained from the supernatants of the enzyme degradation of scaffolds containing 9.1% and 33.3% silica; note the new peak at 15.5 minutes.**

(Colour code: Blue Day3; red Day6; green Day9; pink Day13; brown Day16)

Table 5.8 presents the peak analysis data for all of the HPLC experiments; it can be seen by comparing the area under the curve measurements that the unknown compound with a retention time of 26.2 minutes was produced in higher quantities in all of the enzyme degradations rather than in the Ringers degradations. It was present in the highest quantities in the enzyme degradation of the 0% silica samples; in general the area under the curve decreased as each experiment progressed or though some fluctuations did occur.

**Table 5.8: Peak data obtained from the HPLC analysis of the supernatants of Ringers (R) (week 17//18/19/20) and Tris-proteinase K (TP) (day 3/6/9/13/16) degradation of PLA and PLA-silica scaffolds (single point run)**

| Sample (%silica) | Degradation Experiment | Lactic acid concentration (mM) | | | | Unknown @26.2 minutes Peak Area (AU) | | | | Unknown @ 15.6 minutes Peak Area (AU) |
|---|---|---|---|---|---|---|---|---|---|---|
| | | 17 | 18 | 19 | 20 | 17 | 18 | 19 | 20 | |
| 0 | R | 0 | 0 | 0 | 0 | 4.6 | 6.1 | 6.5 | 4.8 | Not present |
| 9.1 | R | 8.1 | 8.9 | 11.4 | 7.5 | 0.54 | 0.58 | 0.73 | 0.53 | Not present |
| 33.3 | R | 9.2 | 16.7 | 18.3 | 12.3 | 0.44 | 0.60 | 0.47 | 0.75 | Not present |

| Sample (%silica) | Degradation Experiment | Lactic acid concentration (mM) | | | | | Unknown @26.2 minutes Peak Area (AU) | | | | | Unknown @ 15.6 minutes Peak Area (AU) | | | | |
|---|---|---|---|---|---|---|---|---|---|---|---|---|---|---|---|---|
| | | 3 | 6 | 9 | 13 | 16 | 3 | 6 | 9 | 13 | 16 | 3 | 6 | 9 | 13 | 16 |
| 0 | TP | 17.7 | 19.3 | 19.4 | 18.8 | 20.9 | 8.1 | 7.1 | 5.6 | 5.2 | 6.4 | Not measurable | | | | |
| 9.1 | TP | 22.0 | 23.9 | 22.3 | 23.5 | 22.4 | 5.1 | 4.3 | 4.3 | 4.1 | 4.2 | 1.9 | 1.8 | 1.9 | 1.8 | 1.8 |
| 33.3 | TP | 20.3 | 19.4 | 19.3 | 20.1 | 20.3 | 3.8 | 4.3 | 4.1 | 4.5 | 4.0 | 2.0 | 1.9 | 1.9/ | 1.8 | 1.8 |

Figure 5.10 presents the cumulative mass fraction of lactic acid produced through the course of each of the degradation processes.

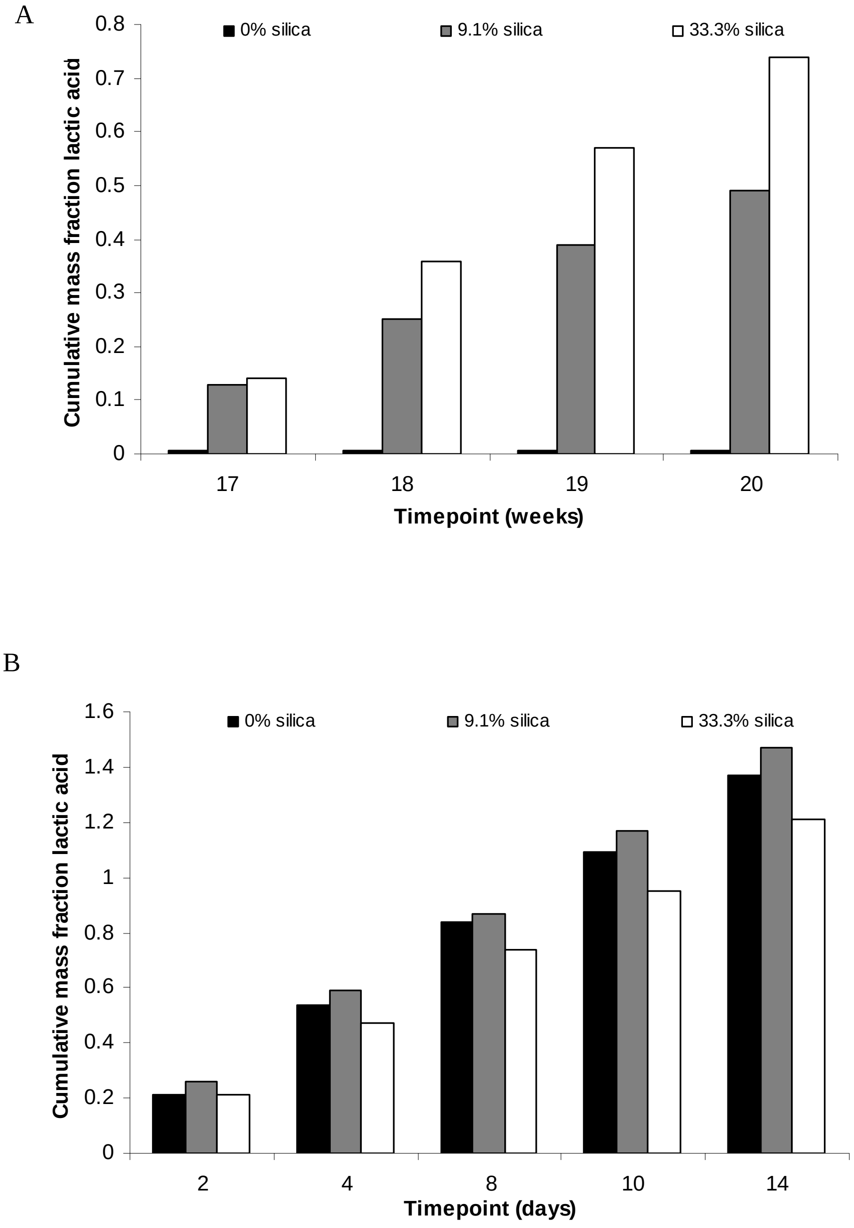

**Figure 5.10: Cumulative mass fraction of lactic acid generated throughout the course of Ringers buffer degradation (A) and Tris-proteinase K degradation (B) as obtained from HPLC analysis (n=1).**

Water absorption is linked to increasing pore size, since as pores enlarge water is more able to penetrate deeper within the scaffold structure, hence an increase in water absorption (as seen throughout all of the time points of the Ringers degradation of PLA scaffolds and in week 17 and 18 with silica content) would indicate enlargement of pores; a decrease (as seen in weeks 19 and 20 with silica content) may be associated with pore collapse or disappearance through erosion as degradation becomes more advanced. Substantial mass loss is really only noticeable in the absence of silica, and it could be that the presence of silica nucleates crystallisation (as discussed in chapter 4), and that crystalline regions of the scaffolds do not degrade by enzyme as quickly as the amorphous regions of the scaffold. The decrease in water absorption as seen with weeks 19 and 20 of scaffolds containing silica could be due to the slight acidity of the silica increasing the local pH which in turn increases the rate of autocatalysis. A similar effect has been noted with acidic catalysts including silica (Brahmkhatri and Patel, 2009).

The 26 minute peak seen during HPLC analysis coincided with the literature retention time typical of isopropanol (propan-1-ol; Rezex company data sheets). Isopropanol could have been generated through the degradation process through random chain scission. It is also possible that a lactate unit was being formed – lactic acid less a proton - as happens to lactic acid in solution, and that this was the peak at 15.5 minutes. The dimer of lactic acid (lactide) is too large a molecule to be eluted from the column in such a short amount of time, since lactide is the cyclic di-ester of lactic acid (2-hydroxypropionic acid). Respective molecular weights: lactic acid : 90; lactate: 89; isopropanol: 60; lactide: 143. The presence of silica in the scaffolds would appear to promote chain end scission and hydrolysis of the ester linkage in addition to the random chain scission, since it is the two former processes that result in the formation of lactic acid.

## 5.3.4 DSC analysis of enzyme degraded samples

DSC was used as a means of assessing molecular weight (through a decrease in Tm), in crystalline order (through a decrease in Tg), and the extent to which the energy associated with these transitions (ΔH) was altered by the degradation process. The methodology has already been described in section 4.2.1.3.

Figure 5.11 shows a DSC thermogram, typical of all of those obtained post enzyme degradation regardless of silica content or point in time; The Tm was present, but the Tg had been almost entirely eradicated. However when compared to a non-degraded sample (section 4.3.1) where measurable, the $T_g$ was seen to have increased from 60.6°C to 68.4°C at the end of the degradation process showing there was more order in the crystal structure

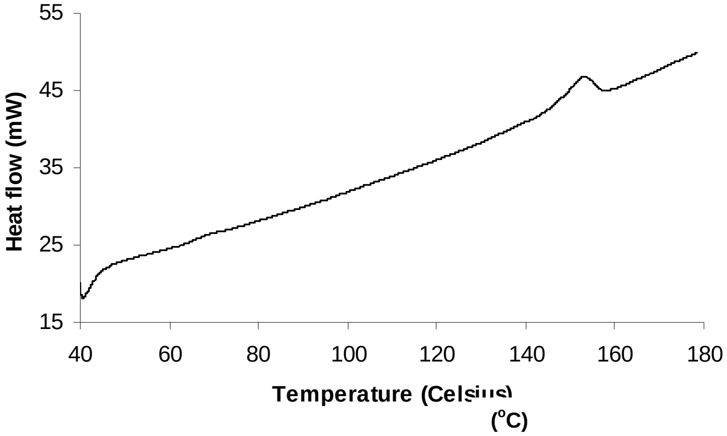

**Figure 5.11: DSC thermogram of PLA post enzyme degradation showing almost total loss of Tg**

As an indicator of molecular weight it was thought that the $T_m$ would be considerably lower post degradation compared to pre degradation, but DSC analysis showed that there was no real change in $T_m$ within the same silica content, it was however noticeably lower in the 33.3% silica compared to the 0% silica samples at day 16. The energy (ΔH) associated with the $T_m$ transition in scaffolds containing 0% and 9.1% silica were fairly consistent although in 33.3% silica scaffolds there was considerable variation in the ΔH of the Tm through the duration of the degradation, as shown in table 5.9

**Table 5.9: Change in** $T_m$ and ΔH **throughout enzyme degradation as evidenced by DSC. There was no obvious difference between like samples but there was a significant difference between 0% and 33.3% samples (Mann-Whitney U test two tails, p=0.05). Errors represent standard deviation from the mean (n=4)**

| % silica content | Day 3 | | Day 9 | | Day 16 | |
|---|---|---|---|---|---|---|
| | $T_m$ | ΔH | $T_m$ | ΔH | $T_m$ | ΔH |
| 0 | 153.2 ± 1.2 | 20.6 ± 1.6 | 153.5 ± 1.1 | 22.0 ± 2.0 | 154.0 ± 1.9 | 21.4 ± 2.7 |
| 9.1 | 153.2 ± 2.1 | 22.3 ± 3.0 | 155.6 ± 0.8 | 23.9 ± 1.3 | 153.5 ± 0.5 | 23.7 ± 0.1 |
| 33.3 | 150.6 ± 1.7 | 17.9 ± 3.0 | 149.9 ± 1.2 | 13.7 ± 2.6 | 149.2 ± 1.4 | 17.0 ± 2.0 |

Comparing pre and post degradation samples, there was very little change in the 0% silica $T_m$, from 146.1°C non-degraded sample to 145.9°C at the end of degradation indicating that there was little change in molecular weight in spite of the mass loss measurements. It is possible that the preferential degradation of amorphous regions of the polymer by the enzyme left behind the crystalline regions and that this compensated for any reduction in molecular weight. The $T_m$ for the 9.1% silica sample was shown to have increased from 148.3°C (non-degraded) to 153.3°C (degraded). In scaffolds containing 33.3% silica $T_m$ also increased, from 147.5°C (non-degraded) to 149.2°C (degraded). The increase in $T_m$ shows that the enzyme preferentially degraded the amorphous regions of the polymer, leaving the crystalline regions untouched which therefore raised the $T_m$ of the remaining polymer.

### 5.3.5 MicroCT

Due to the nature of the very large open pores on the surface of the scaffolds post degradation, the microCT program was unable to interpret the images needed to produce the data that would enable pore size and pore volume distributions to be calculated; therefore, the data obtained from the microCT could only be used to provide visual representation of the degradation process (figure 5.12). All of the scaffolds showed surface erosion by day 3 (left hand column), but the extent to which the enzyme solution had permeated by day 16 (right hand column) varied with increasing silica content. In the sample containing 0% silica, it could be seen that virtually the whole scaffold structure had eroded away to leave a hollow shell, whereas with 9.1% and 33.3% silica contents it could be seen that the degradation was most complete in areas where there were fewer silica particles. However, the transparency of the scaffolds to the passage of X-rays was seen to increase (the scaffolds become very light grey from being dark grey or white) which indicated that the polymer component was becoming less dense as the experiment proceeded.

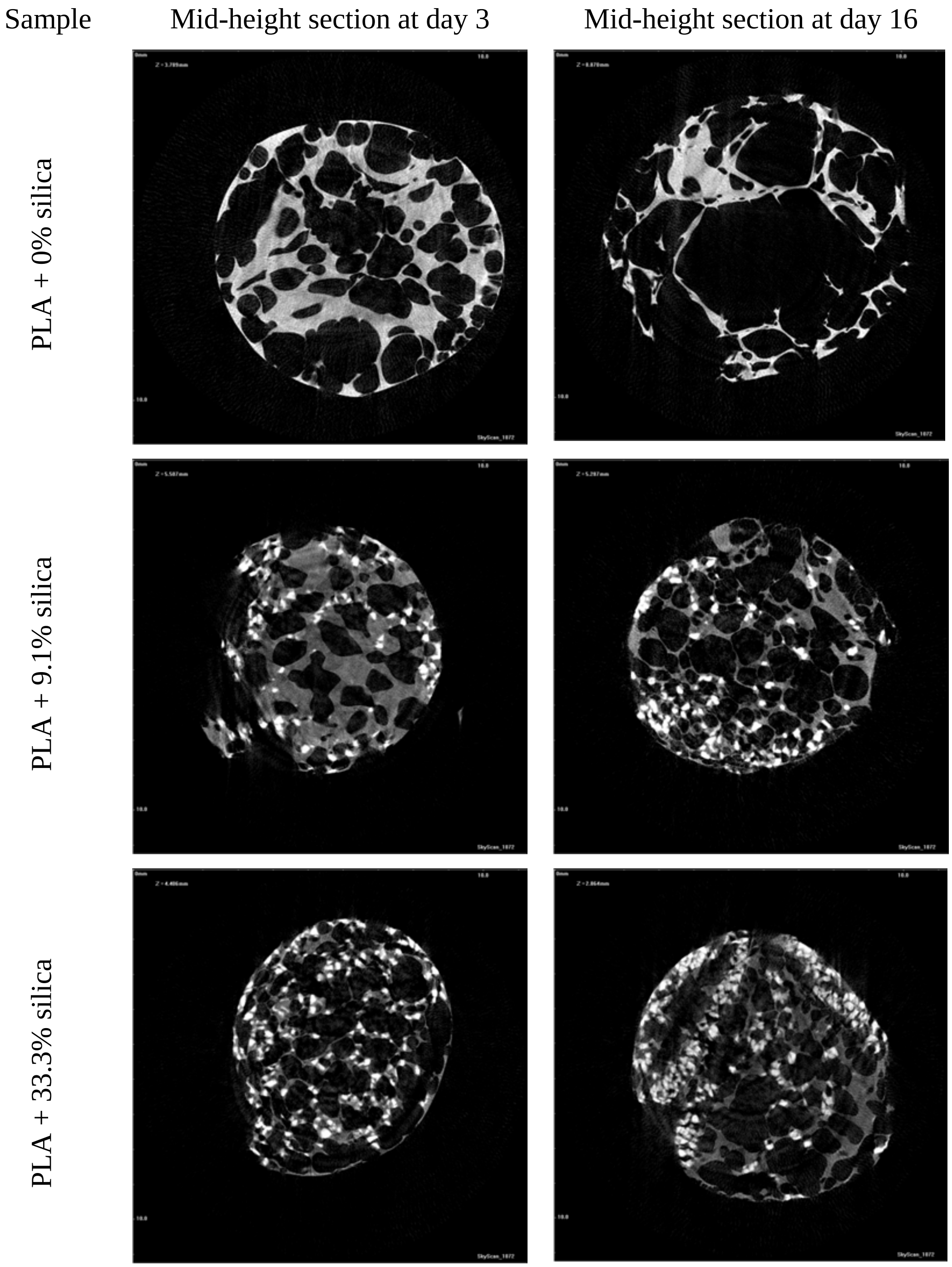

**Figure 5.12: MicroCT images taken throughout the enzyme degradation process.**

## 5.4 Conclusion

In the previous chapters it has been postulated that silica acts to nucleate crystallisation within the polymer scaffolds; the enzyme proteinase k is known to preferentially degrade amorphous polymer and these microCT images support that statement because they show that in the absence of silica where the majority of the polymer is amorphous (as a result of the SCF process) degradation is almost complete, whereas in the presence of silica degradation is limited to the regions of the polymer structure where silica or crystallisation are not present.

The degradation of PLA scaffolds containing silica in Ringers buffer and Tris-proteinase k was monitored through mass loss alongside identification of degradation products by HPLC and through DSC to determine thermal behaviour changes. Literature pertinent to degradation of 3D structures was scarce, therefore where relevant, information obtained from 2d films has been used; in these literature studies, degradation occurred in 48 hours or less, molecular weight was determined by GPC or SEC and the only degradation product monitored was lactic acid evidenced by pH increases and lactate assay (Wang, 2006; Tsuji, 2001, 2004 2006).

It was therefore concluded that in Ringers buffer random chain scission was the probable degradation mechanism, initially resulting in the formation of large chain fragments which corresponded to literature values of isopropanol on analysis by HPLC; subsequent analysis of Ringers buffer alone excluded the presence of the 26 minute peak, and analysis of a 10% isopropanol sample confirmed the literature retention time of 26 minutes. However, the presence of silica in the scaffolds appeared to promote chain end scission as well as random chain scission resulting in the presence of lactic acid. Degradation by enzyme occurred most rapidly in the absence of silica and appeared to be confined to amorphous regions when silica was present; the formation of lactic acid and isopropanol as by-products of the degradation both in the presence and absence of silica suggest chain end scission and random chain scission. In addition the presence of lactate (the hydrolysed monomer of lactide – from the polylactide units of the polymer) suggested that other intermediaries are present and could potentially be detected *in vivo* as a way of monitoring implant breakdown.

The presence of silica was postulated to nucleate crystalline regions within the polymer (as evidenced through DSC and hotstage work in chapter 4) which the enzyme was unable to degrade, and this resulted in an increase in $T_g$ and $T_m$ in pre and post degradation in the DSC analysis. Qualitative confirmation that the scaffolds had been degraded was made through the use of microCT sections taken from images at each time point in the degradation process; calculations pertinent to the pore size distributions could not be made due to shortcomings in the program algorithms which meant that very large open pores could not be accounted for therefore pre and post degradation quantitative comparisons with the results in chapters 2 and 3 could not be made.

# Chapter 6: Summary of Conclusions

The scope of the preceding experimental work was to produce scaffolds suitable for tissue engineering applications through the supercritical fluid gas foaming approach using the polymer Polylactide (PLA) with the inclusion of the mineral silica in order to address two of the issues typical of such scaffolds, namely low connectivity between pores, and the presence of an outer 'skin' - both artifacts from the production process. Characterisation of the scaffold behaviour in experiments that mimicked mineral (bone) deposition and *in vivo* degradation - in a human serum analogue (Ringers solution) and in an enzyme solution that might typically found in a host system (proteinase k) followed. In the course of these experiments data pertaining to the porosity and connectivity of the pores within the scaffolds was collected by physical measurement, SEM, MIP and microCT; the influence of silica on the physical properties (namely crystallinity) and mechanical integrity of the scaffolds was collected by DSC, hotstage microscopy and compression testing; and analysis of the mineral deposition was carried out by von Kossa staining, FTIR and ESEM whilst degradation products were analysed by HPLC.

At the outset it was found that varying the rate at which depressurisation occurred allowed some control over the total porosity of unmodified PLA scaffolds, with slow depressurisation of the vessel at 0.2 L/min resulting in scaffolds with an average porosity of 83.4 ± 1.2%, while a more rapid rate of depressurisation (2.25 L/min) resulted in the formation of PLA scaffolds with an average porosity of 64.6 ± 2.0%. Inclusion of silica resulted in scaffolds that were between 48.8% ± 4.2% porous (0% silica) and 96.1% ± 0.2% porous (33.3% silica) (data obtained from physical measurements). Analysis of these scaffolds by microCT showed them to be between 59% ± 1.0% and 54% ± 2.0%

porous with pores to be in the diameter range of 0.088-0.924 mm in the absence of silica, and 0.044 – 0.342 mm with the inclusion of 33.3% silica respectively, demonstrating that silica was beneficial in control of both pore size and overall scaffold porosity. Visual assessment of the scaffolds by SEM and microCT modelling confirmed this reduction in pore size and also revealed the absence of the outer skin which often blights gas foamed scaffolds It should be borne in mind that the inclusion of silica drastically reduced the height of the scaffolds (due to reduction of the viscosity of the polymer), and that had the scaffold height been constant porosity would have been increased rather than decreased.

The 3D structure of scaffolds is known to play an important role in the success of bone tissue growth. Established methods for assessing pore size and porosity (such as MIP) cannot be used on porous structures such as polymer scaffolds due to the high pressure needed to intrude mercury into the very smallest pores causing collapse of delicate pore walls. MIP gave a perceived porosity of open pores of 35.8% in scaffolds containing 0% silica and 46.8% in scaffolds containing 33.3% silica compared to values of 25% and 60% respectively as obtained by the Archimedes method, (open pores) and 59% and 54% respectively by microCT (open and closed pores). Measurements pertaining to pore wall thickness and connectivity were also obtained from microCT, and the two parameters were found to have an inverse relationship; the presence of silica was found to enhance connectivity of pores.

MicroCT (unlike mercury intrusion porosimetry or SEM) is a non-destructive method which provides quantitative analysis of both closed and open pores in three dimensions. However, more data needs to be collected to optimise the algorithms that calculate the fragmentation index since the nature of the analysis of this parameter is such that it is unable to distinguish between the apparent volume of ‘interconnected’ space between large, isolated pores, and the real interconnectivity afforded by pathways of smaller ones.

The inclusion of silica within the polymer was seen to promote crystal nucleation and growth in solvent cast films and this was evidenced by the data obtained through DSC measurements, namely increases in $\Delta H_f$ (4J/g) $T_g$ ($1^oC$) and crystallinity (3%) but $T_m$ appeared to be unaffected; spherulite nucleation and growth was also observed through hotstage microscopy. However, the SCF process appeared to return all materials to their amorphous form as evidenced by lack of $T_m$ on DSC but this loss of crystallinity was found to be a reversible process that could be restored by an isothermal conditioning process.

The effect that silica had on the mechanical properties of the foamed samples was that the foams exhibited more plastic behaviour than elastic behaviour with increasing silica content. The elastic modulus (strength) was found to increase with increasing silica content (by up to 1.5 mPa), and it was proposed that this was due to silica promoting crystallinity within the foams, and that crystalline regions have a higher elastic modulus than amorphous regions. The load tolerated at yield increased by up to 60N.

The mineralisation process was seen (by SEM and von Kossa stain) to infiltrate the scaffold pores, the mineral confirmed as containing calcium and phosphate. Ringers degradation only produced lactic acid in the presence of silica and the enzyme proteinase k was shown to preferentially degrade amorphous polymer with degradation being almost complete (0%) whereas in the presence of silica degradation was partial (9.1%) or very limited (33.3%). The presence of silica was postulated to nucleate crystalline regions within the polymer (as evidenced previously through DSC and hotstage work which the enzyme was unable to degrade, and this resulted in an increase in $T_g$ and $T_m$ post degradation in the DSC analysis. HPLC analysis of the breakdown products confirmed the presence of lactic acid and isopropanol alongside one other compound, proposed to be lactate, the latter two compounds proposed as being intermediaries in the degradation of PLA to lactic acid.

# Chapter 7: Further work

The scaffolds that have been produced in these gas foaming experiments have huge potential for development. If PLA is the polymer of choice and fulfils the criteria of the desired application then a melt extruder could be used instead of the pressure vessel, which would make the gas foaming process continuous (rather than batch) and would make the scaffolds more uniform; the whole process would then become more energy efficient and could then be scaled up for industrial production.

If another polymer or co-polymer (such as PLGA or PCA) was to be used with lower melt temperatures, the possibility exists that biologically active compounds could be incorporated within the scaffolds with the potential that they could be used as a drug delivery device.

Use of different grain sizes of silica or even other nucleating agents or foaming agents such as nitrogen ($N_2$) could be explored to further tailor the range of pore sizes or pore architecture to the desired application of the scaffolds.

Once scaffold production had been optimised and standardised another line of investigation would be to carry out perfusion culture of an osteoblast cell line (such as MC-3T3) using the scaffolds as the basis for a tissue engineered implant. Perfusion culture would be more preferable to static culture, since the media the scaffolds are bathed in is in a dynamic system making it more like an *in vivo* host; it also subjects the cells to low levels of strain, essential for them to become mineralised. An *in vivo* study would be the next logical progression.

# References

Agrawal, C.M., Best, J., Heckman, J.D., Boyan, B.D. 1995. Protein release kinetics of a biodegradable implant for fracture non-unions. *Biomaterials*, 16, (16) 1255-1260

Alexis, F., Venkatraman, S., S., Rath, S., K., Boey, F. 2004. In vitro study of release mechanisms of paclitaxel and rapamycin from drug-incorporated biodegradable stent matrices. *Journal of controlled release*, 98, (1) 67-74

Atwood, R.C., Jones, J.R., Lee, P.D., & Hench, L.L. 2004. Analysis of pore interconnectivity in bioactive glass foams using X-ray microtomography. *Scripta Materialia*, 51, (11) 1029-1033

Bancroft, G.N., Sikavitsas, V.I., van den, D.J., Sheffield, T.L., Ambrose, C.G., Jansen, J.A., & Mikos, A.G. 2002. Fluid flow increases mineralized matrix deposition in 3D perfusion culture of marrow stromal osteoblasts in a dose-dependent manner. *Proceedings of the National Academy of Sciences U.S.A*, 99, (20) 12600-12605

Barry, J.J., Silva, M.M., Popov, V.K., Shakesheff, K.M., & Howdle, S.M. 2006. Supercritical carbon dioxide: putting the fizz into biomaterials. *Philosophical Transactions A: Maths, Physics, Engineering Sciences*, 364 (1838) 249-261

Bershtein, V.A. and Egorov, V.M. (1994). Differential scanning calorimetry of polymers: Physics, Chemistry, Analysis, Technology. New York: Ellis Horwood Ltd.

Bigg, D.M. 1996. Effect of copolymer ratio on the crystallinity and properties of polylactic acid copolymers. *Antec '96: Plastics - Racing into the Future, Vols I-Iii - Vol I: Processing; Vol II: Materials; Vol III: Spacial Areas.* Society of Plastics Engineers Technical Papers. 54th Annual Technical Conference of the Society-of-Plastics-Engineers - Plastics: Racing into the Future (ANTEC 96) May 05-10, 1996. Indianapolis, In, 42 2028-2039

Boccaccini, A.R., Maquet, V. 2003. Bioresorbable and bioactive polymer/Bioglass (R) composites with tailored pore structure for tissue engineering applications. *Composites Science and Technology*, 63, (16) 2417-2429

Boyle, W.J., Simonet, W.S., Lacey, D.L. 2003. Osteoclast differentiation and activation. *Nature*, 423, (6937) 337-342

Brauer, D.S., Russel, C., Li, W., Habelitz, S. 2006. Effect of degradation rates of resorbable phosphate invert glasses on in vitro osteoblast proliferation. *Journal of Biomedical Materials Research Part A*, 77A, (2) 213-219

Cancedda, R., Cedola, A., Giuliani, A., Komlev, V., Lagomarsino, S., Mastrogiacomo, M., Peyrin, F., & Rustichelli, F. 2007. Bulk and interface investigations of scaffolds and tissue engineered bone by X-ray microtomography and X-ray microdiffraction. *Biomaterials*, 28, 2505-2524

Chao, C.C., Chen, C.K., Chiang, Y.W., & Ho, R.M. 2008. Banded Spherulites in PS & PLLA Chiral Block Copolymers. *Macromolecules*, 41, (11) 3949-3956

Chen, Q.Z., Rezwan, K., Armitage, D., Nazhat, S.N., & Boccaccini, A.R. 2006. The surface functionalization of 45S5 Bioglass-based glass-ceramic scaffolds and its impact on bioactivity. *Journal of Materials Science Materials in Medicine.*, 17, (11) 979-987

Chen, Q. Z., Quinn, J. M.W., Thouas, G. A. Zhou, X.,. Komesaroff, P. A. (2010). Bone-Like Elastomer-Toughened Scaffolds with Degradability Kinetics Matching Healing Rates of Injured Bone. *Advanced Engineering Materials.* (12), 11, B642-B648

Cordonnier, T., Sohier, J., Rosset, P., and Layrolle, P. (2011) Biomimetic Materials for Bone Tissue Engineering – State of the Art and Future Trends. *Advanced Engineering Materials,* (13), 5

Cromme, P., Zollfrank, C., Muller, L., Muller, F.A., & Greil, P. 2007. Biomimetic mineralisation of apatites on Ca2+ activated cellulose templates. *Materials Science and Engineering C*, 27, (1) 1-7

Cyster, L.A., Grant, D.M., Howdle, S.M., Rose, F.R., Irvine, D.J., Freeman, D., Scotchford, C.A., & Shakesheff, K.M. 2005. The influence of dispersant concentration on the pore morphology of hydroxyapatite ceramics for bone tissue engineering. *Biomaterials*, 26, (7) 697-702

Dees, P.J., Polderman, J. 1981. Mercury porosimetry in pharmaceutical technology. *Powder Technology*, 29, (1) 187-197

Deng, X., M., Guo, L., K., Liu, Y., Hao, J., Y. 2003. The degradation of PL-CLE in different pH values and accelerated degradation by increasing temperature or performing in 6% $H_2O_2$-PBS. *Journal of polymer materials*, 20, (3) 285-391

Dorgan, J.R., Lehermeier, H., & Mang, M. 2000. Thermal and rheological properties of commercial-grade poly(lactic acid)s. *Journal of Polymers and the Environment*, 8, (1) 1-9

Doroudiani, S., Park, C.B., Kortschot, M.T. 1996. Effect of the crystallinity and morphology on the microcellular foamstructure of semicrystalline polymers. *Polymer Engineering and Science,* 36, (21) 2645-2662

dos Santos, E.A., Farina, M., & Soares, G.A. 2007. Specific proliferation rates of human osteoblasts on calcium phosphate surfaces with variable concentrations of [alpha]-TCP. *Materials Science and Engineering: C*, 27, (1) 61-66

Drieskens, M., Peeters, R., Mullens, J., Franco, D., Lemstra, P.J., Hristova-Bogaerds, D.G. 2009. Structure Versus Properties Relationship of Poly(lactic acid). I.Effect of Crystallinity on Barrier Properties. *Journal of Polymer Science Part B-Polymer Physics*, 47, (22) 2247-2258

Drumright, R.E., Gruber, P.R., & Henton, D.E. 2000. Polylactic acid technology. *Advanced Materials*, 12, (23) 1841-1846

Du, C., Meijer, G.J., van, d., V, Haan, R.E., Bezemer, J.M., Hesseling, S.C., Cui, F.Z., de, G.K., & Layrolle, P. 2002. Bone growth in biomimetic apatite coated porous Polyactive 1000PEGT70PBT30 implants. *Biomaterials*, 23, (23) 4649-4656

Duarte, A.R.C., Caridade, S.G., Mano, J.F., Reis, R.L., Rui L. 2009. Processing of novel bioactive polymeric matrixes for tissue engineering using supercritical fluid technology. *Materials Science & Engineering C-Materials for Biological Applications*, 29, (7) 2110-2115

Dunne, M., Corrigan, O.I., Ramtoola, Z. 2000. Influence of particle size and dissolution conditions on the degradation properties of polylactide-co-glycolide particles. *Biomaterials*, 21, (16) 1659-1668

Frank, A., Rath, S.K., Boey, F.,Venkatraman, S. 2004. Study of the initial stages of drug release from a degradable matrix of poly(d,l-lactide-co-glycolide). *Biomaterials*, 25, (5) 813-821

Freed LE & Vunjak-Novakovic G 1998. Culture of organised cell communities. *Advanced Drug Delivery Reviews*, 33, 15-30

Fukuda, N., Tsuji, H., Ohnishi, Y. 2002. Physical properties and enzymatic hydrolysis of poly(L-lactide)-$CaCO_3$ composites. *Polymer degradation and stability*, 78 (1) 119-127

Funhoff, A.M., van Nostrum, C.F., Janssen, A.P., Fens, M.H., Crommelin, D.J., Hennink, W.E. 2004. Polymer side-chain degradation as a tool to control the destabilization of polyplexes. *Pharmaceutical* Research, 21, (1) 170-176

Gan, Z.H., Yu, D.H., Zhong, Z.Y., Liang, Q.Z., Jing, X.B. 1999. Enzymatic degradation of poly(epsilon-caprolactone)/poly(DL-lactide) blends in phosphate buffer solution. *Polymer*, 40, (10) 2859-2862

Garlotta, D. 2001. A literature review of poly(lactic acid). *Journal of Polymers and the Environment*, 9, (2) 63-84

Gauthier, O., Bouler, J.M., Aguado, E., Pilet, P., & Daculsi, G. 1998. Macroporous biphasic calcium phosphate ceramics: influence of macropore diameter and macroporosity percentage on bone ingrowth. *Biomaterials*, 19, (1-3) 133-139

Gbureck, U., Barralet, J.E., Spatz, K., Grover, L.M., & Thull, R. 2004. Ionic modification of calcium phosphate cement viscosity. Part I: hypodermic injection and strength improvement of apatite cement. *Biomaterials*, 25, (11) 2187-2195

Ginty, F., Prynnne, C.J., Muniz-Terrera, G., Mishra, G.D., Prentice, A., O'Connell, M.A. 2005. No evidence for a negative association between bone mineral status and indirect estimates of renal net acid excretion in adolescents. *Proceedings of the Nutrition Society*, 64, Suppl. S 80A

Glicklis, R. 2000. Hepatocyte Behavior Within Three-Dimensional Porous Alginate Scaffolds. *Biotechnology and Bioengineering*, 67, 344-353

Gopferich, A. 1997. Polymer bulk erosion. *Macromolecules* 30, (9) 2598-2604

Gratson, G.M., Xu, M.J., Lewis, J.A. 2004. Microperiodic structures - Direct writing of three-dimensional webs. *Nature*, 428, (6981) 386

Griffith, L.G. 2000. Polymeric biomaterials. *Acta Materialia*, 48, (1) 263-277

Gualandi, C., Wilczek, P., Focarete, M.L., Pasquinelli, G., Kawalec, M., Scandola, M. 2009. Bioresorbable electrospun nanofibrous scaffolds loaded with bioactive molecules. *E-Polymers*, 060

Harris, L.D., Kim, B.S., & Mooney, D.J. 1998. Open pore biodegradable matrices formed with gas foaming. *Journal of Biomedical Materials Research*, 42, (3) 396-402

Hench, L.L. 1980. Biomaterials. *Science*, 208, (4446) 826-831

Hench, L.L. & Paschall, H.A. 1973. Direct chemical bond of bioactive glass-ceramic materials to bone and muscle. *Journal of Biomedical Materials Research*, 7, (3) 25-42

Hildebrand T & Ruegsegger, P. 1997. A new method for the model independent assessment of thickness in three-dimensional images. *Journal of microscopy*, 185, 67-75

Hildebrand, T. & Ruegsegger, P. 1997. Quantification of Bone Microarchitecture with the Structure Model Index. *Computational Methods in Biomechanical and Biomedical Engineering*, 1, (1) 15-23

Hildebrand, T., Laib, A., Muller, R., Dequeker, J., & Ruegsegger, P. 1999. Direct three-dimensional morphometric analysis of human cancellous bone: microstructural data from spine, femur, iliac crest, and calcaneus. *Journal of Bone Mineralogy Research*, 14, (7) 1167-1174

Hile, D.D., Amirpour, M.L., Akgerman, A., & Pishko, M.V. 2000. Active growth factor delivery from poly(,-lactide-co-glycolide) foams prepared in supercritical CO2. *Journal of Controlled Release*, 66, (2-3) 177-185

Howdle, S. M. 2001. Supercritical fluid mixing: preparation of thermally sensitive polymer composites containing bioactive materials. *Chemical Communications* (1) 109-110

Howdle, S.M., Watson, M.S., Whitaker, M.J., Popov, V.K., Davies, M.C., Mandel, F.S., Wang, J.D., Shakesheff, K.M. 2001. Supercritical fluid mixing: preparation of thermally sensitive polymer composites containing bioactive materials. *Chemical Communications*, 01, 109-110

Hubbell, J.A. 1999. Bioactive biomaterials. *Current Opinions in Biotechnology*, 10, (2) 123-129 available from: PM:10209141

Hutmacher, D.W. 2000. Scaffolds in tissue engineering bone and cartilage. *Biomaterials*, 21, (24) 2529-2543

Iwata, T., Doi, Y. 1998. Morphology and enzymatic degradation of poly(L-lactic acid) single crystals. *Macromolecules*, 31, (8) 2461-2467

Jain, R.A., Rhodes, C.T., Railkar, A.M., Malick, A.W., Shah, N.H. 2000. Comparison of various injectable protein-loaded biodegradable poly(lactide-co-glycolide) (PLGA) devices: In-situ-formed implant versus in-situ-formed microspheres versus isolated microspheres. *Pharmaceutical Development and Technology*, 5, (2) 201-207

Jayasuriya, A.C., Assad, M., Jayatissa, A.H., Ebraheim, N.A. 2006. Dissolution behaviour of biomimetic minerals on 3D PLGA scaffold. *Surface & Coatings Technology*, Symposium on Protective Coatings and Thin Films held at the E-MRS Spring Meeting, May 31, 2004-June 03, 2005 Strasbourg, France. 200, (22-23) 6336-6339

Jenkins, M.J., Harrison, K.L., Silva, M.M.C.G., Whitaker, M.J., Shakesheff, K.M., & Howdle, S.M. 2006. Characterisation of microcellular foams produced from semi-crystalline PCL using supercritical carbon dioxide. *European Polymer Journal*, 42, (11) 3145-3151

Kellomaki, M., Niiranen, H., Puumanen, K., Ashammakhi, N., Waris, T., & Tormala, P. 2000. Bioabsorbable scaffolds for guided bone regeneration and generation. *Biomaterials*, 21, (24) 2495-2505

Khosla, S. 2001.Minireview: The OPG/RANKL/RANK system. *Endocrinology*, 142, (12) 5050-5055

Kitsugi, T., Yamamuro, T., Nakamura, T., Kokubo, T., Takagi, M., Shibuya, T., Takeuchi, H., Ono, M. 1987. Bonding behavior between 2 bioactive ceramics in-vivo. *Journal of Biomedical Materials Research*, 21, (9) 1109-1123

Kitsugi, T., Yamamuro, T., Nakamura, T., Kokubo, T. 1989. The bonding of glass-ceramics to bone. *International Orthopaedics*, 13, (3) 199-206

Kolstad, J.J. 1996. Crystallization kinetics of poly(L-lactide-co-meso-lactide). *Journal of Applied Polymer Science*, 62, (7) 1079-1091

Kokubo, T., Kushitani, H., Sakka, S., Kitsugi, T., & Yamamuro, T. 1990. Solutions able to reproduce in vivo surface-structure changes in bioactive glass-ceramic A-W. *Journal of Biomedical.Materials Research*, 24, (6) 721-734

Kronenberg, H.M. 2003. Developmental regulation of the growth plate. *Nature*, 423 (6937) 332-336

Kulkarni, A., Reiche, J., Lendlein, A. 2007. Hydrolytic degradation of poly(rac-lactide) and poly[(rac-lactide)-co-glycolide] at the air-water interface. *Surface and Interface Analysis*, 39, (9) 740-746

Landry, F.B., Bazile, D.V., Spenlehauer, G., Veillard, M., Kreuter, J. 1996. Degradation of poly(D,L-lactic acid) nanoparticles coated with albumin in model digestive fluids (USP XXII). *Biomaterials*, 17, (7) 715-723

Langer Robert & Vacanti Joseph P. 1993. Tissue engineering. *Science*, 260, (920) 926

Leblond, C.P., Wright, G.M. 1981. Steps in the elaboration of collagen by odontoblasts and osteoblasts. *Methods in Cell Biology*, 23, 167-189

Lee, P.C., Wang, J., Park, C.B. 2006. Extruded open-cell foams using two semicrystalline polymers with different crystallization temperatures. *Industrial and Engineering Chemistry Research*, 45, (1) 175-181

Li, S.M., Garreau, H., Vert, M. 1990. Structure property relationships in the case of the degradation of massive aliphatic poly-(alpha-hydroxy acids) in aqueous-media .1.poly(dl-lactic acid). *Journal of Materials Science-Materials in Medicine*, 1, (3) 123-130

Li, S.M., Garreau, H., Vert, M. 1990. Structure-property relationships in the case of the degradation of massive poly(alpha-hydroxy acids) in aqueous-media. III. Influence of the morphology of poly(l-lactic acid). *Journal of Materials Science-Materials in Medicine*, 1, (4) 198-206

Li, S.M., McCarthy, S. 1999. Influence of crystallinity and stereochemistry on the enzymatic degradation of poly(lactide)s. *Macromolecules*, 32, (13) 4454-4456

Lin, A.S.P., Barrows, T.H., Cartmell, S.H., & Guldberg, R.E. 2003. Microarchitectural and mechanical characterization of oriented porous polymer scaffolds. *Biomaterials*, 24, (3) 481-489

Lu, P.Z., Lannutti, J.J., Klobes, P., Meyer, K. 2000. X-ray computed tomography and mercury porosimetry for evaluation of density evolution and porosity distribution. *Journal of the American Ceramic Society*, 83, (3) 518-522

Lyu, S., Sparer, R., Untereker, D. 2005. Analytical solutions to mathematical models of the surface and bulk erosion of solid polymers. *Journal of Polymer Science Part B - Polymer Physics*, 43, (4) 383-397

Lyu, S.P., Schley, J., Loy, B., Lind, D., Hobot, C., Sparer, R., Untereker, D. 2007. Kinetics and time-temperature equivalence of polymer degradation. *Biomacromolecules*, 8, (7) 2301-2310

MacArthur B.D. & Oreffo R.O.C. 2006. Bridging the gap. *Nature*, 433, 19

Mandal, B.B. & Kundu, S.C. 2010. Biospinning by silkworms: silk fiber matrices for tissue engineering applications. *Acta Biomaterialia,* 6, (2) 360-371

Marler, J.J., Upton, J., Langer, R., & Vacanti, J.P. 1998. Transplantation of cells in matrices for tissue regeneration. *Advanced Drug Delivery Reviews,* 33, (1-2) 165-182

Matzinos, P., Tserki, V., Kontoyiannis, A., & Panayiotou, C. 2002. Processing and characterization of starch/polycaprolactone products. *Polymer Degradation and Stability,* 77, (1) 17-24

Middleton, J.C. & Tipton, A.J. 2000. Synthetic biodegradable polymers as orthopedic devices. *Biomaterials,* 21, (23) 2335-2346

Mikos, A.G., Sarakinos, G., Lyman, M.D., Ingber, D.E., Vacanti, J.P., & Langer, R. 1993. Prevascularization of porous biodegradable polymers. *Biotechnology and Bioengineering*, 42, (6) 716-723

Mooney, D.J., Baldwin, D.F., Suh, N.P., Vacanti, J.P., & Langer, R. 1996. Novel approach to fabricate porous sponges of poly(-lactic-co-glycolic acid) without the use of organic solvents. *Biomaterials,* 17, (14) 1417-1422

Murphy, W.L., Dennis, R.G., Kileny, J.L., Mooney, D.J. 2002. Salt fusion: An approach to improve pore interconnectivity within tissue engineering scaffolds. *Tissue Engineering,* 8, (1) 43-52

Nalawade, S.P., Picchioni, F., Janssen, L.P. 2006(a). Supercritical carbon dioxide as a green solvent for processing polymer melts: Processing aspects and applications. *Progress in Polymer Science*, 31, (1) 19-43

Nalawade, S.P., Picchioni, F., Marsman, J.H., Janssen, L.P. 2006(b). The FT-IR studies of the interactions of $CO_2$ and polymers having different chain groups. *Journal of Supercritical Fluids*, 36, (3) 236-244

Nazhat, S.N., Kellomaki, M., Tormala, P.,Tanner, K.E., Bonfield, W. 2001. Dynamic mechanical characterization of biodegradable composites of hydroxyapatite and polylactides. *Journal of Biomedical Materials Research*, 58, (4) 335-343

Oliveira, N. S., Dorgan, J., Coutinho, J., A., P., Ferreira, A., Daridon, J., L., Marrucho, I., M. 2006. Gas solubility of carbon dioxide in poly(lactic acid) at high pressures. *Journal of polymer science part B – polymer physics*, 44, (6) 1010-1-19

Otsuki, B., Takemoto, M., Fujibayashi, S., Neo, M., Kokubo, T., & Nakamura, T. 2006. Pore throat size and connectivity determine bone and tissue ingrowth into porous implants: three-dimensional micro-CT based structural analyses of porous bioactive titanium implants. *Biomaterials*, 27, (35) 5892-5900

Palmer, H.K., Rowe, R.C. 1974. Application of mercury porosimetry to porous polymer powders. *Powder Technology*, 9, (4) 181-186

Patel, P.A., Eckart, J., Advincula, M.C., Goldberg, A.J., Mather, P.T. 2009. Rapid synthesis of polymer-silica hybrid nanofibers by biomimetic mineralization. *Polymer*, 50, (5) 1214-1222

Patience, C., Takeuchi, Y., Weiss, R.A. 1997. Infection of human cells by an endogenous retrovirus of pigs. *Nature Medicine*, 3, (3) 282-286

Peppas, N.A. & Langer, R. 1994. New challenges in biomaterials. *Science*, 263, (5154) 1715-1720

Pitt, C.G., Chasalow, F.I., Hibionada, Y.M., Klimas, D.M., Schindler, A. 1981. Aliphatic polyesters .1. The degradation of poly(epsilon-caprolactone) *in vivo*. *Journal of Applied Polymer Science*, 26, (11) 3779-3787

Pitt, C.G., Gratzl, M.M., Kimmel, G.L., Surles, J., Schindler, A. 1981. Aliphatic polyesters .2. The degradation of poly(dl-lactide), poly(epsilon-caprolactone), and their copolymers in-vivo. *Biomaterials*, 2, (4) 215-220

Pluta, M., Galeski, A. 2002. Crystalline and supermolecular structure of polylactide in relation to the crystallization method. *Journal of Applied Polymer Science*, 86, (6) 1386-1395

Pluta, M., Galeski, A., Alexandre, M., Paul, M.A., Dubois, P. 2002. Polylactide/montmorillonite nanocomposites and microcomposites prepared by melt blending: Structure and some physical properties. *Journal of Applied Polymer Science*, 86, (6) 1497-1506

Powell and Ingen House, 1991; Engineering with polymers, Stanley Thornes, Cheltenham.

Pyda, M., Bopp, R.C., Wunderlich, B. 2004. Heat capacity of poly(lactic acid). *Journal of Chemical Thermodynamics*, 36, (9) 731-742

Qiu, Z.B., Yan, C.Z., Lu, J.M., Yang, W.T. 2007. Miscible crystalline/crystalline polymer blends of poly(vinylidene fluoride) and poly(butylene succinate-co-butylene adipate): Spherulitic morphologies and crystallization kinetics. *Macromolecules*, 40, (14) 5047-5053

Quirk, R.A., France, R.M., Shakesheff, K.M., & Howdle, S.M. 2004. Supercritical fluid technologies and tissue engineering scaffolds. *Current Opinion in Solid State and Materials Science*, 8, (3-4) 313-321

Rack, H.J., & Qazi, J.I. 2006. Titanium alloys for biomedical applications. *Materials science and engineering C*, 26, 1269-1277

Ramesh, N.S., Rasmussen, D.H., Campbell, G.A. 1994. The heterogeneous nucleation of microcellular foams assisted by the survival of microvoids in polymers containing low glass-transition particles .1. Mathematical-modeling and numerical-simulation. *Polymer Engineering and Science*, 34, (22) 1685-1697

Ramesh, N.S., Rasmussen, D.H., Campbell, G.A. 1994. The heterogeneous nucleation of microcellular foams assisted by the survival of microvoids in polymers containing low glass-transition particles .2. Experimental results and discussion. *Polymer Engineering and Science*, 34, (22) 1698-1706

Rekow, D., Van Thompson, P., Ricci, J.L. 2005. Influence of scaffold meso-scale features on bone tissue response. *Journal of Materials Science* 6th International Workshop on Interfaces, June 26-30, 41, (16) 5113-5121

Rigby, S.P., Fletcher, R.S., Raistrick, J.H., Riley, S.N. 2002. Characterisation of porous solids using a synergistic combination of nitrogen sorption, mercury porosimetry, electron microscopy and micro-focus X-ray imaging techniques. *Physical Chemistry Chemical Physics,* 4, (14) 3467-3481

Roy, I., Gupta, MN. 2003. Smart polymeric materials: Emerging biochemical applications. *Chemistry and Biology*, 10, (12) 1161-1171

Sachlos, E., Reis, N., Ainsley, C., Derby, B., & Czernuszka, J.T. 2003. Novel collagen scaffolds with predefined internal morphology made by solid freeform fabrication. *Biomaterials*, 24, (8) 1487-1497

Saha, S.K., Tsuji, H. 2006. Effects of rapid crystallization on hydrolytic degradation and mechanical properties of poly(L-lactide-co-epsilon-caprolactone). *Reactive & Functional Polymers*, 66, (11) 1362-1372

Salter, D. M., Wright, M. O., Caldwell, H., Wallace, H., Robb, J. E. 1997. Response of human bone cells to mechanical stimuli: Different electrophysiological responses with different frequencies of cyclical strain. *Journal of pathology* 181, A11

Sandor, G.K.B., Rittenberg, B.N., Clokie, C.M.L., & Caminiti, M.F. 2003. Clinical success in harvesting autogenous bone using a minimally invasive trephine. *Journal of Oral and Maxillofacial Surgery*, 61, (2) 164-168

Shafi, M.A., Flumerfelt, R.W. 1997. Initial bubble growth in polymer foam processes. *Chemical Engineering Science*, 52, (4) 627-633

Shafi, M.A., Joshi, K., Flumerfelt, R.W. 1997. Bubble size distributions in freely expanded polymer foams. *Chemical Engineering Science*, 52, (4) 635-644

Shah, V.M., Hardy, B.J., Stern, S.A. 1993. Solubility of carbon-dioxide, methane, and propane in silicone polymers - effect of polymer backbone chains. *Journal of Polymer Science Part B-Polymer Physics*, 31, (3) 313-317

Sikavitsas, V.I., Temenoff, J.S., & Mikos, A.G. 2001. Biomaterials and bone mechanotransduction. *Biomaterials*, 22, (19) 2581-2593

Silva, M.M., Cyster, L.A., Barry, J.J.A., Yang, X.B., Oreffo, R.O.C., Grant, D.M., Scotchford, C.A., Howdle, S.M., Shakesheff, K.M., & Rose, F.R.A.J. 2006. The effect of anisotropic architecture on cell and tissue infiltration into tissue engineering scaffolds. *Biomaterials*, 27, (35) 5909-5917

Sousa, A., Schut, J., Kohn, J., Libera, M. 2006. Nanoscale morphological changes during hydrolytic degradation and erosion of a bioresorbable polymer. *Macromolecules*, 39, (21) 7306-7312

Spowage, A.C., Shacklock, A.P., Malcolm, A.A., May, S.L., Tong, L., & Kennedy, A.R. 2006. Development of characterisation methodologies for macroporous materials. *Journal of Porous Materials*, 13, (3-4) 431-438

Tai, H., Upton, C. E., White, L. J., Pini, R., Storti, G., Mazzotti, M., Shakesheff, K. M., Howdle, S. M.. (2010). Studies on the interactions of CO2 with biodegradable poly(DL-lactic acid) and poly(lactic acid-co-glycolic acid) copolymers using high pressure ATR-IR and high pressure rheology. *Polymer,* 51 (1425–1431)

Tancret, F., Bouler, J.M., Chamousset, J., Minois, L.M. 2006. Modelling the mechanical properties of microporous and macroporous biphasic calcium phosphate bioceramics. *Journal of the European Ceramic Society*, 26, (16) 3647-3656

Tatibouet, J., Gendron, R., Hamel, A., Sahnoune, A. 2002. Effect of different nucleating agents on the degassing conditions as measured by ultrasonic sensors. *Journal of Cellular Plastics*, 59th Annual Technical Conference of the Society-of-Plastics-Engineers (ANTEC 01) May 06-10, 2001 Dallas, Texas. 38, (3) 203-218

Tian, H.Y., Tagaya, H. 2007. Preparation, characterization and mechanical properties of the polylactide/perlite and the polylactide/montmorillonite composites. *Journal of Materials Science*, 42, (9) 3244-3250

Tomasko, D.L., Li, H.B., Liu, D.H., Han, X., Wingert, M.J., Lee, L., Koelling, K.W. 2003. A review of $CO_2$ applications in the processing of polymers. *Industrial and Engineering Chemistry Research*, 42, (25) 6431-6456

Tsuji, H., Ikada, Y. 1998. Blends of aliphatic polyesters .II. Hydrolysis of solution-cast blends from poly(L-lactide) and poly(epsilon-caprolactone) in phosphate-buffered solution. *Journal of applied polymer science*, 67, (3) 405-415

Tsuji, H., Mizuno, A., Ikada, Y. 1998. Blends of aliphatic polyesters. III. Biodegradation of solution-cast blends from poly(L-lactide) and poly(epsilon-caprolactone). *Journal of applied polymer science*, 70, (11) 2259-2268

Tsuji, H., Ishizaka, T. 2001. Blends of aliphatic polyesters. VI. Lipase-catalyzed hydrolysis and visualized phase structure of biodegradable blends from poly(epsilon-caprolactone) and poly(L-lactide). *International Journal of Biological Macromolecules*, 29, (2) 83-89

Tsuji, H., Fukui, I. 2003. Enhanced thermal stability of poly(lactide)s in the melt by enantiomeric polymer blending. *Polymer*, 44, (10) 2891-2896

Tsuji, H. 2003. In vitro hydrolysis of blends from enantiomeric poly(lactide)s. Part 4: well-homo-crystallized blend and nonblended films. *Biomaterials*, 24, (4) 537-547

Tsuji, H., Ikarashi, K., Fukuda, N. 2004. Poly(L-lactide): XII. Formation, growth, and morphology of crystalline residues as extended-chain crystallites through hydrolysis of poly(L-lactide) films in phosphate-buffered solution. *Polymer Degradation and Stability*, 84, (3) 515-523

Urist, M.R., O'Connor, B.T., Burwell, R.G. 1990. Bone-grafts, derivatives and substitutes – introduction. *Bone Grafts, Derivatives and Substitutes*: Symposium on Bone Grafts, Derivatives and Substitutes, March 1990. Robert Jones & Agnes Hunt Orthopaedic Hospital, Institute of Orthopaedics, Oswestry, England

Vadiraj A & Kamaraj M 2007. Effect of surface treatments on fretting failure damage of biomedical titanium alloys. *Tribology International*, 40, 82-88

Vallet-Regi, M. & Ramila, A. 2000. New Bioactive Glass and Changes in Porosity during the Growth of a Carbonate Hydroxyapatite Layer on Glass Surfaces. *Chemistry of Materials*, 12, (4) 961-965

Vallet-Regi, M., Perez-Pariente, J., Izquierdo-Barba, I., & Salinas, A.J. 2000. Compositional Variations in the Calcium Phosphate Layer Growth on Gel Glasses Soaked in a Simulated Body Fluid. *Chemistry of Materials*, 12, (12) 3770-3775

von Burkersroda, F., Gref, R., Gopferich, A. 1998. Erosion of biodegradable block copolymers made of poly(D,L-lactic acid) and poly(ethylene glycol). *Biomaterials*, 18, (24) 1599-1607

von Burkersroda, F., Schedl, L., Gopferich, A. 2002. Why degradable polymers undergo surface erosion or bulk erosion. *Biomaterials*, 23, (21) 4221-4231

Whang, K., Thomas, C.H., Healy, K.E., & Nuber, G. 1995. A novel method to fabricate bioabsorbable scaffolds. *Polymer*, 36, (4) 837-842

Yan, X., Huang, X., Yu, C., Deng, H., Wang, Y., Zhang, Z., Qiao, S., Lu, G., & Zhao, D. (2006). The *in-vitro* bioactivity of mesoporous bioactive glasses. *Biomaterials*, 27, (18) 3396-3403

Yan, S., Yin, J., Yang, Y., Dai, Z., Ma, J., Chen, X. (2007). Surface-grafted silica linked with L-lactic acid oligomer: A novel nanofiller to improve the performance of biodegradable poly (L-lactide). *Polymer* (48) 1688-1694.

Yang St & Ng R 2007. A new dimension to biomaterials. *Materials today*, 10, (3) 64

Yokohara, T., Yamaguchi, M. 2008. Structure and properties for biomass-based polyester blends of PLA and PBS. *European Polymer Journal*, 44, (3) 677-685

Young and Lovell, 1998; Introduction to polymers, 2nd edition, Chapman and Hall, London

Yuryev, Y., Wood-Adams, P., Heuzey, M.C., Dubois, C., & Brisson, J. 2008. Crystallization of polylactide films: An atomic force microscopy study of the effects of temperature and blending. *Polymer*, 49, (9) 2306-2320

# Appendix I

# Lactic acid – HPLC Calibration curve

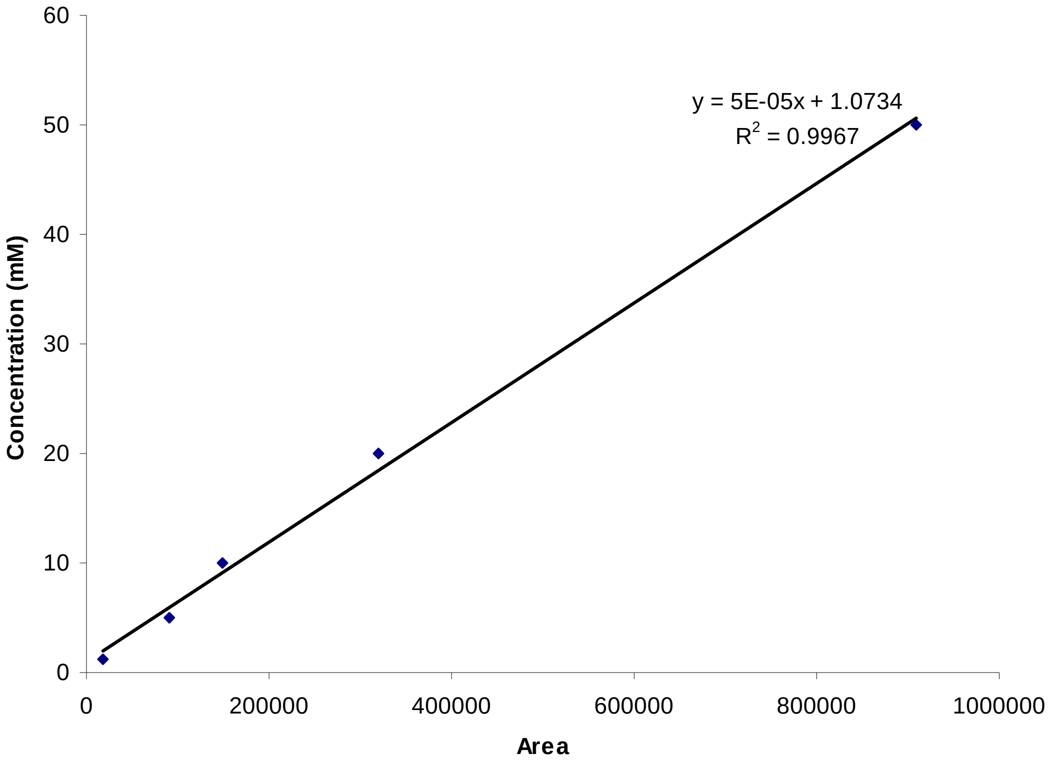

# HPLC baseline curves

## Ringers buffer

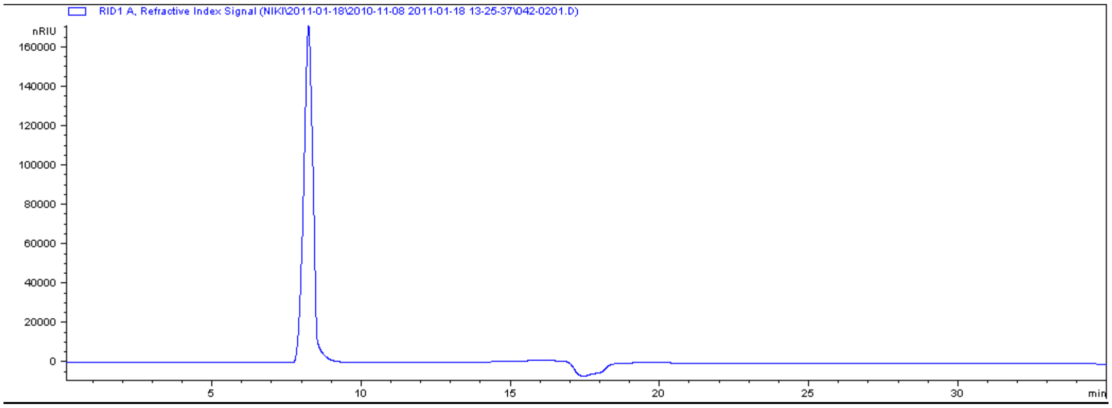

## Isopropanol

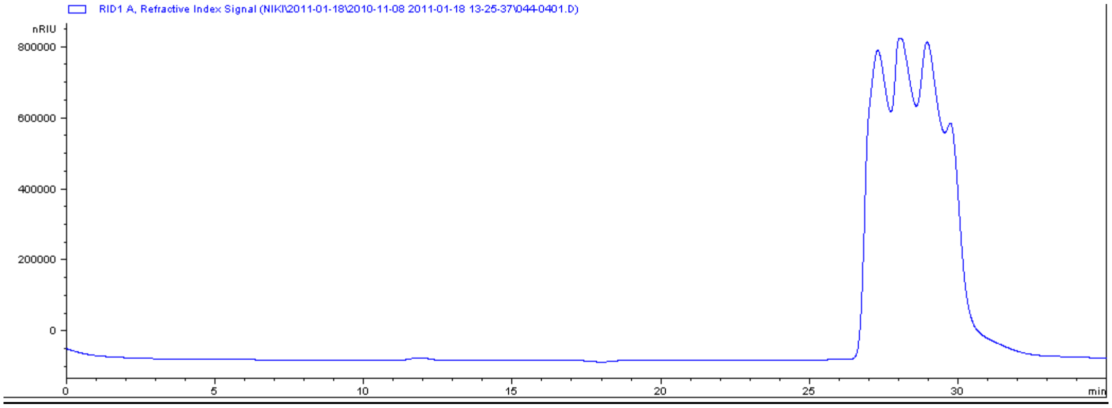

# Appendix II